UNIVERSITY OF ROCHESTER
LABORATORY FOR LASER ENERGETICS

Volume 115
April–June 2008
DOE/NA/28302-846

LLE Review

Quarterly Report

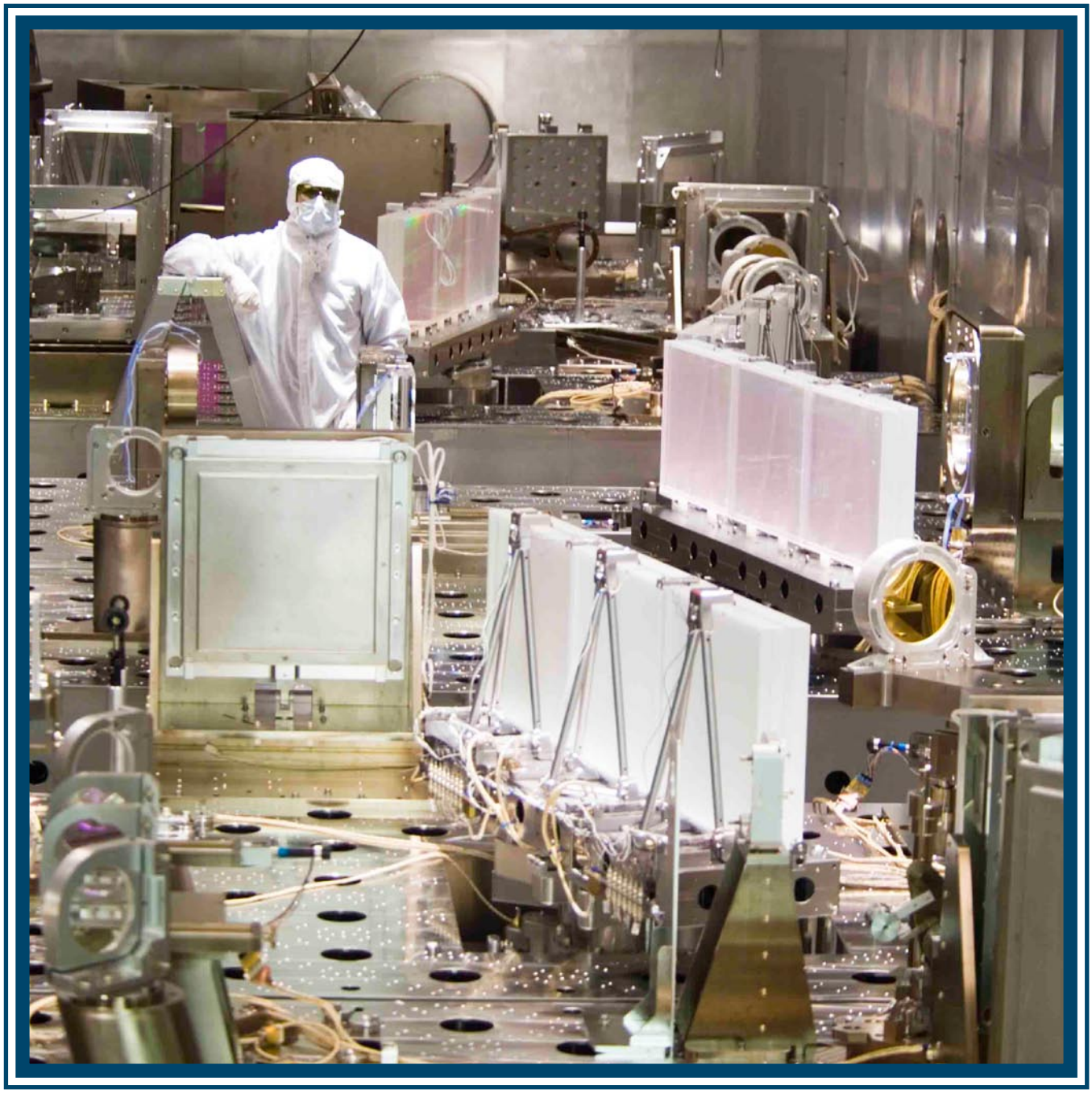

About the Cover:

LLE scientists and engineers have developed an automatic interferometric large-aperture grating tiling technique and realized two tiled-grating compressors for the OMEGA EP High-Energy, Petawatt-Class Laser System. Each compressor consists of four sets of 1.41-m × 0.43-m tiled-grating assemblies (TGA's), each having three 0.47-m × 0.43-m grating tiles. This demonstration has overcome the size limitation of the current state-of-the-art diffraction grating. It opens the path for constructing even larger tiled-grating compressors (multiple meters) for high-energy, high-power optical parametric chirped-pulse–amplification systems. Samuel F. B. Morse, OMEGA Facility Director, is seen standing in the OMEGA EP upper compressor inside the grating compressor chamber (GCC). An embedded Fizeau interferometer was used to tile all four TGA's of each compressor. The results of the tiled-grating compressors are reported (see "Development and Demonstration of Large-Aperture Tiled-Grating Compressors for the OMEGA EP Petawatt-Class Laser System," p. 113).

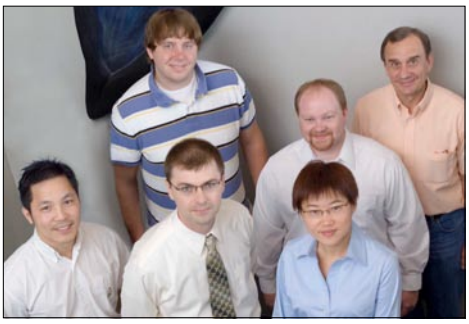

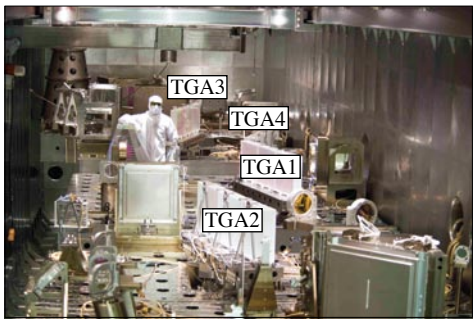

The inside cover photos show members of the Large-Aperture Grating Tiling Development and Realization Team. The four tiled-grating assemblies (TGA's) are illustrated in the photo. Principal Investigator Dr. Jie Qiao, Scientist at LLE (row 1, far right), developed the automatic interferometric tiling and final tiling-optimization techniques for OMEGA EP tiled-grating compressors. She also developed an optical model of the tiled-grating compressor to predict the effects of grating-tile wavefront, tiling error, and compressor input-beam wavefront on focal-spot performance. This model directed the selection and orientation of all 24 grating tiles. Dr. Qiao ultimately led the team to tile all eight TGA's at vacuum inside the GCC. Project Coordinator David Canning (row 1, middle), together with Adam Kalb (row 2, left), Thanh Nguyen (row 1, left), and other LLE engineers, built, qualified, and deployed eight high-precision TGA's. Troy Walker and William Noonan (row 2, from left to right) worked on the control and software for positioning tiling actuators. The team, with the support of other LLE engineers, delivered two fully aligned, tiled-grating compressors. Both compressors (in operation since February 2008) achieved less than 1-ps pulse width.

This report was prepared as an account of work conducted by the Laboratory for Laser Energetics and sponsored by New York State Energy Research and Development Authority, the University of Rochester, the U.S. Department of Energy, and other agencies. Neither the above named sponsors, nor any of their employees, makes any warranty, expressed or implied, or assumes any legal liability or responsibility for the accuracy, completeness, or usefulness of any information, apparatus, product, or process disclosed, or represents that its use would not infringe privately owned rights. Reference herein to any specific commercial product, process, or service by trade name, mark, manufacturer, or otherwise, does not necessarily constitute or imply its endorsement, recommendation, or favoring by the United States Government or any agency thereof or any other sponsor. Results reported in the LLE Review should not be taken as necessarily final results as they represent active research. The views and opinions of authors expressed herein do not necessarily state or reflect those of any of the above sponsoring entities.

The work described in this volume includes current research at the Laboratory for Laser Energetics, which is supported by New York State Energy Research and Development Authority, the University of Rochester, the U.S. Department of Energy Office of Inertial Confinement Fusion under Cooperative Agreement No. DE-FC52-08NA28302, and other agencies.

Printed in the United States of America
Available from
National Technical Information Services
U.S. Department of Commerce
5285 Port Royal Road
Springfield, VA 22161
Price codes: Printed Copy A04
Microfiche A01

For questions or comments, contact John A. Marozas, Editor, Laboratory for Laser Energetics, 250 East River Road, Rochester, NY 14623-1299, (585) 273-5605.

Worldwide-Web Home Page: http://www.lle.rochester.edu/

UNIVERSITY OF ROCHESTER
LABORATORY FOR LASER ENERGETICS

Volume 115
April–June 2008
DOE/NA/28302-846

LLE Review

Quarterly Report

UR LLE

Contents

In Brief

This volume of the LLE Review, covering April–June 2008, features "Development and Demonstration of Large-Aperture, Tiled-Grating Compressors for the OMEGA EP Petawatt-Class Laser System" by J. Qiao, A. Kalb, D. Canning, T. Nguyen, J. Bunkenburg, and J. H. Kelly. In this article (p. 113), the authors report on the OMEGA EP effort regarding the two large-aperture tiled-grating (1.5-m) compressors. Each compressor, consisting of four sets of tiled-grating assemblies, has been built for the OMEGA EP High-Energy, Petawatt-Class Laser System. The techniques used for tiling individual tiled-grating assemblies and for optimizing the overall performance of a tiled-grating compressor are described. Both compressors achieved subpicosecond-pulse duration without tiling-induced temporal degradation. A ray-tracing model predicted that the static wavefront of the grating tiles dominated focal-spot degradations when submicroradian tiling accuracy is achieved. The tiled-grating compressors delivered a tighter focal spot compared to sub-aperture grating compressors with single central tiles.

Additional highlights of recent research presented in this issue include the following:

- C. Stoeckl, K. S. Anderson, T. R. Boehly, J. A. Delettrez, V. N. Goncharov, V. Yu. Glebov, J. H. Kelly, R. L. McCrory, S. F. B. Morse, J. F. Myatt, P. M. Nilson, T. C. Sangster, A. A. Solodov, M. Storm, W. Theobald, B. Yaakobi, L. J. Waxer, and C. D. Zhou (LLE), R. Betti and D. D. Meyerhofer (LLE and the Fusion Science Center for Extreme States of Matter and Fast Ignition Physics), along with J. A. Frenje and R. D. Petrasso (Plasma Science and Fusion Center, MIT), A. J. MacKinnon (LLNL), and P. A. Norreys and R. B. Stephens (RAL) describe a comprehensive scientific program being pursued at LLE to explore the physics of fast ignition (p. 120). The OMEGA EP Laser Facility was completed in April 2008, adjacent to the 60-beam, 30-kJ OMEGA Laser Facility. OMEGA EP consists of four beamlines with a NIF-like architecture. Two of the beamlines can operate as high-energy petawatt (HEPW) lasers, with up to 2.6 kJ each with 10-ps pulse duration. These beams can either be injected into the OMEGA EP target chamber or combined collinearly into the existing OMEGA target chamber for integrated fast-ignitor experiments. Fuel-assembly experiments on OMEGA have achieved high fuel areal densities, and the effects of a cone on the fuel assembly are being studied. Experiments on short-pulse laser systems in collaboration with other institutions are being pursued to investigate the conversion efficiency from laser energy to fast electrons. A coherent transition radiation diagnostic is being developed to study the transport of the electrons in high-density material. Integrated experiments with room-temperature targets on OMEGA will be performed in 2008. Simulations of these integrated experiments show significant heating of up to 1 keV due to the hot electrons from the short-pulse laser.

- J. Bromage, S.-W. Bahk, D. Irwin, J. Kwiatkowski, A. Pruyne, M. Millecchia, M. Moore, and J. D. Zuegel present an on-shot focal-spot diagnostic for characterizing high-energy, petawatt-class laser systems (p. 130). Accurate measurements at full energy are demonstrated using high-resolution wavefront sensing in combination with techniques to calibrate on-shot measurements with low-energy sample beams. Results are shown for full-energy activation shots of the OMEGA EP Laser System.

- S. P. Regan, W. Seka, C. Stoeckl, V. Yu. Glebov, and T. C. Sangster (LLE), D. D. Meyerhofer and R. L. McCrory (LLE and the Departments of Mechanical Engineering and Physics and Astronomy), along with N. B. Meezan, L. J. Suter, D. J. Strozzi, E. A. Williams, O. S. Jones, D. A. Callahan, M. D. Rosen, O. L. Landen, S. H. Glenzer, C. Sorce, and B. J. MacGowan (LLNL), and W. L. Kruer (University of California, Davis) describe how two bursts of suprathermal electrons are observed from gas-filled hohlraums when driven with 13.5 kJ of 351-nm laser light on the OMEGA Laser System (p. 139). The two-plasmon-decay ($2\omega_{pe}$) instability in the exploding laser entrance hole (LEH) window appears to produce up to 20 J of hot electrons with $T_{hot} \sim 75$ keV at very early times and has a very sharp laser-intensity threshold around 0.5×10^{15} W/cm^2. The second pulse produced by stimulated Raman scattering (SRS) during the main laser drive has more energy ($E_{hot} \sim 200$ J), but significantly lower $T_{hot} \sim 20$ keV. While the $2\omega_{pe}$ instability has been observed in direct-drive-implosion targets, this is the first observation of significant effects of the instability in indirect-drive-implosion targets.

- D. H. Edgell, W. Seka, R. E. Bahr, T. R. Boehly, and M. J. Bonino describe the effectiveness of a laser shinethrough barrier for direct illumination of a spherical target in direct-drive inertial confinement fusion experiments (p. 144). In the earliest stages of irradiation, before the plasma forms a critical-density surface, laser light can penetrate into the target. This "shinethrough" light can be sufficiently intense to undergo filamentation and damage the inside of the target, thereby seeding hydrodynamic instabilities. Laser shinethough can be blocked by a thin coating of opaque material such as aluminum (Al). For cryogenic direct-drive targets, the shinethrough barrier material must also be compatible with cryogenic target-fabrication procedures, which rules out Al layers since they would interfere with permeation filling and optical characterization of cryogenic targets. Silicon (Si) has been found to be a promising candidate for a direct-drive cryogenic target shinethrough barrier material. Several cryogenic targets have been coated with Si, successfully permeation filled with either D_2 or DT, and subsequently layered and optically characterized. Various thicknesses of Si coatings have been applied to planar targets and tested under relevant irradiation conditions. Experiments have shown that 200 μm of Si is sufficient to protect targets from laser shinethrough.

- W. Guan and J. R. Marciante describe the suppression and elimination of self-pulsing in a watt-level, dual-clad, ytterbium-doped fiber laser (p. 150). Self-pulsations are caused by the dynamic interaction between the photon population and the population inversion. The addition of a long section of passive fiber in the laser cavity makes the gain recovery faster than the self-pulsation dynamics, allowing only stable continuous-wave lasing. This scheme provides a simple and practical method for eliminating self-pulsations in fiber lasers at all pumping levels.

- J. Kitaygorsky and R. Sobolewski (LLE), along with R. Shouten, S. Dorenbos, E. Reiger, and V. Zwiller (Kavli Institute of Nanoscience, Delft University of Technology, Delft, The Netherlands) present a new readout scheme for NbN superconducting single-photon detectors (SSPD's), using a low-noise cryogenic high-electron mobility transistor and a high-load resistor directly integrated with the detector, to achieve amplitude resolution of dark and photon counts (p. 153). This scheme makes it possible to study the physical origin of dark counts in SSPD's and may enable both photon-number-resolving and energy-resolving capabilities of the standard, meander-type SSPD.

John A. Marozas
Editor

Development and Demonstration of Large-Aperture Tiled-Grating Compressors for the OMEGA EP Petawatt-Class Laser System

Introduction

The OMEGA EP chirped-pulse–amplification system at LLE requires two 1.5-m large-aperture grating compressors to achieve high-energy petawatt capability.[1] The current state-of-the-art multilayer dielectric (MLD) diffraction gratings cannot meet this size requirement.[2] Several institutes have explored the possibility of tiling gratings.[3–6] Kessler and Cotel have demonstrated the coherent addition of small-scale gold gratings in a compressor using a far-field method.[5,6]

Due to the wavefront of large gratings and the general difficulty in achieving diffraction-limited, far-field performance with a 0.5-m-aperture beam, a far-field method alone cannot provide sufficient tiling accuracy for large-scale grating tiling. We have developed and automated an interferometric tiling method and, for the first time, demonstrated a 1.5-m tiled-grating assembly (TGA) composed of three full-size gratings (0.47 m × 0.43 m, 0.5 m in diagonal).[7] In this article, we report the first demonstration of two large-aperture tiled-grating compressors. The architecture and tiling performance of all eight TGA's developed for the two compressors of OMEGA EP are reported. The tiling technique and the method used for constructing a tiled-grating compressor are described. The full spatial and temporal performance of the tiled-grating compressors is reported.

The following sections (1) describe the pulse compression architecture of OMEGA EP and the development of the tiled-grating assemblies; (2) analyze tiling effect on focal-spot performance and the method for constructing a tiled-grating compressor; (3) present the near-field tiling technique in vacuum and the performance of each tiled TGA; and (4) report on tiling optimization and the characterization of the spatial and temporal performances.

OMEGA EP Pulse-Compression Architecture and Tiled-Grating-Assembly Development

OMEGA EP has two separate grating compressors that produce two short-pulse beams (1 ~ 100 ps). Figure 115.1(a) shows the pulse-compression scheme for OMEGA EP. Each compressor consists of four sets of TGA's, each having three 0.47-m × 0.43-m gratings. In total, eight TGA's and 24 grating tiles are required to construct the two compressors. The beam size of the OMEGA EP laser is 0.37 m × 0.37 m. The incident angle on TGA1 is 72.5°, which offers a large pulse-compression ratio and relaxes the damage-threshold requirements for the gratings. Figure 115.1(b) shows the rear view of one TGA, which holds three full-size OMEGA EP grating tiles. Each tile is mounted on a triangular support frame. All three tile support frames are mounted on a mechanical platform, with the center support frame fixed to the mechanical platform to provide structural stability. The mechanical platform is positioned on a rotary stage, which allows the entire TGA to rotate between

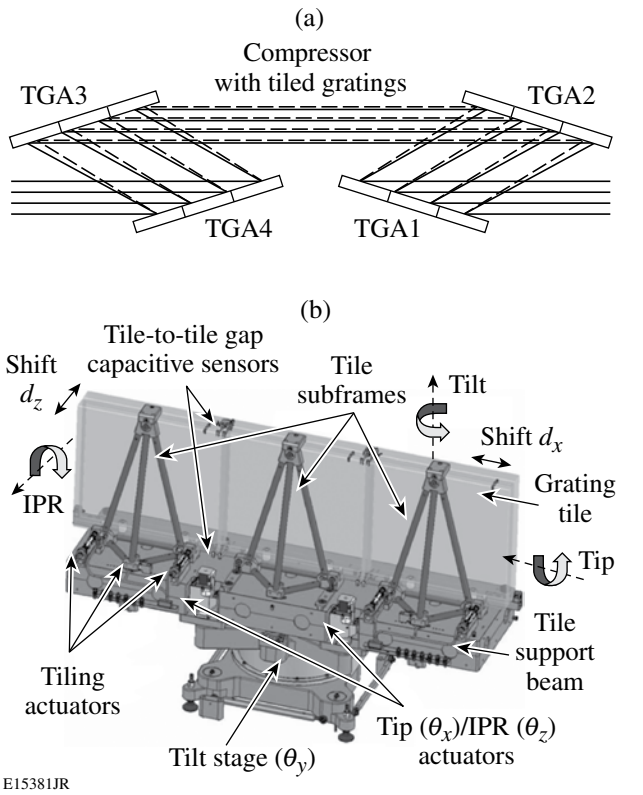

Figure 115.1
(a) OMEGA EP compressor consists of four tiled-grating assemblies (TGA's). The size of each TGA is 1.41 m × 0.43 m. (b) TGA assembly and tiling parameters.

–175° to +175° (θ_y rotation). Tip (θ_x) and in-plane rotation (IPR/θ_z) movements are provided by two motorized linear actuators mounted on the back of the mechanical platform.

Tile-to-tile alignment is realized by maintaining the central tile static and by moving the two outboard tiles relative to the central tile. For each outboard tile, there are six degrees of freedom relative to the central tile: tilt θ_y, tip θ_x, IPR θ_z, lateral shift d_x, longitudinal shift (also referred to as piston d_z), and relative groove-spacing change Δ_d. The six parameters form three independent pairs: piston and lateral shift, tip and IPR, and tilt and groove spacing change. The two parameters within each pair compensate each other;[8] therefore, each of the outboard tile support frames incorporates only three electrostrictive actuators to provide tile-to-tile alignment by modifying tip, tilt, and piston. Each actuator is paired with a capacitive sensor to form a closed control loop to hold its position. The resolution for holding the position of an actuator is ±4 nm. For coarse alignment, the TGA is positioned at normal and Littrow angles iteratively to remove the tip and IPR of the central tile by adjusting the two linear actuators. The grating grooves of outboard tiles can be aligned to that of the central tile by manually adjusting the tip and IPR through three screws underneath the tile support beam. The initial aligned position is determined by interferometric analysis. The changes from the aligned positions in terms of piston and lateral shift, tip, and IPR are monitored by two pairs of capacitive sensors across the tile gap mounted on the top and bottom surfaces of the tile substrates. The aligned position is then maintained in real time by compensating the temporal drift of the lateral shift and the in-plane rotation with the piston and tip, respectively. Eight sets of TGA's have been built for the two compressors of OMEGA EP.

Modeling for Focal-Spot Analysis and Tiled-Compressor Construction

A ray-tracing model has been developed to perform tiling tolerance analysis for the full tiled-grating compressor system followed by an *f*/2 parabola for focusing (i.e., 12 gratings grouped in four TGA's). This model simulates the influence of misalignment on all four TGA's of a compressor taking into account the measured wavefronts of the grating tiles. The performance of a tiled-grating compressor is fundamentally determined by the initial tiling performance and the long-term stability of a TGA. The initial tiling is constrained by the interferometric measurement, which is subject to disturbance caused by turbulence and vibration; the long-term stability of a TGA is determined by environmental stability, such as temperature and vibration. Taking into account the sensitivity of the tiling interferometer and the mechanical and environmental stability of a TGA, the best-achievable tiling accuracy for each tile of each TGA was determined to be approximately ±0.2 μrad, ±0.2 μrad, and ±0.13 μm for tilt plus groove spacing change, tip plus IPR, and piston plus lateral shift, respectively. For each OMEGA EP compressor, there are eight outboard tiles to be aligned to their corresponding central tiles. Since there are three independent tiling parameters for each tile, the total number of independent tiling parameters is 24. It is necessary to understand and predict the combined effect of the tiling errors described above on the focal spot of the tiled-grating compressor. For each outboard tile of a TGA of the compressor, the tilt, tip, and piston were chosen as the independent tiling parameters to perform a Monte Carlo tolerance analysis, i.e., each outboard tile's position in terms of tilt, tip, and piston was randomly perturbed within the tiling accuracy. This simulation was done in the case of a flat grating-tile wavefront and a measured non-flat grating-tile wavefront. For both cases, the input beam of the compressor was flat. The mean and standard deviation values of the radius of 80% encircled energy, R_{80}, and Strehl ratio were calculated for 500 runs. Figure 115.2 shows the histograms of the far-field performance of 500 randomly realized tiled-grating compressors with a tiling accuracy tilt/tip = ±0.2 μrad and piston = 0.13 μm for the grating tiles with a flat wavefront. The mean and standard deviation of R_{80} are 4.2 μm and 0.66 μm, respectively.

The size of each of the 12 holographically recorded MLD diffraction-grating tiles is 0.47 m × 0.43 m. The state-of-the-art wavefront quality for this size of grating tile is approximately 0.25 λ (peak-to-valley), λ (wavelength) = 1053 nm. Grating wavefront error consists of a substrate mirror term due to coat-

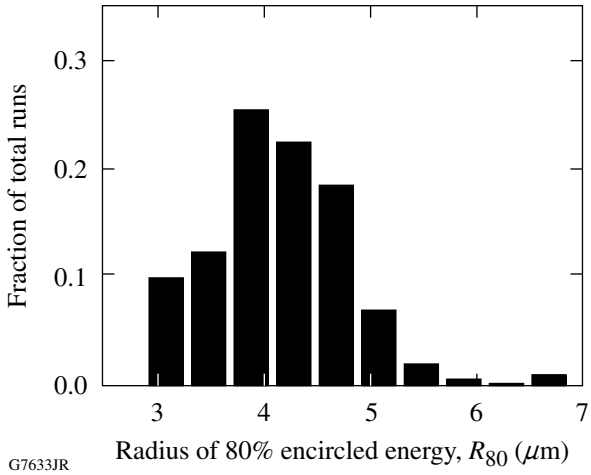

Figure 115.2
The histograms of R_{80} for 500 simulations considering the experimental tiling error and flat grating-tile wavefront.

ing and a holographic term, which could add or cancel each other, depending on the orientation of the grating relative to the beam. The final wavefront of the compressor varies with the choice, order, and orientation of each of its 12 gratings. These properties were optimized to minimize the overall wavefront of the compressor using a matrix-based procedure that considers the measured wavefront of each individual grating tile at both orientations. We have modeled the focal-spot degradation caused by the static wavefront of all grating tiles for various compressor configurations. In these simulations, the three glass substrates of each TGA are perfectly aligned, i.e., there is no tiling error. The compressor configurations producing the minimum total wavefront error were selected for actual construction. Figure 115.3(a) shows the minimized wavefront map of one realization. The peak-to-valley and rms wavefront are 0.73 λ and 0.07 λ, respectively. The corresponding R_{80} is 7.3 μm. The design baseline corresponding to a flat wavefront is 2.6 μm. A Monte Carlo tiling-tolerance analysis predicted the focal-spot degradation under imperfect tiling conditions by using the measured wavefront of the tiles and the experimental tiling accuracy of tilt/tip ±0.2 μrad and piston ±0.13 μm. Figure 115.3(b) shows the histogram of R_{80} for 500 simulations. The mean and standard deviation of R_{80} are 7.7 μm and 0.8 μm, respectively. Considering the focal-spot size without tiling error (R_{80} = 7.3 μm) and the design baseline (R_{80} = 2.6 μm), we conclude that the focal-spot degradation is dominated by the static grating wavefront when submicroradian tiling accuracy can be achieved. We can also conclude that, given the same tiling accuracy, the focal-spot degradation caused by tiling error is greater for a compressor consisting of grating tiles with flat wavefront (R_{80} changes from 2.6 μm to 4.2 μm) than for that consisting of grating tiles with non-flat wavefront (R_{80} changes from 7.3 μm to 7.7 μm).

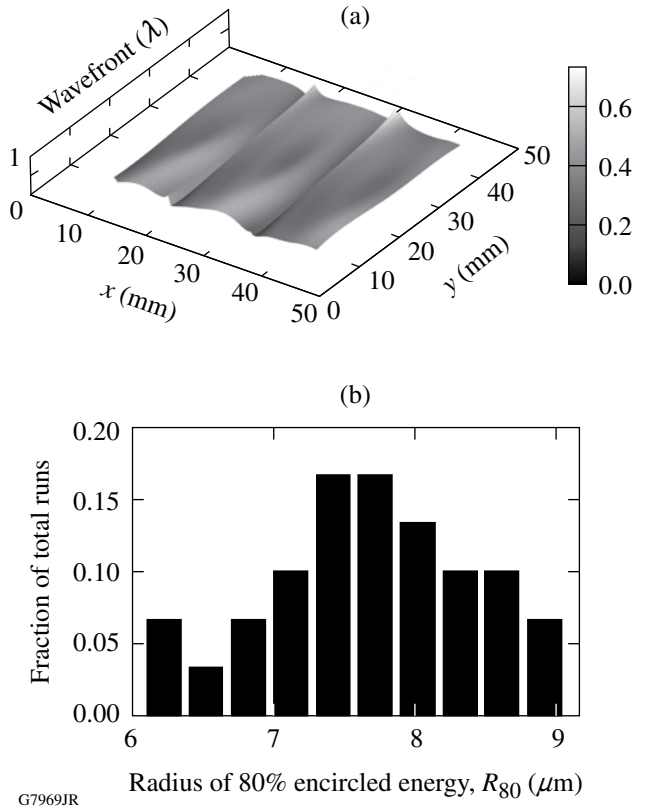

Figure 115.3
(a) The wavefront map of one compressor realization when there is no tiling error. (b) The histogram of R_{80} for 500 simulations when tiling error and grating-tile wavefront are taken into account.

Interferometric Tiling Technique in a Grating Compressor Chamber at Vacuum and the Performance of the Tiled TGA's

A 12-in.-aperture Fizeau interferometer was built for each compressor inside the grating compressor chamber (GCC) to tile individual TGA's at vacuum. The laser wavelength of the interferometer is 1053 nm. As shown in Fig. 115.4, the col-

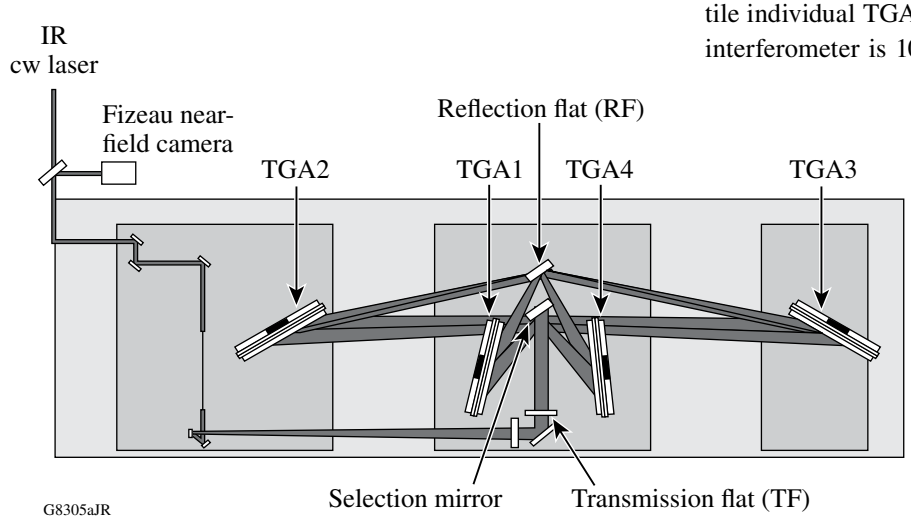

Figure 115.4
Optical layout for tiling each individual TGA with a Fizeau interferometer inside the GCC. The combined movement of the TGA selection mirror and RF makes it possible for the interferometer to see all of the gaps of the four TGA's, sequentially.

limated Fizeau beam is transmitted through the transmission flat and directed to two adjacent tiles of each one of the four TGA's by the selection mirror. The reflection flat (RF) is oriented to retroreflect the diffracted beam from each TGA at its working angle. Unique orientations of the TGA's, the selection mirror, and the RF were required to sequentially tile each of the eight gaps of four TGA's. The Fourier analysis of the resulting interferogram[9] was used to retrieve the phase of each tile and to calculate the differential tilt, tip, and piston between the central tile and an outboard tile. The differential values were used as feedback to control the tiling actuators to minimize the overall wavefront of the full TGA. This near-field tiling process has been automated.

To predict the focal-spot performance of a tiled-grating compressor, it is essential to obtain the overall wavefront and stability of a tiled TGA having three tiles. Before the TGA's were installed inside the GCC, a 24-in.-aperture Fizeau interferometer was used to tile each TGA and obtain the overall wavefront using an automated near-field method in a large-optics test facility.

Figures 115.5(a)–115.5(c) illustrate the automatic tiling process and show the phase map of the two tiles under alignment before, during, and at the end of the automatic tiling process, respectively. Minimized wavefront (rms wavefront = 0.0562 λ) of the two tiles was achieved after removing the angular and piston misalignment between the two tiles.

Figure 115.6(a) shows the overall rms wavefront of all tiled TGA's, which is under 0.08 λ. Figure 115.6(b) illustrates the typical tiling stability. The tiled wavefront of one of the eight TGA's was maintained below 0.09 λ for at least 12 h by tiling actuators in a closed control loop. The stability test was done during the night since there were many other integration activities around the interferometer area during the day. Please note: the grating compressor vacuum chamber provides a much more controlled environment.

After all of the eight TGA's were installed inside the GCC, they were retiled using the GCC interferometers. The differential angle between two adjacent tiles was measured for 12 h by the Fizeau interferometer. Figure 115.7 shows the typical

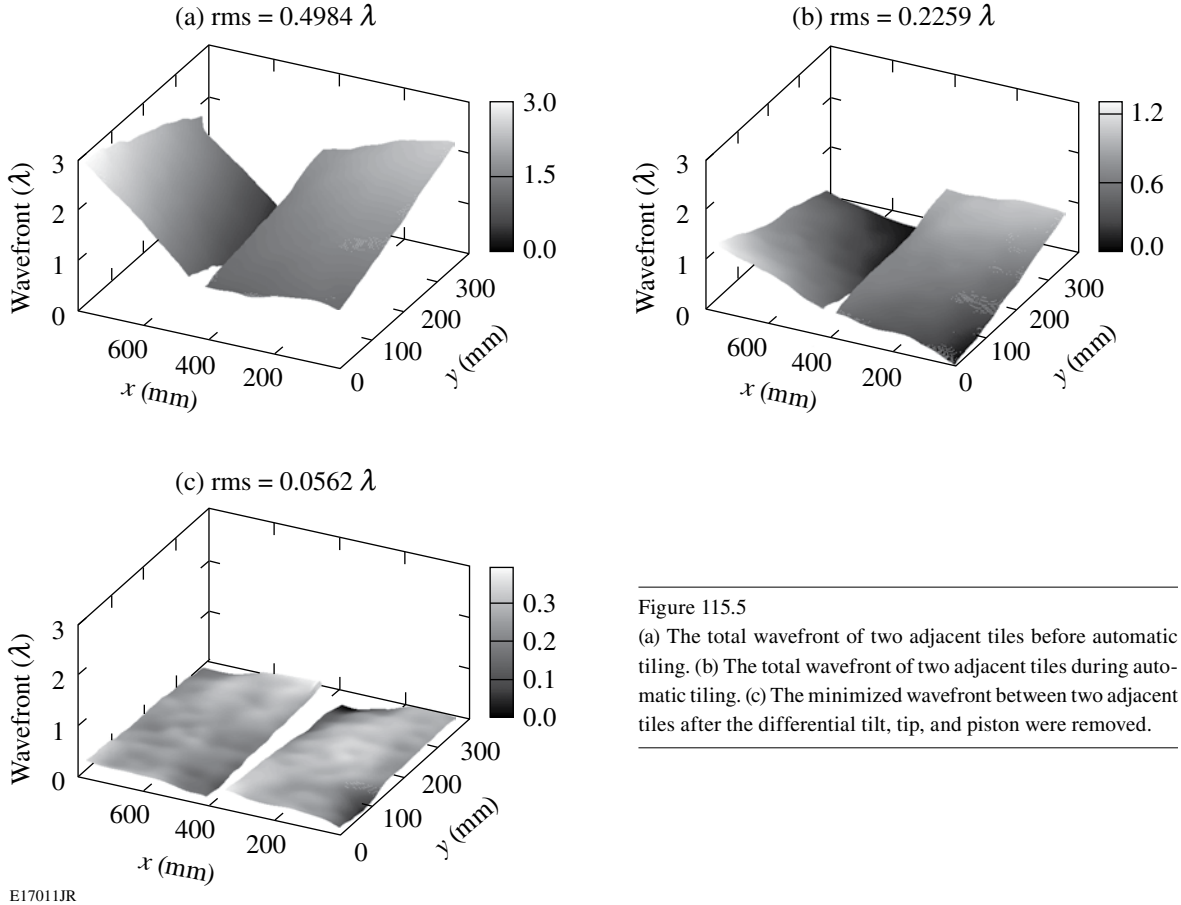

Figure 115.5
(a) The total wavefront of two adjacent tiles before automatic tiling. (b) The total wavefront of two adjacent tiles during automatic tiling. (c) The minimized wavefront between two adjacent tiles after the differential tilt, tip, and piston were removed.

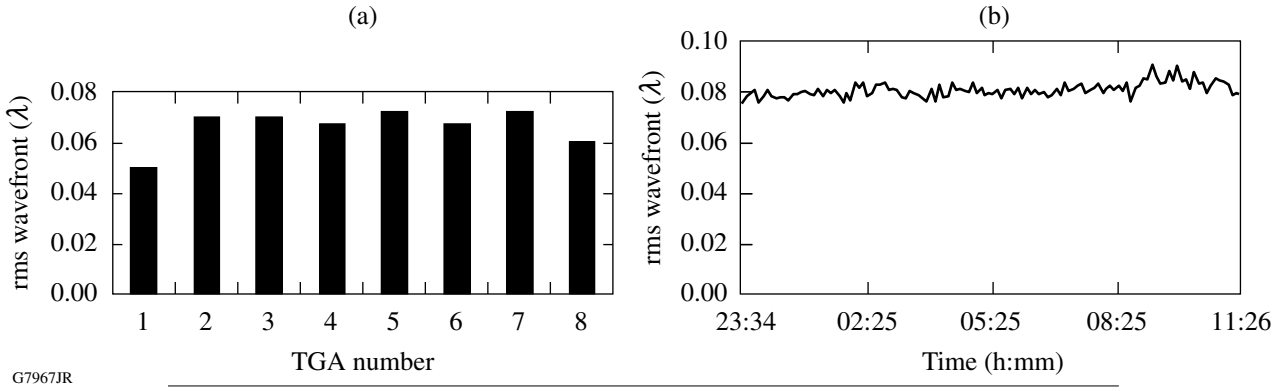

Figure 115.6
(a) Root-mean-square (rms) tiled wavefronts of all eight TGA's; (b) typical wavefront stability of a tiled TGA.

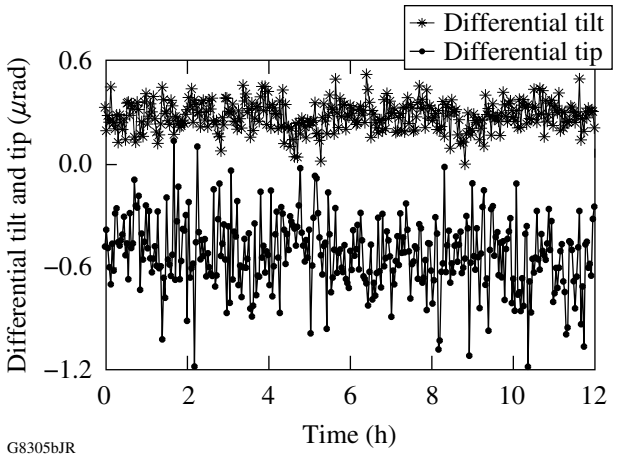

Figure 115.7
Angular tiling stability in the GCC at vacuum.

angular tiling stability in the GCC at vacuum. The standard deviation of the differential tilt (horizontal) and differential tip (vertical) is 0.1 μrad and 0.2 μrad, respectively.

Performance Characterization and Optimization of Tiled-Grating Compressors

After individual TGA tiling, the four TGA's were rotated to their previously aligned compressor position. Any residual tiling misalignment among the four outboard tiles (i.e., one tile per TGA) on the same side of the beam can be canceled using one of the tiles (see the highlighted tiles in Fig. 115.8). We chose to use the outboard tiles of TGA4 to compensate the cumulative tiling error. This was done by a far-field analysis. A tiling apodizer array with three different apertures was placed in the collimated tiling-beam space. The translation of the tiling-apodizer array limited the illumination of the compressor to one single tile, two adjacent tiles, or all three tiles at a time. The far-field pattern of two adjacent tiles is compared to that of the central tiles in order to obtain angular misalignment and differential phase information, therefore providing feedback to drive the corresponding tiling actuators of TGA4 to remove the residual tiling error. After this tiling optimization, the three-tile apodizer is translated into the beam to evaluate the final tiling performance.

It is not possible to directly compare the focal-spot performance of the tiled-grating compressor having four sets of TGA's (a total of 12 tiles) to that of a compressor consisting of four monolithic gratings with the same aperture size due to the unavailability of the latter. To evaluate the effect of tiling on focal-spot degradation, we apodized the beam size along the tiling (horizontal) direction to construct a sub-aperture compressor consisting of only the four central tiles. The aperture-size ratio between the single-central-tile compressor and the triple-tile compressor is 1:2.95 and 1:1 along the horizontal and vertical directions, respectively. Since the two compressors have the same beam size along the vertical direction, the two vertical lineouts were compared to evaluate focal-spot degradation due to tiling. The two horizontal lineouts were compared to show the aperture ratio between the two configurations. Figures 115.9(a) and 115.9(b) show the focal spots of the single-central-tile compressor and the triple-tile compressor, respectively. Figure 115.9(c) shows a comparison between two horizontal and vertical lineouts. In these plots, f_x and f_y are the dimensions, in microradians, of the focal spot along the horizontal and vertical directions.

The full width at half maximum (FWHM) of the focal-spot lineout ratio between the single-central-tile sub-aperture compressor and the triple-tile full-aperture compressor is 3:1 and 1:1 for the horizontal and vertical directions, respectively. This is expected when comparing a sub-aperture compressor to a properly aligned full-aperture grating compressor with four monolithic gratings. The profiles of two vertical lineouts are comparable. We can conclude that tiling does not degrade the

spatial performance of the tiled-grating compressor. A triple-tile compressor delivers a tighter focal spot and three times the energy of a single-central-tile-only compressor.

After compressor alignment and grating tiling, temporal compression was optimized by changing the dispersion of the stretcher. The optical parametric chirped-pulse–amplification

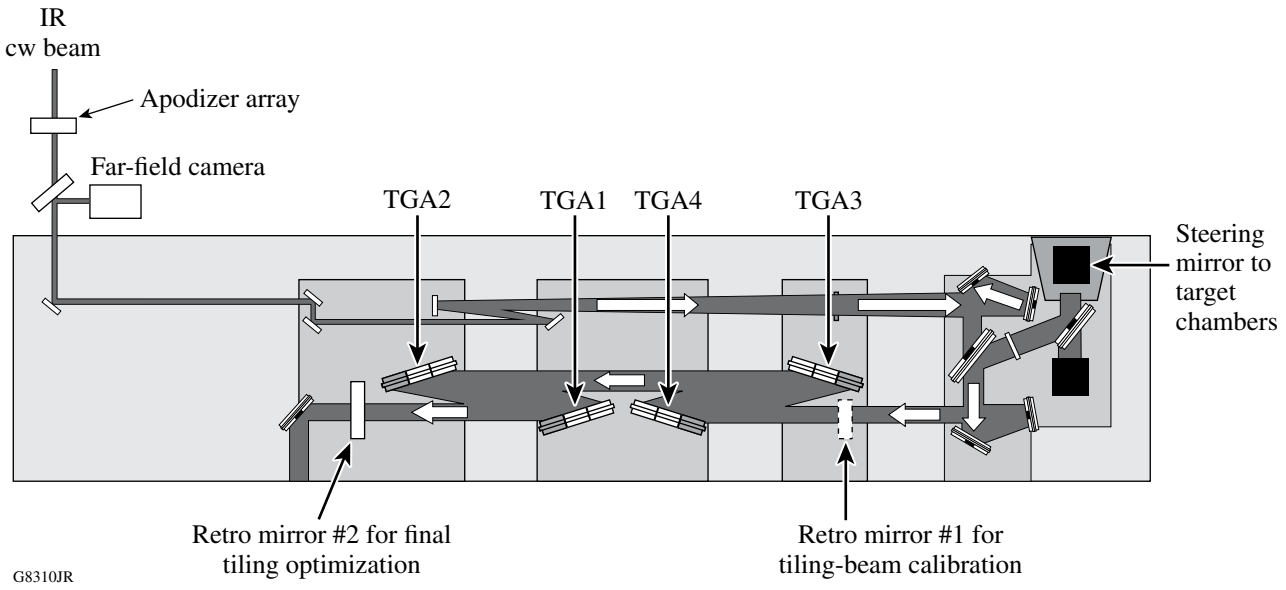

Figure 115.8
Optical layout for evaluating and optimizing overall tiling performance of the whole compressor. Before tiling optimization, retro mirror #1 was used to calibrate the far field of the tiling beam. During tiling optimization, this mirror was removed from the beam. The tiling beam went through the compressor and was reflected back by retro mirror #2. One of the four highlighted tiles was chosen to optimize the overall tiling performance.

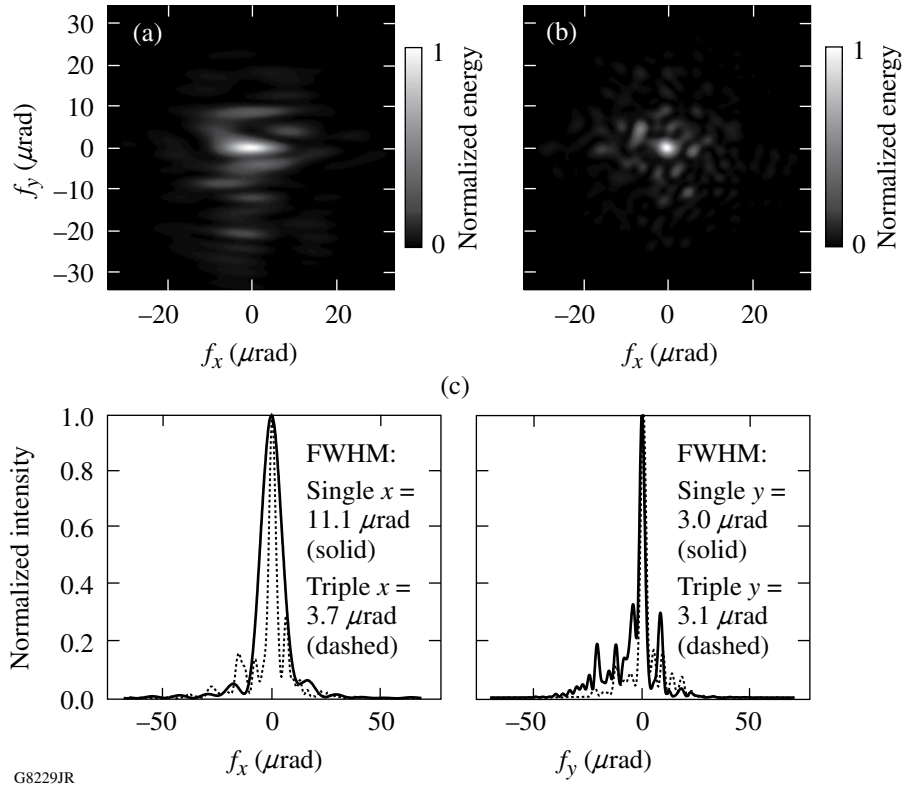

Figure 115.9
(a) Focal spot of the single-central-tile compressor; (b) focal spot of the triple-tile compressor; (c) comparison between the horizontal lineouts and vertical lineouts of the two focal spots.

(OPCPA) front end is operated at 5 Hz (Ref. 10). The autocorrelation of the output pulses was measured for both single-central-tile and triple-tile configurations for both OMEGA EP compressors. Figures 115.10(a) and 115.10(b) show the measured autocorrelations with a decorrelation factor of 1.34 (calculated from the measured spectrums). The pulse width is 630 fs for both the single-central-tile and triple-tile configurations of compressor 1. Similarly, we obtained a 600-fs pulse width for the single-central-tile and triple-tile configurations of compressor 2. The transform-limited pulse width is 400 fs and 410 fs for compressors 1 and 2, respectively. Single- and triple-tile configurations delivered the same pulse width. Therefore, there is no change in pulse duration due to tiling.

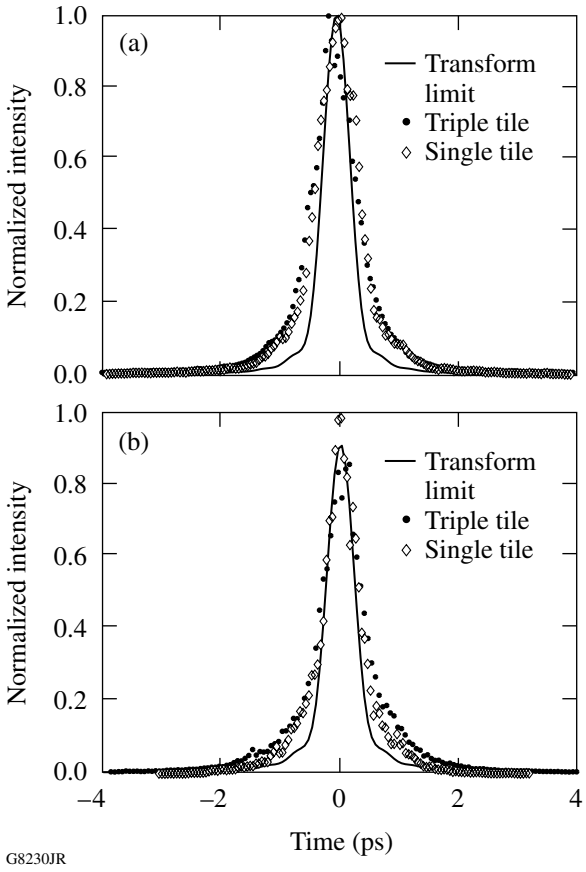

Figure 115.10
(a), (b) Autocorrelation scanning results for single-tile and triple-tile configurations for (a) compressor 1 and (b) compressor 2.

Conclusions

In conclusion, we have developed and built eight precision tiled-grating assemblies. Submicroradian tiling accuracy and stability have been achieved for all eight TGA's. A ray-tracing model predicts that the static wavefront of the grating tiles dominates focal-spot degradations when submicroradian tiling accuracy is achieved. For the first time, we demonstrated pulse compression in two 1.5-m, large-aperture tiled-grating compressors for the OMEGA EP high-energy, petawatt-class laser system. Measurement of the tiled-grating compressors verified the model prediction and confirmed that the focal-spot degradation caused by tiling is minimal. Output-pulse autocorrelation measurements verified that both compressors achieved subpicosecond pulse widths and there is no pulse duration change due to tiling. This demonstration opens the path for constructing even larger tiled-grating compressors (multiple meters) for high-energy, high-power OPCPA systems.

ACKNOWLEDGMENT

This work was supported by the U.S. Department of Energy Office of Inertial Confinement Fusion under Cooperative Agreement No. DE-FC52-08NA28302, the University of Rochester, and the New York State Energy Research and Development Authority. The support of DOE does not constitute an endorsement by DOE of the views expressed in this article. The authors are grateful for valuable support from W. Noonan, T. Walker, R. Kidder, C. Kingsley, G. King, and D. Irwin of LLE.

REFERENCES

1. J. H. Kelly, L. J. Waxer, V. Bagnoud, I. A. Begishev, J. Bromage, B. E. Kruschwitz, T. J. Kessler, S. J. Loucks, D. N. Maywar, R. L. McCrory, D. D. Meyerhofer, S. F. B. Morse, J. B. Oliver, A. L. Rigatti, A. W. Schmid, C. Stoeckl, S. Dalton, L. Folnsbee, M. J. Guardalben, R. Jungquist, J. Puth, M. J. Shoup III, D. Weiner, and J. D. Zuegel, J. Phys. IV France **133**, 75 (2006).

2. J. A. Britten *et al*., in *Laser-Induced Damage in Optical Materials: 2003*, edited by G. J. Exarhos *et al*. (SPIE, Bellingham, WA, 2004), Vol. 5273, pp. 1–7.

3. T. Zhang, M. Yonemura, and Y. Kato, Opt. Commun. **145**, 367 (1998).

4. Y. Zuo *et al*., Opt. Lett. **32**, 280 (2007).

5. T. J. Kessler, J. Bunkenburg, H. Huang, A. Kozlov, and D. D. Meyerhofer, Opt. Lett. **29**, 635 (2004).

6. A. Cotel *et al*., Opt. Express **15**, 2742 (2007).

7. J. Qiao, A. Kalb, M. J. Guardalben, G. King, D. Canning, and J. H. Kelly, Opt. Express **15**, 9562 (2007).

8. *LLE Review Quarterly Report* **100**, 242, Laboratory for Laser Energetics, University of Rochester, Rochester, NY, LLE Document No. DOE/SF/19460-578, NTIS Order No. PB2006-106672 (2004). (Copies may be obtained from the National Technical Information Service, Springfield, VA 22161.)

9. M. Takeda, H. Ina, and S. Kobayashi, J. Opt. Soc. Am. **72**, 156 (1982).

10. V. Bagnoud, I. A. Begishev, M. J. Guardalben, J. Puth, and J. D. Zuegel, Opt. Lett. **30**, 1843 (2005).

Fast-Ignition Target Design and Experimental-Concept Validation on OMEGA

Introduction

The fast-ignitor concept for inertial confinement fusion[1,2] has shown significant promise due to successful small-scale integrated experiments.[3,4] It makes it possible to use lower driver energies than conventional hot-spot ignition[5] and has the potential for higher gains. The fast-ignitor concept separates the fuel assembly and fuel heating by using an ultrafast laser in addition to a driver that compresses the fuel to high density. The ultrafast laser produces relativistic electrons with high efficiency (up to 50% has been reported[6]) that heat the fuel. Options for the compression driver are laser or heavy-ion-beam–heated hohlraums or laser direct drive.[7]

Many challenges remain for the fast-ignitor concept. The first is to demonstrate the required compression of the fuel to areal densities required for ignition. The conversion efficiency from ultrafast laser to energetic electrons must be high at ignition-relevant intensities, energies, and pulse lengths. The energy distribution of the hot electrons must be compatible with the areal density of the compressed core to ensure that the electrons deposit most of their energy into a hot spot of at least 0.3 g/cc cm (Ref. 8). Another challenge is the transport of relativistic electrons from the critical-density region ($n_e \sim 10^{21}$ cm^{-3} for a typical 1-μm laser), where the ultrafast laser is absorbed and converted into electrons, to the compressed fuel—a distance that can be hundreds of microns in an ignition-scale target. For an electron-beam divergence of ~20°, the overlap between the electron beam originating from a small focal spot (~10-μm radius) and the dense core with a diameter of <50 μm would be very small.[9,10] Two solutions have been proposed to minimize this standoff distance: a channeling beam to bore a hole in the plasma atmosphere around the core,[2,11] which would allow the ultrafast laser to be absorbed closer to the core, and a re-entrant cone to keep the path of the ultrafast laser free of plasma and bring it as close as possible to the dense core.[3,12] The cone-in-shell concept, while advantageous with respect to the electron transport, breaks the symmetry of the spherical fuel assembly, which could limit the fuel areal density that can be achieved with a given driver energy. Another issue for cone-in-shell targets is plasma filling the inside of the cone from the shock wave that the high-pressure core plasma sends through the gold cone. Self-generated electromagnetic fields from the propagation of the electron beam in plasma will modify both the transport and the energy-deposition characteristics. The transport and energy deposition of the fusion alpha particles in near-ignition plasma conditions could significantly change the plasma conditions in the assembled fuel.

All of these physics areas will be experimentally accessible with the combined OMEGA/OMEGA EP Facility at LLE. OMEGA EP[13] provides two short-pulse (~1 ps to 100 ps), high-energy laser beams with an energy of up to 2.6 kJ per beam at 1.053 μm, integrated into the existing OMEGA[14] Laser Facility (60 beam, 30 kJ at 0.35 μm). The OMEGA EP beams can be combined collinearly and coaxially and routed to either the existing OMEGA target chamber or the new OMEGA EP target chamber. The combined beams allow the channeling approach to fast ignition (FI) to be studied under realistic conditions for the first time, whereas only one beam is required for cone-in-shell experiments. The OMEGA/OMEGA EP Facility will be best suited to perform integrated fast-ignition experiments because of OMEGA's unique ability to compress cryogenic D_2 and DT targets.[15,16] To study alpha transport under realistic conditions, the areal density of the compressed core must be of the order of the hot-spot areal density of an ignition target, ~0.3 g/cm^2 (Ref. 8), which could be achieved in high-performance cryogenic-DT implosions on OMEGA.[17]

This article describes several important components of LLE's comprehensive scientific program to investigate the physics of the fast-ignitor concept. The following sections (1) introduce the OMEGA/OMEGA EP integrated laser facility; (2) describe hydrodynamic experiments on high-areal-density implosion and fuel assembly with cone-in-shell targets; (3) discuss experiments that measure the conversion efficiency from laser light into energetic electrons and the development of a coherent transition radiation diagnostic to investigate the hot-electron transport; (4) summarize simulations of integrated fast-ignitor physics experiments on OMEGA EP and full-scale, high-gain, fast-ignition experiments; and (5) provide a short summary of the information presented.

Laser System

The OMEGA EP Laser Facility is housed in a structure on the south side of the existing OMEGA laser building (see Fig. 115.11). The OMEGA EP target chamber is due east of the existing OMEGA target chamber. The OMEGA Laser System delivers up to 30 kJ of UV light in 60 beams arrayed in a "soccer ball" symmetry for uniform illumination of spherical implosion targets.[14] OMEGA has an elaborate pulse-shaping system, which can provide up to ~4-ns-long, highly shaped pulses with a contrast of up to 100. The individual OMEGA beams are smoothed by distributed phase plates (DPP's),[18] two-dimensional smoothing by spectral dispersion[19] with 1-THz bandwidth in the UV, and polarization smoothing.[20]

The four new OMEGA EP beamlines are located to the south of the compression chamber and the new target chamber. The beamlines use a folded beam path similar to the architecture[21] of the National Ignition Facility (NIF)—an upper level that includes a 7-disk booster amplifier and a transport spatial filter, and a lower level that includes an 11-disk main amplifier, a cavity spatial filter, a plasma-electrode Pockels cell (PEPC),[22] and a deformable mirror. A second polarizer is inserted between the PEPC and the cavity spatial filter to protect the laser system against IR light reflected from the target when the beamline is operated in short-pulse mode. Two of the beams can be compressed using four 141-cm × 41-cm diffraction-grating units, with each unit consisting of three multilayer-dielectric–grating tiles.[23,24] A deformable mirror placed after the last grating unit provides further wavefront correction in each beamline. The beams are either combined before leaving the compression chamber and propagate coaxially through evacuated tubes to the OMEGA or OMEGA EP target chamber, or they can be directed into the OMEGA EP chamber on separate paths in an orthogonal configuration. An *f*/2 off-axis parabola focuses the short-pulse beam to provide a small focal spot even with the expected phase-front distortions in such a large-scale, high-energy laser system. The beams are synchronized to each other and to the OMEGA laser pulse to better than 10-ps rms. A comprehensive set of laser diagnostics measures the laser energy, pulse duration, and, for the first time on a high-energy petawatt system, the focal-spot intensity distribution at full energy. All four beams can be used as long-pulse beams and converted into the third harmonic at 351 nm (<10 ns, up to 6.5 kJ). These beams propagate only to the OMEGA EP target chamber. The long-pulse beams are focused with *f*/6.5 lenses onto the target and are arrayed in a square with a 23° angle to their common centerline. DPP's for beam shaping will be available in 2009.

Fuel-Assembly Experiments

High fuel compression and high areal densities have been achieved on OMEGA, both with cryogenic targets[25] and room-temperature targets,[26] using highly shaped pulses that put the target on a low adiabat (ratio of the shell pressure to the Fermi-degenerate pressure). It has been shown that the areal density ρR depends primarily on the adiabat α of the target and the laser energy E:[27]

$$(\rho R)_{\max} = 2.6 \Big/ \alpha^{0.54} E_{\mathrm{MJ}}^{0.33}. \tag{1}$$

The cryogenic targets are 10-μm-thick, ~430-μm-outer-radius CD shells, filled with D_2 to form a 95-μm-thick layer at the inside of the CD shell at cryogenic temperatures.

The pulse shape for the cryogenic target (Fig. 115.12) uses a decaying-shock-adiabat shaping picket[28] and a slowly rising

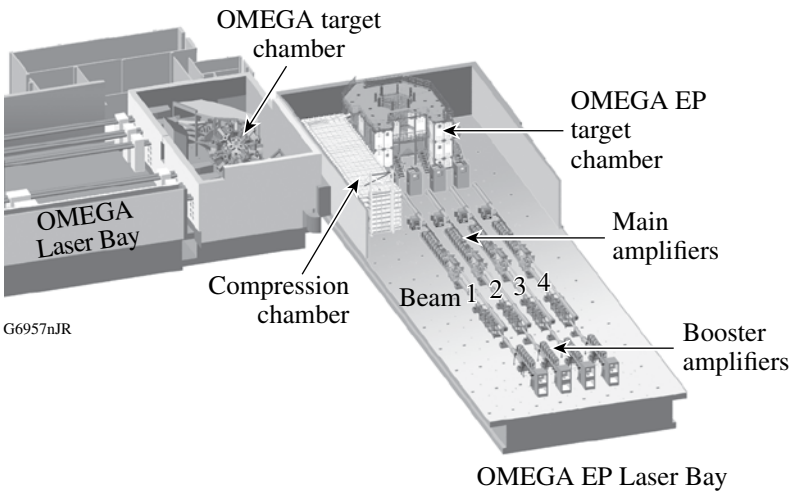

Figure 115.11
Schematic of the expanded OMEGA Laser Facility. The new OMEGA EP laser adjacent to the existing 60-beam OMEGA facility includes four NIF-like beamlines, a compression chamber, and a new target chamber. Two of the four beams can be run in short-pulse mode and can be directed into either target chamber. All four beams can be converted into UV and used in the OMEGA EP target chamber.

main pulse to put the cryogenic D_2 fuel on an adiabat of $\alpha \sim 2$. The areal density of the imploded targets is inferred from the energy downshift in the secondary proton spectrum.[29] These protons are created by D^3He fusion reactions, which are secondary reactions in D_2 fuel. Figure 115.13 shows a measured secondary proton spectrum from the cryogenic target compared to 1-D *LILAC*[30] simulations.[25] An areal density of ~200 mg/cm^2 can be inferred from the spectrum, which is more than 80% of the clean 1-D predictions. The density of the compressed D_2 approaches ~100 g/cm^3—a 500-fold compression of the original D_2-ice density. In the room-temperature experiments, 40-μm-thick, 430-μm-outer-radius plastic shells coated outside with a 0.1-μm layer of aluminum and filled with D_2 gas with pressure ranging from 8 to 25 atm were imploded using relaxation adiabat-shaping, ~16- to 20-kJ UV laser pulses.[26,31,32] A typical experimental pulse shape that puts the room-temperature plastic targets on an adiabat of $\alpha \sim 1.5$ is shown in Fig. 115.12. A picket at the beginning of the pulse and a spike at the end of the pulse were used to optimize the implosion for high yield and high areal density. The room-temperature targets also showed areal densities of up to ~200 mg/cm^2 and densities of the order of 100 g/cm^3, which translates into a 100-fold compression.

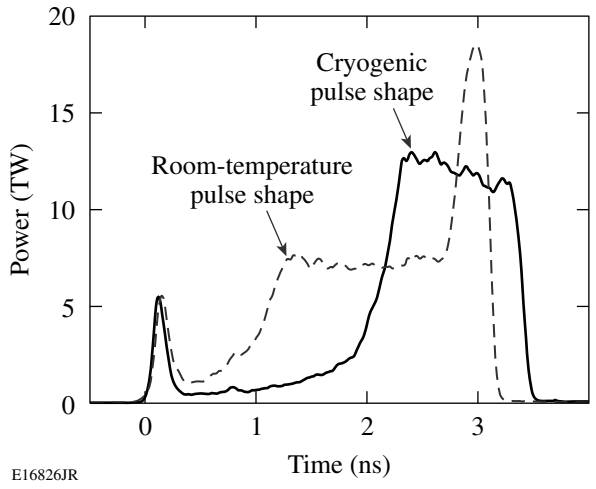

Figure 115.12
Laser pulse shapes used in the low-adiabat OMEGA cyrogenic (solid) and room-temperature (dashed) target implosions.

Fuel assembly in direct-drive cone-in-shell targets has been investigated using experiments on OMEGA in both indirect-[33] and direct-drive[34] geometries, including the achievable areal densities and filling the cone with plasma. Gas-tight targets were developed for the direct-drive experiments to be able to fill the targets with D_2 or D^3He, which makes it possible to use nuclear diagnostics to measure the areal density achieved in the implosion. The targets were 24- to 40-μm-thick CH shells of ~870-μm outer diameter, with a hollow gold cone with an opening angle of 70° or 35° inserted through a hole in the shell (Fig. 115.14).[34] A step on the cone defines the distance between the cone tip and the center of the shell, typically 30±10 μm. The cone has a thickness of ~100 μm outside the shell and 10 μm inside the shell and ends in a 30-μm-thick hyperbolic-shaped tip. For some experiments the cone tip was

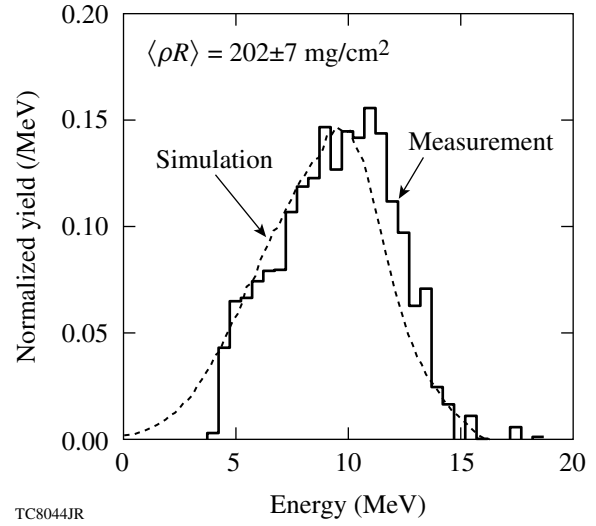

Figure 115.13
Measured secondary-proton spectrum (solid line) for the cryogenic target. The dashed line shows the calculated spectrum from the 1-D hydrocode.

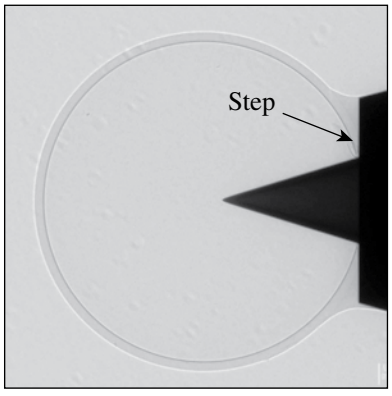

Figure 115.14
Radiograph of a gas-tight, fast-ignitor cone-in-shell target. A gold cone with an opening angle of 35° is inserted through a hole in a 24-μm-thick CH shell of ~870-μm outer diameter. A step on the cone defines the location of the cone tip at a distance of 30±10 μm to the center of the shell. It also provides a convenient interface to apply enough glue to make the assembly gas tight.

cut off to form a 15-μm-thick flat tip. Most experiments used 54 of the 60 OMEGA beams, at 351-nm wavelength, with a 1-ns square pulse and ~21 kJ of total energy or a highly shaped pulse of ~3-ns duration and ~20-kJ energy. For some experiments, 15 beams with a total energy of ~6 kJ were diverted to a backlighter foil and focused to a spot size of 600 μm. The target was irradiated using 35 of the remaining beams with ~11 kJ of laser energy.

X-ray framing cameras[35] were used to acquire backlit images of the fuel assembly around the cone tip. Figure 115.15 shows a backlit image of a cone-in-shell target (lower half) irradiated with a 1-ns square pulse at peak density compared to a 2-D *DRACO*[36] hydrodynamic simulation (upper half). The image shows a dense core ~100 μm from the cone tip, with lower-density plasma in between. An areal density of ~70 mg/cm^2 was measured for a 35° cone target using nuclear diagnostics—more than 60% of what a 1-D simulation predicts for an equivalent full sphere.[34] Mixing does not seem to be an issue in these direct-drive cone experiments,[34] and the hydro-efficiency penalty from the cone is not very big. A streaked optical pyrometer (SOP)[37] was used to investigate the filling of the inside of the cone. The high-pressure core plasma sends a shock wave through the gold cone that creates a plasma inside the cone when it breaks out. This could significantly increase the electron propagation distance. SOP uses an optical system that images the inside of the tip of the cone onto the slit of the streak camera with an ~10-μm spatial resolution and a 500-μm field of view. The breakout of the shock driven by the pressure from the core produces a short burst of light.

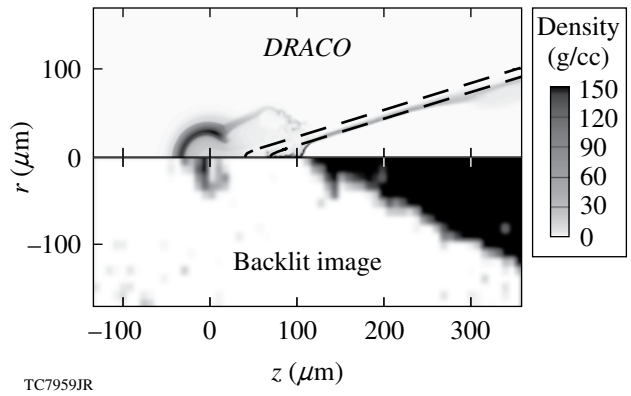

Figure 115.15
Backlit framing-camera image from a target filled with 10 atm of D_2 and imploded using a 1-ns square pulse at 11-kJ laser energy, compared to a 2-D *DRACO* radiation hydrodynamic code simulation.

Figure 115.16 shows a lineout through the center of the SOP trace from a 35° cone target with a 15-μm-thick flat tip irradiated by a highly shaped pulse at 20-kJ energy, as well as the areal density of the compressed core as predicted by the 2-D hydrocode *DRACO* and the drive-laser pulse shape. The shock signal starts just after the time of peak compression as calculated by *DRACO*. The absolute timing uncertainty of SOP is estimated to be ~100 ps. This shows that with the current designs the inside of the cone is free of plasma at the time when the short-pulse laser would propagate. Since the projected range for a 1-MeV electron in gold is of the order of ~50 μm (Ref. 38), the gold tip must be as thin as possible to avoid excessive energy loss of the fast electrons. In an optimized cryogenic capsule, the core would produce a lower pressure on the cone due to the lower average ionization of hydrogenic plasma compared to CH plasma.

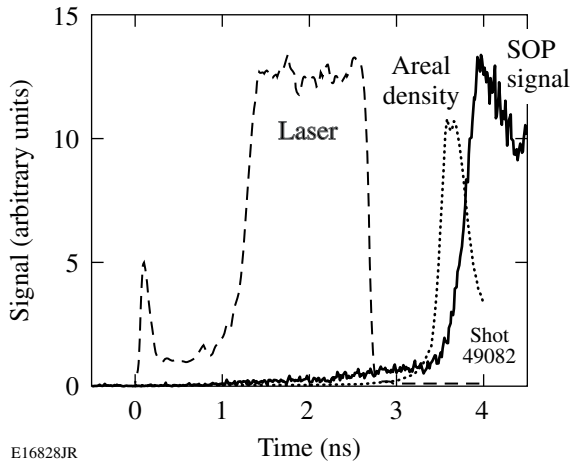

Figure 115.16
Lineout through the center of the SOP signal (solid line) of a cone-in-shell target with a 35° opening angle irradiated by a shaped pulse at 20 kJ. The dashed line shows the laser pulse power, and the dotted line represents the calculated evolution of the areal density.

Short-Pulse Experiments and Diagnostics

The conversion efficiency from laser energy into energetic electrons $\eta_{L\to e}$ has been measured using K-shell spectroscopy of reduced-mass Cu targets.[39] It has been shown that the normalized fast-electron–induced K_α yield from reduced-mass targets is approximately constant above 10^{18} W/cm^2 and can be readily used to infer $\eta_{L\to e}$ (Refs. 40 and 41). The heating of these reduced-mass targets is sufficient to affect the inner-shell fluorescence probabilities.[41] Ionization of the outer shells of copper at high temperature affects the M ⟶ K and the L ⟶ K transition probabilities and causes a deviation in the ratio of the emitted

number of K_β and K_α photons. This is used to infer the electron temperature of the target and allows the conversion efficiency $\eta_{L\to e}$ to be inferred independently from the absolute K_α yield by using a model for the equation of state of copper.[41]

The experiments have been performed on both the Rutherford Appleton Laboratory PW facility[42] and the Multi-Terawatt (MTW) laser at LLE.[43] The Vulcan PW laser delivers up to 500 J of energy with a pulse duration as short as 0.5 ps at a wavelength of 1.054 μm, focused by an *f*/3 off-axis parabola onto the target. Roughly 30% of the laser energy is contained in a 7-μm full width at half maximum (FWHM) spot. The MTW laser delivered 1- to 5-J, 1-ps pulses at a wavelength of 1.053 μm and was focused by an *f*/2 off-axis parabola at normal incidence to the target. The focal spot has an FWHM between 4 to 6 μm containing ~50% of the laser energy, with a peak intensity of 2×10^{19} W/cm^2.

Copper foils ranging between $20 \times 20 \times 2$ μm^3 and $500 \times 500 \times 50$ μm^3 were used as targets. They were mounted by using either a 17-μm-diam silicon carbide stalk or, in the case of the smallest targets, a pair of 1-μm-diam spider silk threads.

The K-shell line radiation was measured using a single-photon–counting spectrometer[44] based on an SI 800-145 x-ray back-illuminated, charge-coupled device (CCD).[45] Various copper filters between 75 to 150 μm were used to optimize the signal-to-background ratio of the K-shell emission. Figure 115.17(a) (Ref. 39) shows the measured conversion efficiency of laser energy into K_α photons emitted from $500 \times 500 \times 20$-μm^3 copper targets as a function of the laser intensity. The K_α photon yield increases up to intensities of 10^{18} W/cm^2 and stays constant at higher intensity. The data from Fig. 115.17 are compared to a model of K_α photon production, which assumes an exponentially distributed fast-electron spectrum $f(E) = \exp\left(-E/T_e\right)$, where T_e is calculated from the laser intensity through the ponderomotive scaling.[46]

$$T_e\,[\mathrm{MeV}] = 0.511\left[\left(1 + I_{18}\lambda_{\mu m}^2/1.37\right)^{0.5} - 1\right], \qquad (2)$$

where E is the electron energy, T_e is the electron temperature, I_{18} is the laser intensity in units of 10^{18} W/cm^2, and $\lambda_{\mu m}$ is the laser wavelength in microns. The energy loss of the fast electrons is calculated using the continuous slowing down for cold approximation solid-density copper.

The model assumes that all electrons are reflected at the target boundaries from electrostatic sheath fields[47,48] and deposit all their energy in the target (refluxing). Relativistic corrections to the copper K-shell ionization cross section[49] are included, and the only free parameter in the model is the conversion efficiency $\eta_{L\to e}$. A laser-to-electron energy-conversion efficiency $\eta_{L\to e}$ = (20±10)% can be inferred by comparing the experimental data with the predictions of this model. The discrepancies in the observed K_α yield at lower laser intensities are most likely due to the assumption of ponderomotive scaling, which breaks down at a laser irradiance below 10^{18} W/cm^2 μm^2 (Ref. 46).

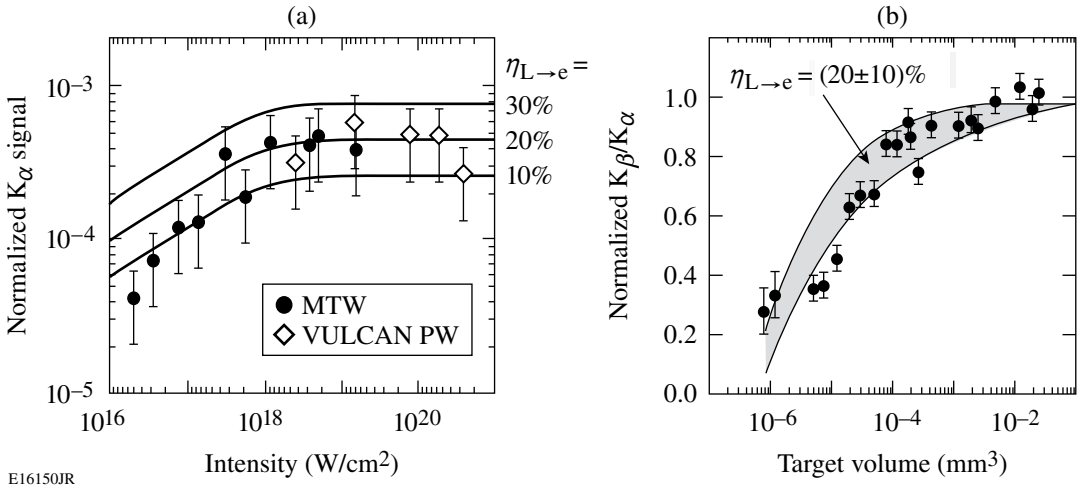

Figure 115.17
(a) Energy in K_α photons (normalized to the laser energy) emitted by a $500 \times 500 \times 20$-μm^3 copper target as a function of laser intensity. The curves correspond to the total calculated K_α yield at a given laser-to-electron-energy-conversion efficiency $\eta_{L\to e}$. (b) Ratio of the number of K_β to K_α photons (normalized to the cold material value) as a function of target volume. Numerical calculations of K_β/K_α are shown as a function of target volume caused by target heating, assuming $\eta_{L\to e}$ = (20±10)%.

Figure 115.17(b) (Ref. 39) shows the measurement of the change in the ratio of the number of emitted K_β and K_α photons $\left(K_\beta/K_\alpha\right)$ normalized to the cold material value as a function of the target volume at a constant laser intensity of 2×10^{19} W/cm^2. Numerical target-heating calculations using the implicit-hybrid particle-in-cell code *LSP*[50] infer the energy content of the fast electrons from the reduction in the ratio of K_β/K_α (Ref. 41). The collisional-radiative code *PrismSPECT*[51] was used to determine the target's ion-population distribution. Assuming a conversion efficiency of $\eta_{L\to e} = (20\pm10)\%$, the calculation reproduces the observed variation in the ratio $\left(K_\beta/K_\alpha\right)$ with target volume, which is consistent with the efficiencies inferred from the absolute K_α yield. This technique can be readily extended to laser energies on the multikilojoule level and pulse durations >10 ps on OMEGA EP, much closer to the fast-ignitor laser conditions as in the present small-scale experiments.

A promising technique that provides information about the transport of the energetic electrons generated in the short-pulse laser–plasma interaction is the measurement of transition radiation (TR).[52] TR is emitted when a charged particle passes through a refractive-index interface[53]—in this case, energetic electrons exiting the target into vacuum. The emitted electromagnetic energy is very small for a single electron. However, the laser-generated energetic-electron distribution typically has a highly correlated longitudinal electron-density structure, which leads to a considerable coherent enhancement, producing coherent transition radiation (CTR).[54] The two dominant electron-acceleration processes produce structures at different frequencies: resonance absorption[55] accelerates electrons into the target once every optical cycle, whereas the $\vec{v}\times\vec{B}$ force[46] accelerates electrons twice every optical cycle, generating a CTR signal at the first or second harmonic of the laser frequency, respectively. The spatial-intensity distribution and spectrum of the CTR emission measured at the backside of the target provide information about the electron transport, especially the spatial distribution and divergence of the coherent part of the electron distribution exiting the target and the slope or temperature of the longitudinal energy distribution.

A transition radiation diagnostic (TRD)[56] has been developed to acquire high-resolution images of the target's rear-side optical emission at the second harmonic ($\lambda \sim 527$ nm) for experiments conducted on the MTW laser. The optical design is shown in Fig. 115.18(a) (Ref. 56). A commercial 20× infinity corrected objective[57] collects the optical emission from the target's rear

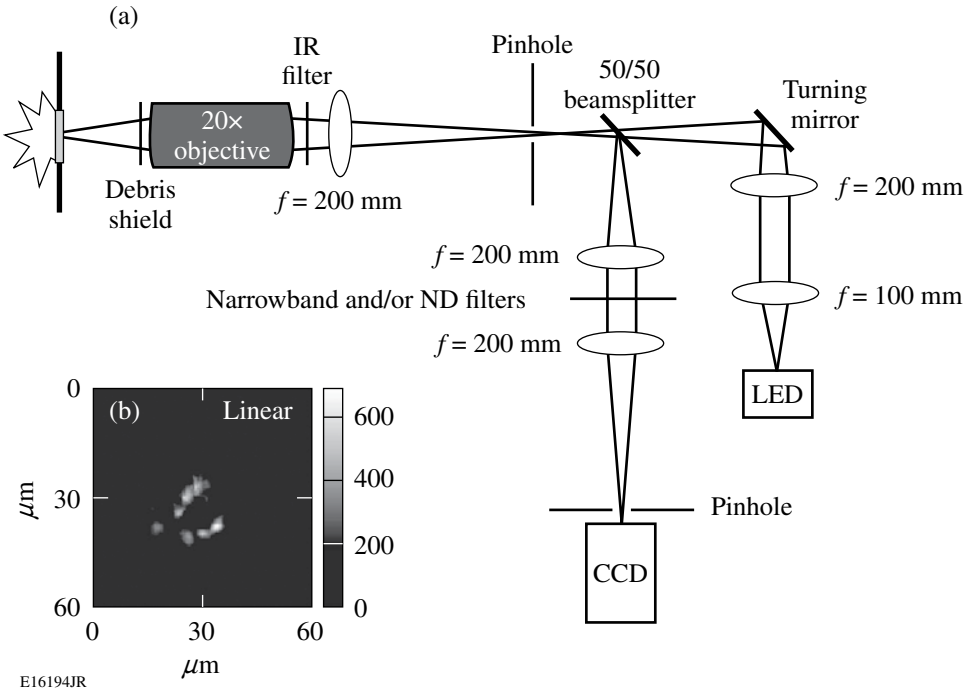

Figure 115.18

(a) Optical design of the transition radiation detector. A high-quality microscope objective and an optical system of three lenses image the rear surface of the target onto a CCD detector. Filters and pinholes are used to minimize background contributions. The right arm of the system is used for pre-shot focusing. (b) Image of the rear-side optical CTR emission from a 20-μm-thick aluminum foil. The scale is logarithmic and the intensity is expressed in arbitrary units. A number of ~2-μm-diam filaments are contained within a 15-μm-diam emission region.

surface. A sacrificial 150-μm-thick glass microscope cover protects the objective from target debris. The objective is mounted on a high-resolution (20-nm step), motorized, 1-D linear actuator. Filters prevent 1ω laser light from propagating and narrow the spectral acceptance of the optical system to a 24-nm band centered on λ = 529 nm. An optical system of three 200-mm-focal-length achromatic lenses and a 50/50 beam splitter transports the light to a CCD camera. This Spectral Instruments (SI) 800-series CCD uses a front-illuminated chip with 1024 × 1024, 13.5-μm × 13.5-μm pixels, thermo-electrically cooled to –40°C to minimize the dark current.[45] To obtain consistent high-resolution images of the target's rear-surface emission, the microscope objective must be positioned with ~1-μm precision relative to the rear surface of the target since its depth of focus is only 1.6 μm. The second arm of the optical system sends light from an ultrabright green LED (light-emitting diode) through the beam splitter and collection optics onto the target. The light reflected off small-scale surface features on the rear surface of the target is imaged onto the CCD camera. These features are used to obtain the best focus position for the objective. Extensive tests have shown that the optical resolution of the TRD in the optimum focus position is limited only by the CCD pixel size to ~1.4 μm over the full field of view.[56] The pinholes shown in Fig. 115.18(a) minimize the propagation of stray light through the system. The background from hard x rays is minimized by folding the optical system through 90° so that the detector can be shielded behind a 10-cm-thick lead brick wall. An additional 2-mm-thick lead shield is placed around the CCD camera to minimize single hits by scattered x rays arriving from the rear and top sides. This shielding reduces the background by more than an order of magnitude on the CCD detector.

The TRD has been used in several experiments to diagnose electron transport in solid materials. Figure 115.18(b) shows a coherent transition radiation image from the rear side of a 30-μm aluminum foil. A 5-J, 500-fs pulse from the MTW laser was focused to an ~4-μm-radius spot on the target, corresponding to a laser intensity of ~10^{19} W/cm^2. The diameter of the rear-side coherent optical emission is less than 20 μm. Structures, indicative of electron-beam filaments, superimposed on a ring-like feature are clearly visible in this region with a spatial full width at half maximum of ~2 μm. These structures are indicative of electron-beam filamentation.[58]

This instrument will be used extensively on the MTW to study the divergence and potential breakup of the electron flow through the target and to infer the slope temperature of the longitudinal electron temperature.[54] Based on the experience with this TRD on the MTW, a detector suitable for OMEGA EP is being designed.

Simulations

To understand the interaction of the electron beam with the target and its effect on the neutron production in both integrated FI experiments on OMEGA EP and high-gain FI targets, the 2-D axisymmetric radiation hydrocode *DRACO* was coupled with the 2-D/3-D hybrid particle-in-cell code *LSP*.[50] *DRACO* simulates the target implosion and the hydrodynamic reaction of the target to the fast-electron heating, using a realistic tabular equation of state, radiation transport, and α-particle transport in DT targets. *LSP* is used to simulate hot-electron transport including self-generated electromagnetic fields. The laser–plasma interaction that creates the energetic electrons is not modeled in *LSP*; a hot-electron distribution is created by promoting background electrons to higher energy according to a theoretical prescription such as Wilks's scaling law[46] and a constant conversion efficiency. The transport of hot electrons is currently modeled in *LSP* only from the end of the cone tip for cone-in-shell targets to the dense core, where the hot-electron energy is absorbed; the cone itself and the electron transport in the cone are not simulated.

The *LSP* part of the simulation starts when the high-energy, short-pulse laser is injected using the hydrodynamic profiles predicted by *DRACO*. *LSP* runs for a short time (~1 ps) during which the hydrodynamic evolution is minimal, and it generates a time history of hot-electron energy deposition. *DRACO* then runs for the same time, using the energy deposition calculated by *LSP* as an additional energy source in the temperature equation. The hydrodynamic profiles in *LSP* are updated according to the *DRACO* results, while the hot-electron distributions and the electromagnetic fields in *LSP* are left unchanged. *DRACO* and *LSP* are run together for the duration of the high-energy petawatt pulse. The hydrodynamic reaction of the target after the high-energy petawatt pulse is simulated by *DRACO*.

The first simulations of integrated fast-ignitor experiments planned for the combined OMEGA/OMEGA EP Laser System used 40-μm-thick CD shells of ~870-μm outer diameter, a gold cone with an opening angle of 35° and a tip thickness of 15 μm, irradiated by a highly shaped laser pulse of ~3-ns duration and ~20-kJ energy. Currently, radiation transport is not included in the hydro simulation, which leads to an overestimate of the compressed target density. The OMEGA EP laser is assumed to deliver 2.6 kJ in a 10-ps pulse into the cone, which is translated into a hot-electron distribution assuming a 30% conversion efficiency and a slope temperature according to the Wilks scaling. The hot electrons are given a Gaussian profile in the radial direction with a diameter of 20 μm (FWHM) and an angular spread of 20° (half-angle, FWHM). Figure 115.19 shows results

from these simulations as 2-D maps of (a) the plasma density, (b) hot-electron density, and (d) the azimuthal magnetic field in the r–z plane 6 ps after the beginning of the hot-electron pulse. Figure 115.19(c) shows the total plasma-temperature increase caused by the heating from hot electrons at the end of the laser pulse. The hot electrons are seen to be well collimated by the resistive magnetic field generated by the electron beam despite the high initial divergence. The maximum temperature increase in the core is of the order of 1 keV.

This *LSP*/*DRACO* code combination scheme was also used to perform integrated high-gain, fast-ignition simulations. An optimized spherically symmetric target imploded with a highly shaped 300-kJ compression pulse[7] was used, and the electron beam was injected 125 μm from the target center. The electron beam had a square profile in time with a duration of 10 ps and a Gaussian profile in the radial direction with a diameter of 30 μm (FWHM). A Maxwellian distribution was assumed for the electrons with a mean energy of 2 MeV and an angular spread of 20° (half-angle, FWHM). In contrast to the simulations of the experiments on OMEGA EP, these simulations show what is believed to be resistive filamentation, similar to observations in the hybrid simulations of Honrubia and Meyer-ter-Vehn.[59] For the given parameters, 43 kJ of energetic electrons were required for ignition, resulting in a gain of ~100. When the effect of the magnetic field on beam electrons was artificially suppressed, the minimum electron-beam energy required for ignition increased to 96 kJ, demonstrating the beneficial effect of the resistive magnetic field.

Summary

A comprehensive scientific program is being pursued at LLE to investigate the fast-ignitor concept for inertial confinement fusion. The combined OMEGA/OMEGA EP Laser Facility provides the experimental infrastructure for these investigations. The OMEGA EP laser was completed in April 2008. Two of the four OMEGA EP beamlines can operate in short-pulse mode, with up to 2.6 kJ each at a 10-ps pulse duration. These beams can be routed into either the OMEGA EP chamber or combined collinearly into the existing OMEGA target chamber for integrated fast-ignitor experiments. Fuel-assembly experiments on OMEGA with both room-temperature and cryogenic targets have achieved high fuel-areal densities of ~200 mg/cm^2, sufficient to stop the MeV electrons produced by the short-pulse laser. Experiments on the fuel assembly of cone-in-shell targets showed only a small deterioration of achievable areal density. The measured areal density was more than 60% of what a 1-D simulation predicts for an equivalent full sphere. The conversion efficiency from laser energy to fast electrons was measured using two independent experimental methods on both LLE's MTW laser and the RAL Vulcan Petawatt and found to be ~20% at intensities >10^{18} W/cm^2. A high-resolution (1.4-μm) TRD measures the coherent transition radiation from the rear side of a solid target, providing insight into the hot-electron transport. Simulation of both full-scale fast-ignition experiments and near-term integrated experiments on OMEGA, using a combination of a radiation hydrocode (*DRACO*) and a hybrid particle-in-cell code (*LSP*), shows the beneficial effects of the resistive magnetic fields generated by the propagation of the

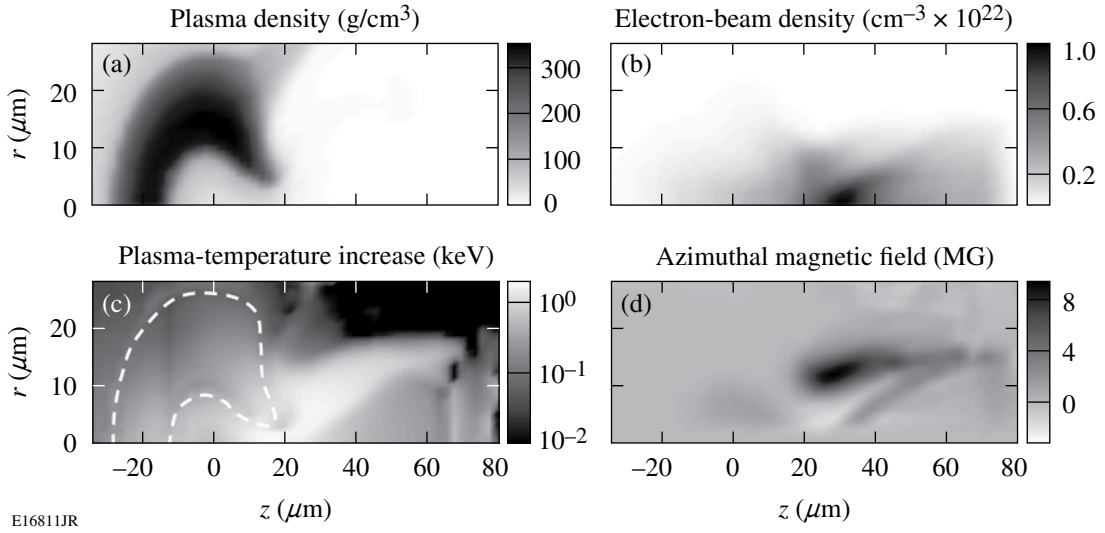

Figure 115.19
Snapshots of the (a) plasma density, (b) hot-electron density, and (d) the azimuthal magnetic field 6 ps after the beginning of the hot-electron pulse, for near-term, integrated fast-ignitor experiments on OMEGA. The maximum increase in plasma temperature (c) at the end of the pulse is ~1 keV

energetic electron into the high-density core. A decrease of the energy required to ignite a target imploded by a 300-kJ UV laser from ~100-kJ electron energy to ~40-kJ electron energy due to the magnetic fields was observed in simulations of full-scale fast-ignition targets. Simulations of fast-ignitor experiments with room-temperature cone-in-shell targets on OMEGA EP showed a temperature increase of up to 1 keV in the core with the short-pulse-laser–produced energetic electrons heating the target. Integrated experiments with room-temperature targets on the combined OMEGA/OMEGA EP Laser Facility are scheduled for the summer of 2008.

ACKNOWLEDGMENT

This work was supported by the U.S. Department of Energy Office of Inertial Confinement Fusion under Cooperative Agreement No. DE-FC52-08NA28302, Fusion Science Center, Office of Inertial Fusion Energy Science No. DE-FC02-ER54789, the University of Rochester, and the New York State Energy Research and Development Authority. The support of DOE does not constitute an endorsement by DOE of the views expressed in this article.

REFERENCES

1. N. G. Basov, S. Yu. Gus'kov, and L. P. Feokistov, J. Sov. Laser Res. **13**, 396 (1992).
2. M. Tabak *et al*., Phys. Plasmas **1**, 1626 (1994).
3. R. Kodama *et al*., Nature **412**, 798 (2001).
4. R. Kodama *et al*., Nature **418**, 933 (2002).
5. J. D. Lindl, R. L. McCrory, and E. M. Campbell, Phys. Today **45**, 32 (1992).
6. K. Yasuike *et al*., Rev. Sci. Instrum. **72**, 1236 (2001).
7. R. Betti, K. Anderson, J. Knauer, T. J. B. Collins, R. L. McCrory, P. W. McKenty, and S. Skupsky, Phys. Plasmas **12**, 042703 (2005).
8. J. Nuckolls *et al*., Nature **239**, 139 (1972).
9. C. K. Li and R. D. Petrasso, Phys. Rev. E **70**, 067401 (2004).
10. R. B. Stephens *et al*., Phys. Rev. E **69**, 066414 (2004).
11. Y. Kitagawa *et al*., Phys. Plasmas **9**, 2202 (2002).
12. P. A. Norreys *et al*., Phys. Plasmas **7**, 3721 (2000).
13. L. J. Waxer, D. N. Maywar, J. H. Kelly, T. J. Kessler, B. E. Kruschwitz, S. J. Loucks, R. L. McCrory, D. D. Meyerhofer, S. F. B. Morse, C. Stoeckl, and J. D. Zuegel, Opt. Photonics News **16**, 30 (2005).
14. T. R. Boehly, D. L. Brown, R. S. Craxton, R. L. Keck, J. P. Knauer, J. H. Kelly, T. J. Kessler, S. A. Kumpan, S. J. Loucks, S. A. Letzring, F. J. Marshall, R. L. McCrory, S. F. B. Morse, W. Seka, J. M. Soures, and C. P. Verdon, Opt. Commun. **133**, 495 (1997).
15. C. Stoeckl, C. Chiritescu, J. A. Delettrez, R. Epstein, V. Yu. Glebov, D. R. Harding, R. L. Keck, S. J. Loucks, L. D. Lund, R. L. McCrory, P. W. McKenty, F. J. Marshall, D. D. Meyerhofer, S. F. B. Morse, S. P. Regan, P. B. Radha, S. Roberts, T. C. Sangster, W. Seka, S. Skupsky, V. A. Smalyuk, C. Sorce, J. M. Soures, R. P. J. Town, J. A. Frenje, C. K. Li, R. D. Petrasso, F. H. Séguin, K. Fletcher, S. Padalino, C. Freeman, N. Izumi, R. Lerche, and T. W. Phillips, Phys. Plasmas **9**, 2195 (2002).
16. T. C. Sangster, R. Betti, R. S. Craxton, J. A. Delettrez, D. H. Edgell, L. M. Elasky, V. Yu. Glebov, V. N. Goncharov, D. R. Harding, D. Jacobs-Perkins, R. Janezic, R. L. Keck, J. P. Knauer, S. J. Loucks, L. D. Lund, F. J. Marshall, R. L. McCrory, P. W. McKenty, D. D. Meyerhofer, P. B. Radha, S. P. Regan, W. Seka, W. T. Shmayda, S. Skupsky, V. A. Smalyuk, J. M. Soures, C. Stoeckl, B. Yaakobi, J. A. Frenje, C. K. Li, R. D. Petrasso, F. H. Séguin, J. D. Moody, J. A. Atherton, B. D. MacGowan, J. D. Kilkenny, T. P. Bernat, and D. S. Montgomery, Phys. Plasmas **14**, 058101 (2007).
17. P. W. McKenty, V. N. Goncharov, R. P. J. Town, S. Skupsky, R. Betti, and R. L. McCrory, Phys. Plasmas **8**, 2315 (2001).
18. Y. Lin, T. J. Kessler, and G. N. Lawrence, Opt. Lett. **21**, 1703 (1996).
19. S. Skupsky and R. S. Craxton, Phys. Plasmas **6**, 2157 (1999).
20. T. R. Boehly, V. A. Smalyuk, D. D. Meyerhofer, J. P. Knauer, D. K. Bradley, R. S. Craxton, M. J. Guardalben, S. Skupsky, and T. J. Kessler, J. Appl. Phys. **85**, 3444 (1999).
21. G. H. Miller, E. I. Moses, and C. R. Wuest, Opt. Eng. **43**, 2841 (2004).
22. M. A. Rhodes *et al*., Appl. Opt. **34**, 5312 (1995).
23. B. W. Shore *et al*., J. Opt. Soc. Am. A **14**, 1124 (1997).
24. T. J. Kessler, J. Bunkenburg, H. Huang, A. Kozlov, and D. D. Meyerhofer, Opt. Lett. **29**, 635 (2004).
25. T. C. Sangster, V. N. Goncharov, P. B. Radha, V. A. Smalyuk, R. Betti, R. S. Craxton, J. A. Delettrez, D. H. Edgell, V. Yu. Glebov, D. R. Harding, D. Jacobs-Perkins, J. P. Knauer, F. J. Marshall, R. L. McCrory, P. W. McKenty, D. D. Meyerhofer, S. P. Regan, W. Seka, R. W. Short, S. Skupsky, J. M. Soures, C. Stoeckl, B. Yaakobi, D. Shvarts, J. A. Frenje, C. K. Li, R. D. Petrasso, and F. H. Séguin, Phys. Rev. Lett. **100**, 185006 (2008).
26. W. Theobald, R. Betti, C. Stoeckl, K. S. Anderson, J. A. Delettrez, V. Yu. Glebov, V. N. Goncharov, F. J. Marshall, D. N. Maywar, R. L. McCrory, D. D. Meyerhofer, P. B. Radha, T. C. Sangster, W. Seka, D. Shvarts, V. A. Smalyuk, A. A. Solodov, B. Yaakobi, C. D. Zhou, J. A. Frenje, C. K. Li, F. H. Séguin, R. D. Petrasso, and L. J. Perkins, Phys. Plasmas **15**, 056306 (2008).
27. V. N. Goncharov, T. C. Sangster, P. B. Radha, R. Betti, T. R. Boehly, T. J. B. Collins, R. S. Craxton, J. A. Delettrez, R. Epstein, V. Yu. Glebov, S. X. Hu, I. V. Igumenshchev, J. P. Knauer, S. J. Loucks, J. A. Marozas, F. J. Marshall, R. L. McCrory, P. W. McKenty, D. D. Meyerhofer, S. P. Regan, W. Seka, S. Skupsky, V. A. Smalyuk, J. M. Soures, C. Stoeckl, D. Shvarts, J. A. Frenje, R. D. Petrasso, C. K. Li, F. Séguin, W. Manheimer, and D. G. Colombant, Phys. Plasmas **15**, 056310 (2008).
28. V. N. Goncharov, J. P. Knauer, P. W. McKenty, P. B. Radha, T. C. Sangster, S. Skupsky, R. Betti, R. L. McCrory, and D. D. Meyerhofer, Phys. Plasmas **10**, 1906 (2003).

29. C. K. Li, D. G. Hicks, F. H. Séguin, J. A. Frenje, R. D. Petrasso, J. M. Soures, P. B. Radha, V. Yu. Glebov, C. Stoeckl, D. R. Harding, J. P. Knauer, R. L. Kremens, F. J. Marshall, D. D. Meyerhofer, S. Skupsky, S. Roberts, C. Sorce, T. C. Sangster, T. W. Phillips, M. D. Cable, and R. J. Leeper, Phys. Plasmas **7**, 2578 (2000).

30. J. Delettrez, R. Epstein, M. C. Richardson, P. A. Jaanimagi, and B. L. Henke, Phys. Rev. A **36**, 3926 (1987).

31. K. Anderson and R. Betti, Phys. Plasmas **11**, 5 (2004).

32. C. D. Zhou, W. Theobald, R. Betti, P. B. Radha, V. A. Smalyuk, D. Shvarts, V. Yu. Glebov, C. Stoeckl, K. S. Anderson, D. D. Meyerhofer, T. C. Sangster, C. K. Li, R. D. Petrasso, J. A. Frenje, and F. H. Séguin, Phys. Rev. Lett. **98**, 025004 (2007).

33. R. B. Stephens *et al*., Phys. Rev. Lett. **91**, 185001 (2003).

34. C. Stoeckl, T. R. Boehly, J. A. Delettrez, S. P. Hatchett, J. A. Frenje, V. Yu. Glebov, C. K. Li, J. E. Miller, R. D. Petrasso, F. H. Séguin, V. A. Smalyuk, R. B. Stephens, W. Theobald, B. Yaakobi, and T. C. Sangster, Phys. Plasmas **14**, 112702 (2007).

35. D. K. Bradley *et al*., Rev. Sci. Instrum. **66**, 716 (1995).

36. P. B. Radha, T. J. B. Collins, J. A. Delettrez, Y. Elbaz, R. Epstein, V. Yu. Glebov, V. N. Goncharov, R. L. Keck, J. P. Knauer, J. A. Marozas, F. J. Marshall, R. L. McCrory, P. W. McKenty, D. D. Meyerhofer, S. P. Regan, T. C. Sangster, W. Seka, D. Shvarts, S. Skupsky, Y. Srebro, and C. Stoeckl, Phys. Plasmas **12**, 056307 (2005).

37. J. A. Oertel *et al*., Rev. Sci. Instrum. **70**, 803 (1999).

38. P. K. Gupta *et al*., Appl. Phys. Lett. **39**, 32 (1981).

39. P. M. Nilson, W. Theobald, J. Myatt, C. Stoeckl, M. Storm, O. V. Gotchev, J. D. Zuegel, R. Betti, D. D. Meyerhofer, and T. C. Sangster, Phys. Plasmas **15**, 056308 (2008).

40. W. Theobald, K. Akli, R. Clarke, J. Delettrez, R. R. Freeman, S. Glenzer, J. Green, G. Gregori, R. Heathcote, N. Izumi, J. A. King, J. A. Koch, J. Kuba, K. Lancaster, A. J. MacKinnon, M. Key, C. Mileham, J. Myatt, D. Neely, P. A. Norreys, H.-S. Park, J. Pasley, P. Patel, S. P. Regan, H. Sawada, R. Shepherd, R. Snavely, R. B. Stephens, C. Stoeckl, M. Storm, B. Zhang, and T. C. Sangster, Phys. Plasmas **13**, 043102 (2006).

41. J. Myatt, W. Theobald, J. A. Delettrez, C. Stoeckl, M. Storm, T. C. Sangster, A. V. Maximov, and R. W. Short, Phys. Plasmas **14**, 056301 (2007).

42. C. N. Danson *et al*., Nucl. Fusion **44**, S239 (2004).

43. V. Bagnoud, I. A. Begishev, M. J. Guardalben, J. Puth, and J. D. Zuegel, Opt. Lett. **30**, 1843 (2005).

44. C. Stoeckl, W. Theobald, T. C. Sangster, M. H. Key, P. Patel, B. B. Zhang, R. Clarke, S. Karsch, and P. Norreys, Rev. Sci. Instrum. **75**, 3705 (2004).

45. Spectral Instruments, Tucson, AZ 85745.

46. S. C. Wilks *et al*., Phys. Rev. Lett. **69**, 1383 (1992).

47. A. J. Mackinnion *et al*., Phys. Rev. Lett. **88**, 215006 (2002).

48. Y. Sentoku *et al*., Phys. Rev. Lett. **90**, 155001 (2003).

49. H. Kolbenstvedt, J. Appl. Phys. **38**, 4785 (1967).

50. D. R. Welch *et al*., Nucl. Instrum. Methods Phys. Res. A **464**, 134 (2001).

51. Prism Computational Sciences, Inc., Madison, WI 53711.

52. S. D. Baton *et al*., Phys. Rev. Lett. **91**, 105001 (2003).

53. V. L. Ginzburg, Phys.-Usp. **39**, 973 (1996).

54. J. Zheng *et al*., Phys. Plasmas **10**, 2994 (2003).

55. W. L. Kruer, *The Physics of Laser Plasma Interactions*, Frontiers in Physics (Westview Press, Boulder, CO, 2003), pp. 39–43.

56. M. Storm, C. Guo, D. D. Meyerhofer, J. Myatt, T. C. Sangster, and C. Stoeckl, "Relativistic Electron-Beam Transport Measurements," to be published in Review of Scientific Instruments.

57. K. Miyamoto, *Plasma Physics for Nuclear Fusion*, Revised (MIT Press, Cambridge, MA, 1989).

58. L. Gremillet, G. Bonnaud, and F. Amiranoff, Phys. Plasmas **9**, 941 (2002).

59. J. J. Honrubia and J. Meyer-ter-Vehn, Nucl. Fusion **46**, L25 (2006).

A Focal-Spot Diagnostic for On-Shot Characterization of High-Energy Petawatt Lasers

Introduction

Knowledge of the laser focus is an essential part of accurately controlling and interpreting target experiments using petawatt-class lasers.[1–9] Large-scale lasers present significant challenges for the development of focal-spot diagnostics. Their focal spots can be highly structured due to the complexity of systems containing hundreds of optical surfaces. Furthermore, high-energy petawatt lasers typically require adaptive and tiled optics that must be configured correctly for a successful target shot.[10–12] Focal-spot characterization on each full-energy shot is a necessity and the only way to capture effects such as thermally induced aberrations in the amplifiers.

Depending on the target experiment, the quantity of interest may range from the focal-spot width to an analysis of encircled energy at a given plane, to a full characterization of the focal volume along an extended interaction region. Direct measurement of the focus at full energy without interfering with the target experiment is impractical, if not impossible, due to the extreme intensities at focus. One option is to precharacterize the near-field wavefront after propagation through focus, from which the focal volume is obtained using a diffraction calculation.[13] This article demonstrates a simplified near-field approach that does not rely on wavefront sensing in the target chamber and is therefore more suited to the complexity of high-energy petawatt lasers. Results are reported for an on-shot focal-spot diagnostic (FSD) for OMEGA EP, a high-energy petawatt-class laser that was recently activated at LLE.[1] The following three sections describe (1) the FSD, (2) the experiments used to qualify the FSD by comparison to direct measurement at low energy, and (3) results for high-energy target shots.

Diagnostic Concept and Design

1. Focal-Spot Diagnostic (FSD)

The FSD characterizes full-energy shots using high-resolution measurements of the near-field wavefront and fluence. The time-integrated focal spot at the target is calculated numerically from these measurements using standard diffraction theory.[14] Direct measurements of the full beam without interfering with the target shot are not practical due to its high energy (up to 2.6 kJ on target) and large size (400×400 mm^2). The FSD, like the other on-shot laser diagnostics, measures a lower-energy sample of the main beam that is attenuated and down-collimated to a more convenient beam size (12×12 mm^2). Careful calibration is necessary to ensure that measurements made on the sample beam reflect the main beam at focus. Therefore, a critical part of the FSD is the cross-calibration of the wavefront sensor measurements to a reference surface centered on the target location, from which the optical fields are numerically propagated.

Figure 115.20 shows a schematic of one of the short-pulse beamlines in OMEGA EP, necessary for understanding how the FSD was implemented and qualified. The front end of the laser system uses an optical parametric chirped-pulse amplifier (OPCPA) to produce stretched pulses (250 mJ, square 8-nm spectrum, 5 Hz).[15] For target shots, these pulses are amplified using a multipass Nd:glass amplifier. A tiled-grating compressor (three tiles per grating, four gratings) is used to compress the pulses. A deformable mirror corrects compressor aberrations and pre-corrects aberrations in the transport and the off-axis parabolic (OAP) focusing mirror ($f = 1.046$ m, $f/2$). A diagnostic pickoff mirror reflects 99% of the compressed pulse energy toward the target chamber as the main beam and transmits the remainder as a sample beam for the laser diagnostics package. The wavefront sensor (WFS) used by the FSD for each compressor is one of more than a dozen laser diagnostics used to characterize the on-shot beam.

The WFS chosen for OMEGA EP is a Shack–Hartmann sensor,[16] which is positioned at an image plane conjugate to the fourth compressor grating. It has a 133×133-lenslet array with a 14×14-mm^2 charge-coupled-device (CCD) sensor.[17] A local wavefront gradient as high as 15 mrad can be measured. The accuracy of the defocus term was measured to be better than 0.01 waves at 1.053 μm, and the relative error in astigmatism was less than 2%. The accuracy of measuring higher-order aberrations was studied using sinusoidal phase plates (one-wave peak-to-valley). Wavefront measurements up to 25% of the maximum spatial frequency were confirmed to have less

than 1% discrepancy with interferometric measurements of the phase plates. Measurements at higher spatial frequencies were limited by the maximum slope capability of the WFS.

The FSD must be calibrated to numerically transfer the sample-beam measurement at the sensor to a spherical reference surface in the target chamber that is centered on the intended focal-spot location. One part of this calibration is to precisely measure the amount of demagnification during the four down-collimation and imaging stages from the diagnostic mirror to the WFS. Another part is to measure the difference between (a) sample-beam aberrations that are artifacts in the on-shot measurement that must be subtracted and (b) aberrations in the main beam path that are after the diagnostic mirror and so must be added to the on-shot measurement. This difference, the transfer wavefront (ΔW_{trans}), is applied to correct the on-shot measurement before calculating the focal spot.

The transfer wavefront is measured by using two separate laser sources to probe the back end of the laser system, as shown in Fig. 115.21. The sample path from the WFS to an actuated compressor alignment mirror (CAM) and back is characterized using a laser source that is included in the diagnostics. The measured wavefront is

$$W_1 = W_{S0} + 2W_S , \tag{1}$$

where W_{S0} is the measured source wavefront and W_S is the single-pass aberration in the sample path to the CAM. The path from the target focus back to the WFS is characterized

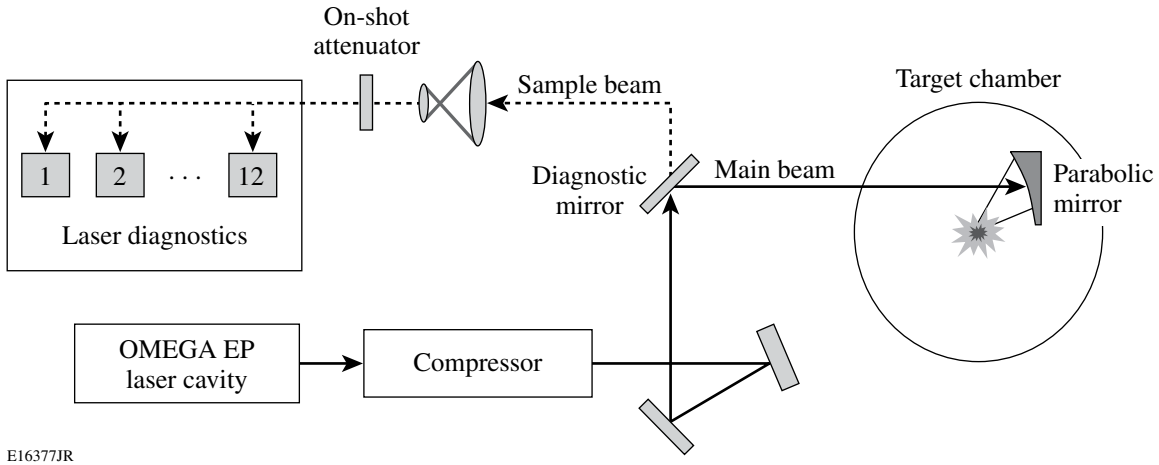

Figure 115.20
Overview of OMEGA EP, showing the relative location of the main laser beam and the sample beam used by diagnostics for on-shot measurement of the laser properties. The focal-spot diagnostic wavefront sensor is one of many laser diagnostics that characterize the sample beam.

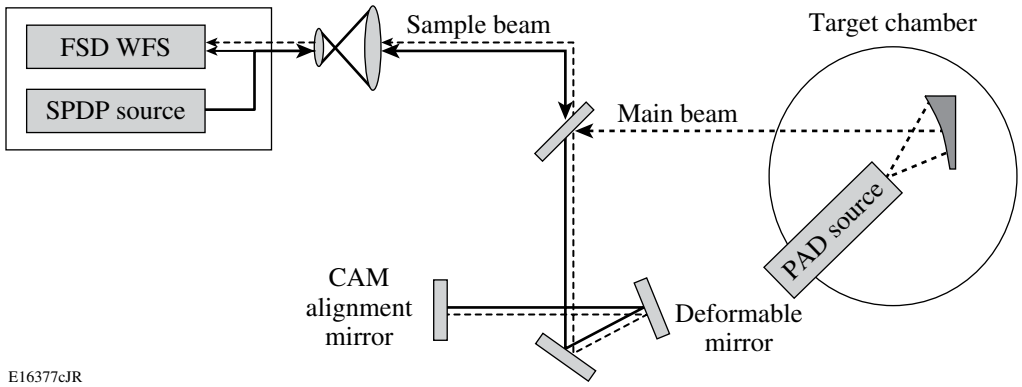

Figure 115.21
Schematic showing probe lasers used to calibrate the FSD.

using a back-propagating point source positioned at the desired focal-spot location. On OMEGA EP, the parabola alignment diagnostic (PAD) provides this point source. The measured wavefront is

$$W_2 = T^{-1}\left(W_{M0}\right) + W_M + W_S\,, \tag{2}$$

where W_{M0} is the measured point-source wavefront and W_M represents the main-path aberrations to the CAM. The inverse transformation $T^{-1}(\ldots)$ may be necessary to account for geometric distortion T produced by the focusing element, such as that due to low-f-number OAP's.[18] The transfer wavefront is given by

$$\Delta W_{\text{trans}} = W_M - W_S = W_1 - W_2 + W_{S0} - T^{-1}\left(W_{M0}\right). \tag{3}$$

Results from the transfer wavefront measurement for the OMEGA target chamber are shown in Fig. 115.22.

In principle, other approaches could be used to measure ΔW_{trans}. For example, one could use a single laser source and add a second WFS to measure the wavefront of the converging beam directly in the target chamber.[13] In this case additional steps would be needed to ensure that the resulting measurements were correctly scaled and registered before calculating ΔW_{trans}. With this single WFS approach, W_1 and W_2 are automatically registered in transverse alignment and in the image plane that is conjugate to the sensor. Furthermore, for a system as complex as OMEGA EP, it is simpler to produce a backward-propagating point source inside a target chamber than it is to provide accurate, high-resolution wavefront measurements of a forward-propagating, focusing probe beam.

After a shot, the field measured at the wavefront sensor is calibrated to a spherical reference surface centered on the target location by adding ΔW_{trans}. This field is numerically propagated to the target plane. If the f number of the OAP exceeds unity, a scalar field approximation is sufficient[18] and the diffraction calculation reduces to a two-dimensional Fourier transformation. One advantage of this field-based approach is that the irradiance can be calculated at any plane relative to the target by changing the diffraction calculation. Once the irradiance is calculated, it is straightforward to calculate the encircled energy as a function of radius.

One limitation of this approach is that it is strictly valid only if there is no chromatic variation of the transfer or on-shot wavefronts. The wavefront reported by a Shack–Hartmann sensor is a spectrally weighted average. Effects such as longitudinal chromatic aberration that has not been fully compensated[19] or angular dispersion from stretcher or compressor misalignment,[12] once quantified using independent techniques, can be included in the post-shot calculation.[20]

2. Focal-Spot Microscope for Direct Measurement at Low Energies

A custom focal-spot microscope (FSM) was built to validate the accuracy of the FSD. It provides a direct measurement of the focus in the OMEGA target chamber with spatial resolution of 0.36 μm per pixel and sufficient dynamic range to capture the diffuse low-intensity spray around the main focal spot that, when integrated, can represent a significant fraction of the total energy. Although not able to be used on a full-energy shot, the FSM has enough internal attenuation (6.0 OD) to safely measure focused pulses produced by the OMEGA EP front end,

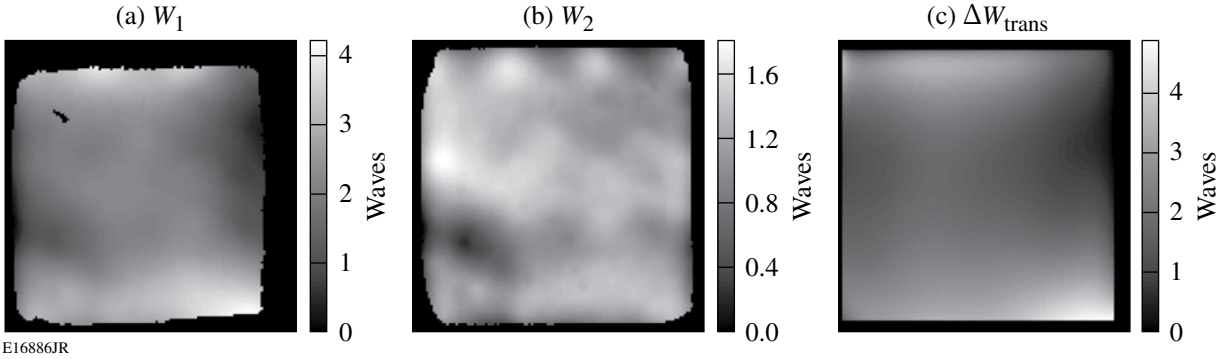

Figure 115.22
Measured transfer wavefront (in units of waves) obtained using two probe sources. (a) W_1, with the target chamber source (PAD), (b) W_2, with the diagnostic package source, and (c) ΔW_{trans}, transfer wavefront after source errors have been subtracted and a Legendre modal fit has been used to extrapolate to an extended pupil region.

with sufficient energy available after the diagnostic mirror for the FSD WFS to make a simultaneous measurement.

Figure 115.23 shows a schematic of the FSM that was installed in the OMEGA target chamber, using the ten-inch manipulator (TIM) that opposed the OAP. The microscope objective was optimized for near-infrared (10×, N.A. = 0.26, f = 20 mm), with a damage threshold of 20 mJ/cm^2 and a long working distance (30 mm), making it suitable for laser focus characterization. When combined with the 660-mm-focal-length tube lens, the total magnification of the system was 33×. Between the objective and tube lens were a wedged vacuum window, a pair of neutral-density filters with a total optical density (OD) of 4.0, and a beam splitter at 45° that was also made from neutral-density filter glass (2.0 OD). The scientific-grade camera used a one-megapixel, front-illuminated CCD chip cooled to –20°C, giving a read-noise limited dynamic range of 14.5 bits. The entire FSM was contained in an air bubble to permit its use with the target chamber at vacuum. Care was taken with internal surface preparations and baffling to minimize stray light and scattering within the FSM that could reduce the instrument's dynamic range.

The FSM was aligned to the intended focus location using the same techniques as used with the PAD point source. First, a reflective sphere was aligned precisely so that it was centered on the desired focal-spot location. Then, a collimated fiber-fed beam at 1053 nm was focused by the FSM objective onto the surface of the sphere. The FSM position was adjusted so that the focusing beam was normal to the sphere surface, at which point the FSM focal plane was coincident with the intended focus location. Under these conditions light reflected back off the sphere into the FSM appears tightly focused at the CCD. Coarse positioning was done using the TIM; fine positioning was achieved using the piezo and mechanical actuators of a motion-control system.

FSD Qualification Results

The focal-spot diagnostic was qualified using a sequence of experiments designed to compare measurements made by the FSD and FSM. The laser source for these experiments was the front-end system for OMEGA EP after propagation through the entire beamline and compression chamber into the OMEGA target chamber. Gain narrowing by the Nd:glass amplifiers during a full-energy shot reduces the square 8-nm spectrum to a 3.3-nm-wide Gaussian-like spectrum. Therefore, the impact of any chromatic aberrations and angular dispersion on the focal spot, which could in principle be present during a shot, would have been exaggerated during these low-energy tests. Wave-plate throttles were set so that 400 μJ of the 100-mJ front end were focused in the target chamber. This provided enough energy per pulse for the FSD wavefront sensor after transmission through the diagnostic mirror (0.5%) and yet was not too high for the FSM due to its internal attenuation (6.0 OD). Data acquisition by the FSD and FSM was synchronized so that each measurement represented the same OPCPA pulse.

Figure 115.24 shows an example of data measured by the FSD wavefront sensor. The raw 2-K × 2-K image contains Shack–Hartmann spots formed by the 133 × 133-lenslet array, from which is calculated both the wavefront and fluence at the input to the wavefront sensor. The image plane for this sensor is the last of the four tiled-grating assemblies inside

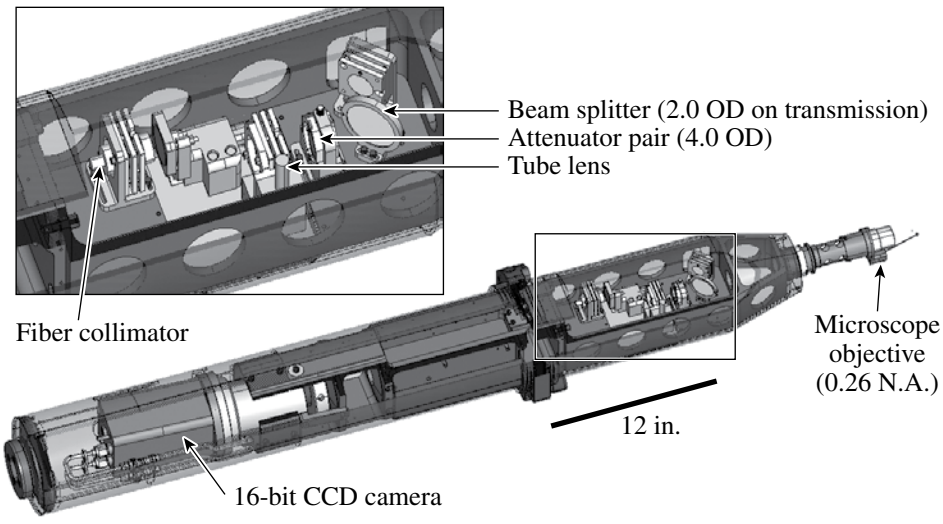

Figure 115.23
Focal-spot microscope (FSM) used for direct, low-energy measurements of the OMEGA EP focal spot in the OMEGA target chamber.

the compressor. The gaps between grating tiles are apodized within the main beamline to minimize diffraction effects that would otherwise result from each tile edge. As a result, the OPCPA beam is divided into three sub-beams, each of which is reduced separately. Separate measurements of the tiled-grating compressor were made to ensure the gratings were correctly aligned and tiled;[12] therefore it was assumed that there was no significant residual angular dispersion or differential piston error between the tiles.

Figure 115.25 shows a direct comparison of a focal spot measured indirectly by the FSD and directly by the FSM,

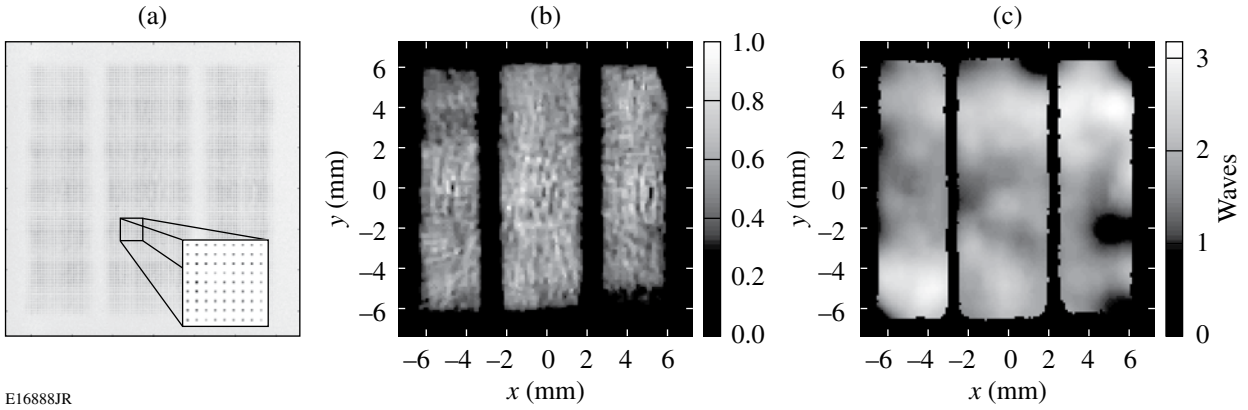

Figure 115.24
FSD measurements using the OPCPA front end. (a) Raw Shack–Hartmann image with inset showing the spots formed by each lenslet, (b) fluence (normalized), (c) wavefront (in units of waves).

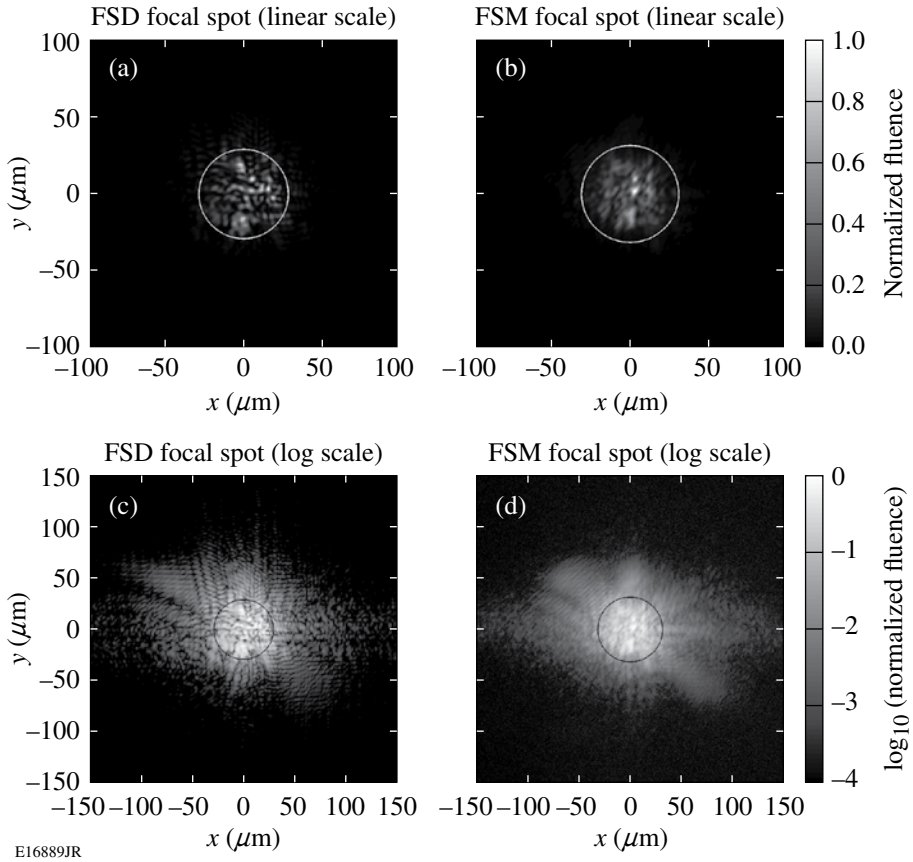

Figure 115.25
Same-shot measurements of focal spot by the FSD and FSM. (a),(b) Linear scale plots; (c),(d) logarithmic scale plots. Circles contain 80% of the energy.

on both linear and logarithmic scales. The FSD results were calculated using the transfer wavefront shown in Fig. 115.22(c) and the OPCPA measurements in Fig. 115.24. Agreement is reasonable, on both linear and logarithmic scales. The only fitting parameter used when calculating the FSD image was 25 μm of defocus between the PAD position used when measuring ΔW_{trans} and the FSM focal plane. This is reasonable given the precision of setting the axial position of one TIM-based diagnostic relative to another. The encircled energy curves calculated for both measurements are in good agreement up to the 70% encircled energy radius (see Fig. 115.26). Beyond this, FSD encircled energy values are larger than those measured by the FSM for the same radius by up to 4%. This trend has been seen consistently in a number of our experiments, both on OMEGA EP and smaller-scale test beds using continuous-wave sources.[19] Possible explanations include optical scattering from the FSM optics and within the CCD chip that could scatter light from the main spot, thereby reducing the inferred measurement of encircled energy at a given radius. Alternatively, the finite spatial resolution of the FSD wavefront sensor (133 × 133 lenslets) will not capture high spatial frequencies present in the wavefront to some degree, and these frequencies may contribute significantly to scattering to regions far from the main spot.

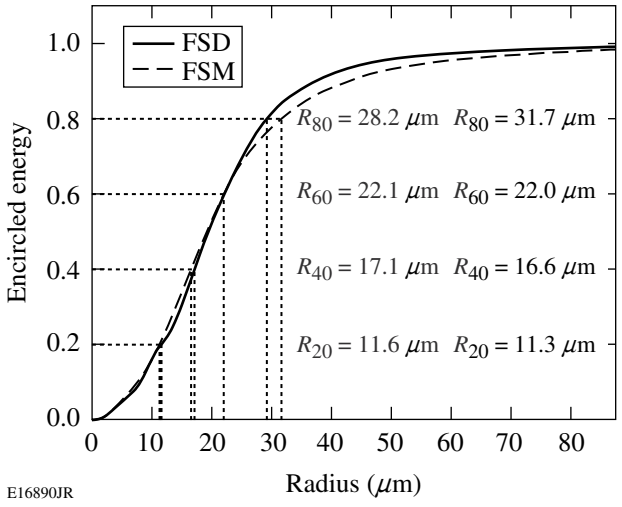

Figure 115.26
Encircled energy curves derived from Fig. 115.25.

To further test the validity of FSD measurements, we used a deformable mirror to severely distort the focal spot. The FSD and FSM measurements for distorted focal spots are shown in Figs. 115.27 and 115.28. Again, agreement is reasonably good, even down to four orders of magnitude below the maximum fluence.

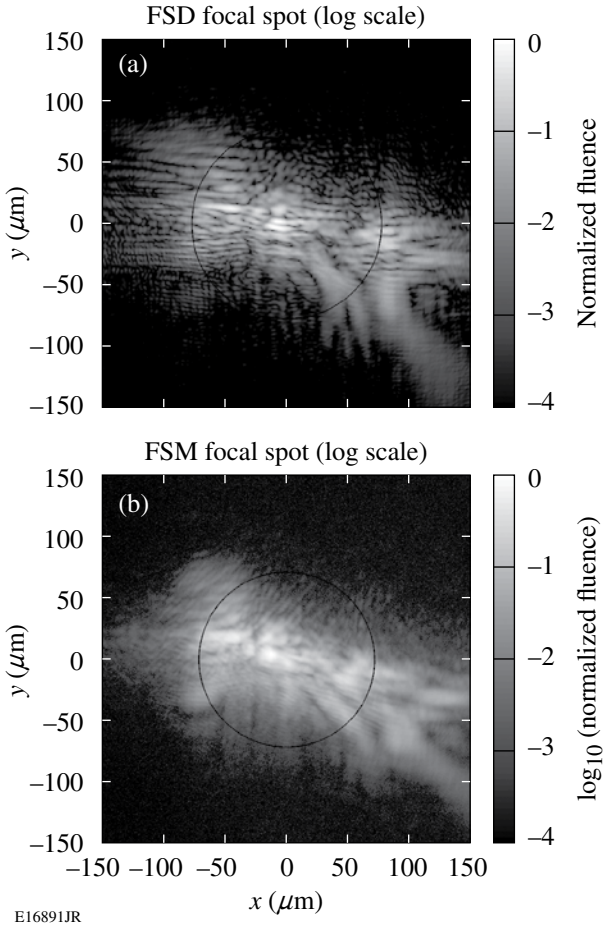

Figure 115.27
Comparison of FSD and FSM measurements for strongly aberrated focal spots (logarithmic scale). Circles contain 80% of the energy.

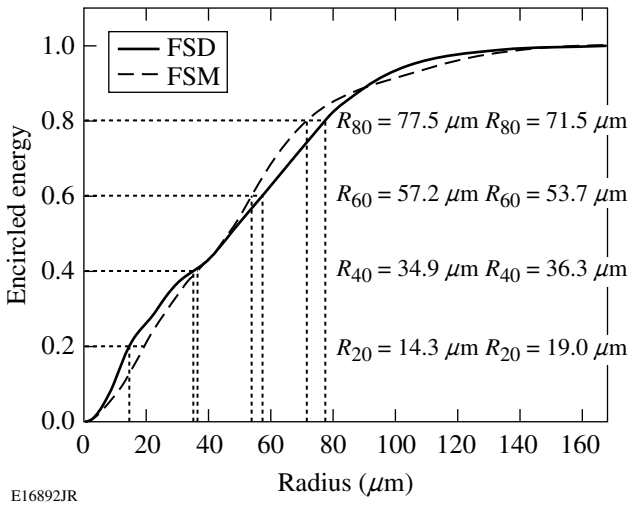

Figure 115.28
Encircled energy curves for the strongly aberrated focal spots shown in Fig. 115.27.

FSD Results for High-Energy Shots

A series of high-energy OMEGA EP target shots were taken in April 2008 to qualify the new laser system. Included in this qualification was an on-shot measurement by the FSD of the focal spot at the target. The following figures show results for one of the target shots (#3053), which was a 10-ps, 440-J shot to a planar target in the OMEGA target chamber.

Figure 115.29 shows the FSD measurement of the calibrated fluence and wavefront (i.e., after ΔW_{trans} was added). The diagnostic showed that there were ~3.3 waves of astigmatism and defocus due in part to thermally induced aberrations within the amplifiers. This type of on-shot information makes it possible to further improve the system, for example, by adjusting OAP alignment or optimizing the beamline adaptive optics system. The corresponding focal spot is shown in Fig. 115.30, in the form of a transverse scan through the focal volume along the axial direction of the beam, obtained by numerically propagating the field to each plane. The flexibility of this approach makes it possible to calculate the focal spot at an arbitrary plane. For example, the target for this shot was a Au-coated plastic ($500 \times 500 \times 10\ \mu\text{m}^3$) set at 45° to the beam, so the

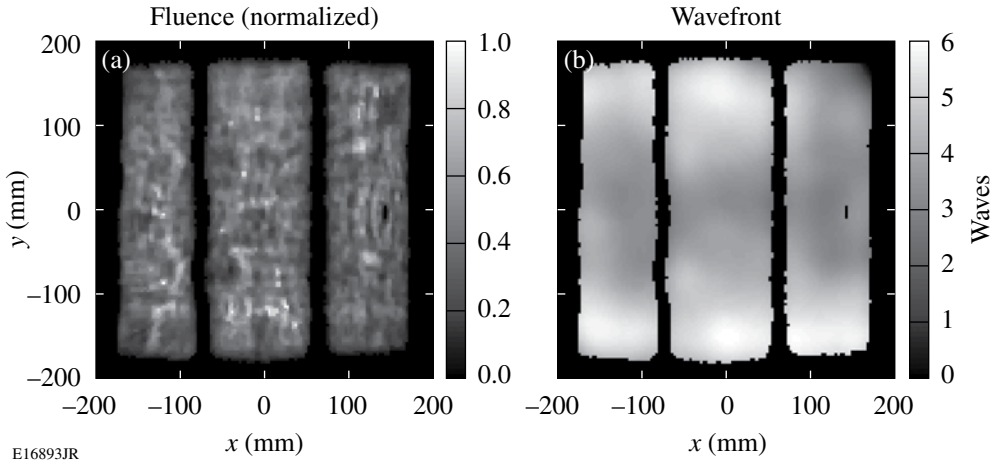

Figure 115.29
(a) On-shot fluence (normalized) and (b) wavefront (in units of waves), calibrated by adding ΔW_{trans}.

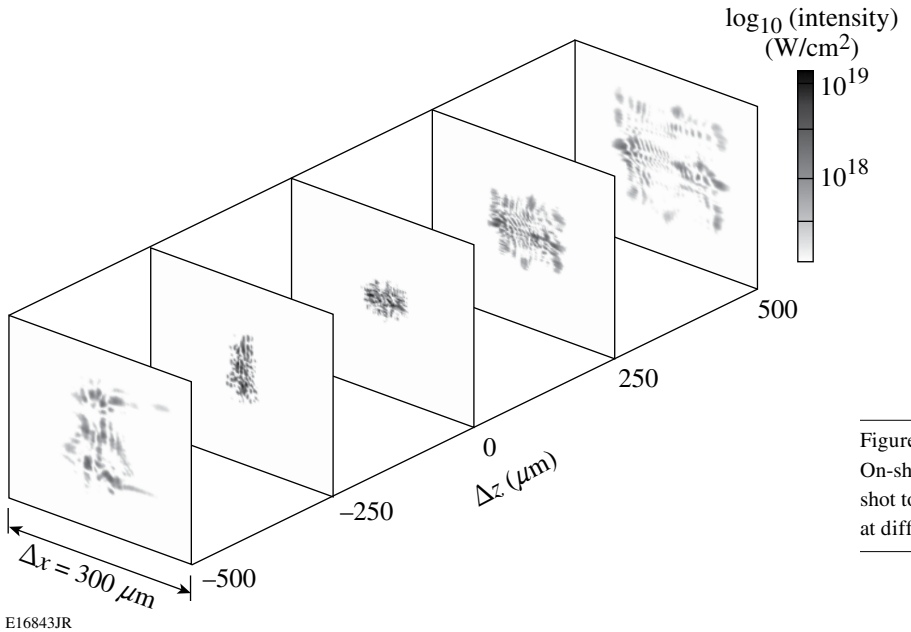

Figure 115.30
On-shot focal volume for a 10-ps, 440-J OMEGA EP target shot to the OMEGA chamber. Images show the focal spot at different planes, plotted on a logarithmic scale.

focal spot on the target surface can be obtained despite the oblique angle of incidence. Figure 115.31 shows the focal spot on a logarithmic scale along with the corresponding encircled energy curve.

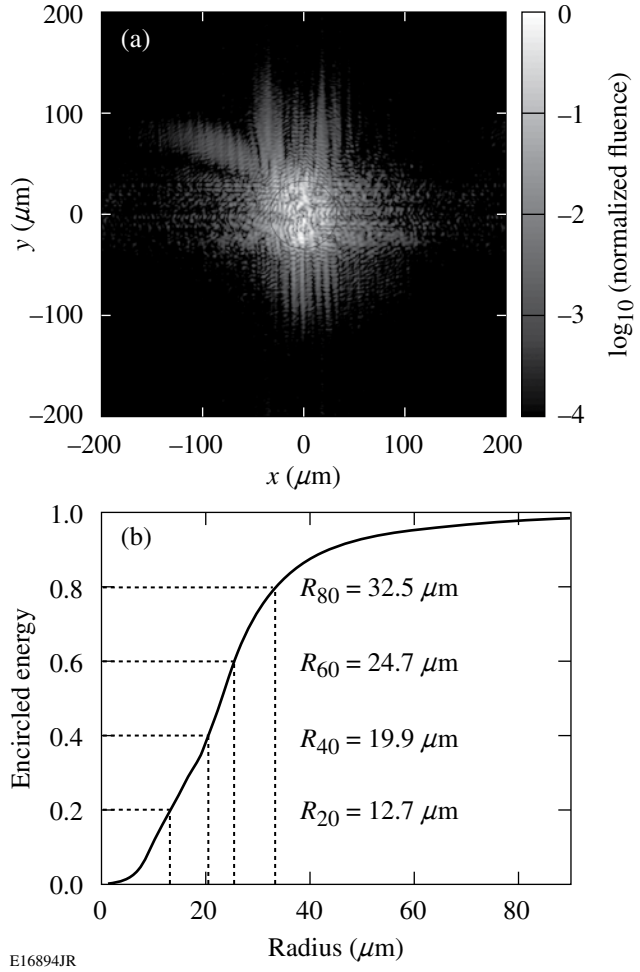

Figure 115.31
(a) Focal spot normalized fluence (logarithmic scale) and (b) encircled energy for a 10-ps, 440-J target shot.

Conclusions

A new focal-spot diagnostic suitable for characterizing high-energy petawatt-class lasers at full energy has been presented. The diagnostic was developed and demonstrated at LLE and is currently deployed as a facility laser diagnostic on the OMEGA EP Laser System. Accurate measurements at full energy are made using high-resolution wavefront sensing in combination with techniques to calibrate on-shot measurements made on a low-energy sample beam. The diagnostic was validated at low energy using a custom focal-spot microscope to directly measure the focus in the target chamber. Measurements at full energy are also shown for 10-ps, 450-J target shots taken as part of the campaign to activate OMEGA EP to the OMEGA target chamber.

ACKNOWLEDGMENT

This work was supported by the U.S. Department of Energy Office of Inertial Confinement Fusion under Cooperative Agreement No. DE-FC52-08NA28302, the University of Rochester, and the New York State Energy Research and Development Authority. The support of DOE does not constitute an endorsement by DOE of the views expressed in this article.

REFERENCES

1. L. J. Waxer, M. J. Guardalben, J. H. Kelly, B. E. Kruschwitz, J. Qiao, I. A. Begishev, J. Bromage, C. Dorrer, J. L. Edwards, L. Folnsbee, S. D. Jacobs, R. Jungquist, T. J. Kessler, R. W. Kidder, S. J. Loucks, J. R. Marciante, D. N. Maywar, R. L. McCrory, D. D. Meyerhofer, S. F. B. Morse, A. V. Okishev, J. B. Oliver, G. Pien, J. Puth, and A. L. Rigatti, presented at CLEO/QELS 2008, San Jose, CA, 4–9 May 2008 (Paper JThB1).

2. L. J. Waxer, D. N. Maywar, J. H. Kelly, T. J. Kessler, B. E. Kruschwitz, S. J. Loucks, R. L. McCrory, D. D. Meyerhofer, S. F. B. Morse, C. Stoeckl, and J. D. Zuegel, Opt. Photonics News **16**, 30 (2005).

3. C. P. J. Barty *et al*., Nucl. Fusion **44**, S266 (2004).

4. N. Blanchot *et al*., in *Topical Problems of Nonlinear Wave Physics*, edited by A. M. Sergeev (SPIE, Bellingham, WA, 2006), Vol. 5975, p. 59750C.

5. C. Le Blanc *et al*., in *Inertial Fusion Sciences and Applications 2003*, edited by B. A. Hammel, D. D. Meyerhofer, J. Meyer-ter-Vehn, and H. Azechi (American Nuclear Society, La Grange Park, IL, 2004), pp. 608–611.

6. C. N. Danson *et al*., Nucl. Fusion **44**, S2396 (2004).

7. K. Mima *et al*., Fusion Sci. Technol. **47**, 662 (2005).

8. V. Yanovsky *et al*., Opt. Express **16**, 2109 (2008).

9. M. Martinez *et al*., in *Laser-Induced Damage in Optical Materials: 2005*, edited by G. J. Exarhos *et al*. (SPIE, Bellingham, WA, 2006), Vol. 5991, p. 59911N.

10. R. A. Zacharias *et al*., Opt. Eng. **43**, 2873 (2004).

11. T. J. Kessler, J. Bunkenburg, H. Huang, A. Kozlov, and D. D. Meyerhofer, Opt. Lett. **29**, 635 (2004).

12. J. Qiao, A. Kalb, M. J. Guardalben, G. King, D. Canning, and J. H. Kelly, Opt. Express **15**, 9562 (2007).

13. S.-W. Bahk, P. Rousseau, T. A. Planchon, V. Chvykov, G. Kalintchenko, A. Maksimchuk, G. A. Mourou, and V. Yanovksy, Opt. Lett. **29**, 2837 (2004).

14. J. W. Goodman, *Introduction to Fourier Optics* (McGraw-Hill, New York, 1968).

15. L. J. Waxer, V. Bagnoud, I. A. Begishev, M. J. Guardalben, J. Puth, and J. D. Zuegel, Opt. Lett. **28**, 1245 (2003).

16. B. C. Platt and R. Shack, J. Refractive Surg. **17**, S573 (2001).

17. Imagine Optic, 91400 Orsay, France.

18. S.-W. Bahk, P. Rousseau, T. A. Planchon, V. Chvykov, G. Kalintchenko, A. Maksimchuk, G. Mourou, and V. Yanovsky, Appl. Phys. B **80**, 823 (2005).

19. T. J. Kessler, H. Huang, and D. Weiner, in *International Conference on Ultrahigh Intensity Laser Development, Science and Emerging Applications 2006* (ICUIL, Cassis, France, 2006), pp. 126–128.

20. S.-W. Bahk, J. Bromage, J. D. Zuegel, and J. R. Fienup, presented at CLEO/QELS 2008, San Jose, CA, 4–9 May 2008 (Paper JThB6).

Suprathermal Electrons Generated by the Two-Plasmon-Decay Instability in Gas-Filled Hohlraums

Inertial confinement fusion (ICF) occurs when a spherical shell target containing thermonuclear fuel (i.e., deuterium and tritium) is imploded to produce energy gain.[1,2] Energy gain is predicted to be achieved with megajoule (MJ)-class lasers, such as the 192-beam, 351-nm, 1.8-MJ National Ignition Facility (NIF) being constructed at the Lawrence Livermore National Laboratory.[3] The implosion is driven by the ablation of material from the outer shell surface with intense laser beams (direct drive)[1] or with x rays produced in a high-Z enclosure or hohlraum (indirect drive).[2] Ignition will be first explored on the NIF with indirect-drive ICF. The NIF laser beams are arranged in two cones around the poles of the spherical target chamber to irradiate both sides of the cylindrical hohlraum through the laser entrance holes (LEH's). The laser beams irradiate the inner high-Z wall (i.e., Au, U) of the hohlraum, and the resulting high-Z plasma radiates x rays that are trapped and re-radiated by the opaque hohlraum wall and uniformly ablate the implosion capsule.[2,4] Ignition requires high-compression implosions (convergence ratio ~30), which places strict requirements on the irradiation-nonuniformity level of the x-ray drive on the capsule (<1% to 2% rms) and on the compressibility of the DT fuel. The required drive symmetry is more likely to be achieved if the hohlraum is filled with a low-Z gas fill, which minimizes the motion of the laser-deposition region.[2] A thin (0.5-μm) polyimide window covering each LEH is required to initially contain the gas fill. High compressibility requires that the DT fuel remain close to Fermi degenerate throughout the implosion. This requires control of irreversible heating of the DT fuel, leading to precise pulse shaping to minimize shock heating of the fuel.[2,5] Any additional irreversible heating sources such as suprathermal or hot electrons ($T_{\text{hot}} > 20$ keV) produced by laser–plasma interactions need to be understood and controlled. This article reports, for the first time, evidence of hot-electron production during the early-time burnthrough of the LEH window, which, if not properly controlled, could lead to unacceptably large hot-electron preheat of the DT fuel in an ignition capsule.

The experimental signature of suprathermal-electron generation is the hard x-ray bremsstrahlung emission from small angle scattering of the hot electrons in the high-Z wall of the hohlraum target.[6] The possible sources of hot-electron generation are parametric processes that produce electron-plasma waves, such as two-plasmon-decay ($2\omega_{\text{pe}}$) instability[7,8] and stimulated Raman scattering (SRS).[8,9] The $2\omega_{\text{pe}}$ instability occurs near quarter-critical density when the phase-matching conditions are satisfied for the laser light to decay into two electron-plasma waves or plasmons. SRS involves the decay of a laser photon into a plasmon and a scattered photon in the visible spectrum. Wave–particle interactions (e.g., Landau damping, trapping, and wave breaking) can generate hot electrons.[8] In addition to hard x rays, an experimental signature of $2\omega_{\text{pe}}$ instability is significant $3/2\omega$ emission, which is Thomson scattering of the laser drive from the plasmons.

This article shows, for the first time, that gas-filled hohlraums driven with 13.5 kJ of 351-nm laser light produce two bursts of suprathermal electrons that are clearly resolved with the shaped laser pulse drive having a lower-intensity foot pulse followed by a higher-intensity main drive. The first burst from the two-plasmon-decay ($2\omega_{\text{pe}}$) instability in the exploding LEH window produces up to 20 J of hot electrons with $T_{\text{hot}} \sim 75$ keV. It has a sharp laser-intensity threshold when the overlapped beam intensity is around 0.5×10^{15} W/cm^2. The $2\omega_{\text{pe}}$ instability has been observed in direct-drive ICF;[10] however, this is the first observation of the $2\omega_{\text{pe}}$ instability for indirect-drive ICF using 351-nm laser light. The second pulse with $T_{\text{hot}} \sim 20$ keV coincides with the SRS during the main laser drive. Previous hard x-ray experiments were not sensitive to the production of window hot electrons because they were time integrated.[6] Window hot electrons were also not observed using an x-ray spectroscopic technique.[11] Only a single burst of hard x rays is observed from a vacuum hohlraum because it does not have a gas fill contained by an LEH window.

Gas-filled Au hohlraums were irradiated on the OMEGA Laser System[12] with 40 beams arranged in three cones and smoothed with phase plates.[13] The thickness of the Au hohlraum wall ranged from 2 to 5 μm, and the hohlraum length varied from 2.3 to 2.55 mm. The inside diameter was 1.6 mm and

the LEH diameter varied from 1.07 to 1.2 mm. Figure 115.32 shows a computer rendering of the hohlraum and the energy-deposition regions of the cone 1, cone 2, and cone 3 beams having angles of incidence to the hohlraum axis of 21.4°, 42.0°, and 58.8°, respectively. Best focus of all the beams occurred at the LEH. Cone 2 and cone 3 beams were pointed to the center of the LEH and contributed to the peak overlapped laser intensity. Cone 1 beams were pointed slightly outside the center of the LEH and did not overlap the other beams at the LEH. All of the hohlraums, except for the vacuum ones, had a 0.6-μm-thick polyimide window, which is close to the 0.5-μm LEH window thickness of the NIF target. As shown in Table 115.I, the initial fully ionized electron density n_e of the hohlraum gas fill was varied by changing the gas fill, where the critical density is given as $n_{cr} = 1.1 \times 10^{21}/\lambda_{\mu m}^2 \text{cm}^{-3} = 9.0 \times 10^{21}\,\text{cm}^{-3}$. The measured laser power of the shaped laser pulse drive (PS26) is shown in Fig. 115.33. The total on-target laser energy E_{UV} was 13.5 kJ. The peak foot power was adjusted to vary the overlapped laser intensity at the LEH window from 0.5 to 1.5 $\times$ 10^{15} W/cm^2. The laser burned through the LEH window with the lower-intensity foot and produced peak radiation temperatures of ~190 eV during the higher-intensity main drive.

The hard x-ray diagnostic (HXRD) has four high-pass energy channels recording time-resolved measurements along a line of sight 42° to the hohlraum axis.[14] The channels have the following lower-energy cutoffs: $h\nu > 20$ keV (HXRD1), $h\nu > 40$ keV (HXRD2), $h\nu > 60$ keV (HXRD3), and $h\nu > 80$ keV (HXRD4). The HXRD has a 120-ps rise time and a 1/e decay time of 1.2 ns. The absolute time scale was established using the hard x rays emitted from a Au spherical target irradiated with an ~200-ps

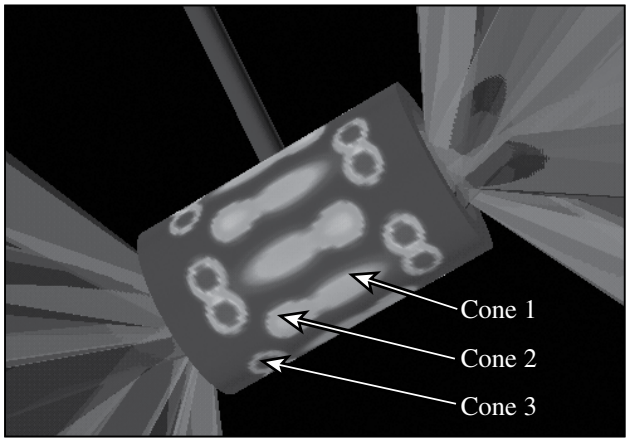

E16297JR

Figure 115.32
Computer rendering of a gas-filled Au hohlraum irradiated with 40 laser beams. The beams are arranged in three cones and have elliptical phase plates. The energy-deposition regions of cone 1, cone 2, and cone 3 beams are shown on the inner wall of the hohlraum. A shaped laser pulse delivers 13.5 kJ of 351-nm light.

Table 115.I: Hohlraum specifications.

Gas Fill	Pressure (atm)	Initial Fully Ionized n_e
100% CH_4	0.9	0.02 n_{cr}
76% CH_4 + 24% C_5H_{12}	0.9	0.04 n_{cr}
100% C_5H_{12}	0.9	0.1 n_{cr}

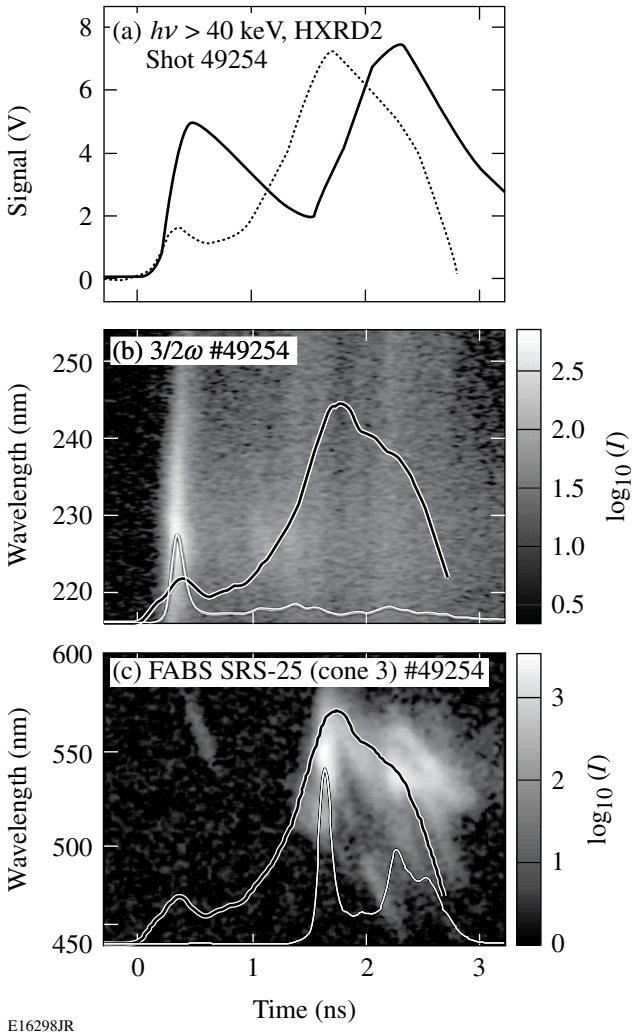

E16298JR

Figure 115.33
(a) Time history of HXRD2 ($h\nu > 40$ keV) (solid curve) compared with laser power (dotted curve). (b) Time-resolved spectral measurement of 3/2ω emission compared with measured laser pulse (white/black curve). Spectrally integrated time history is superposed (white curve). (c) Time-resolved FABS SRS with spectrally integrated time history (white curve) and laser power (white/black curve) superposed.

Gaussian laser pulse. The fraction f_{hot} of laser energy E_{UV} coupled to hot electrons (i.e., $E_{hot} = f_{hot} E_{UV}$) and the temperature characterizing the Maxwellian distribution of hot electrons T_{hot} were inferred from the HXRD measurements using the thick-target bremsstrahlung radiation approximation

$$\frac{dI}{d\nu d\Omega} = \frac{5 \times 10^{11}}{4\pi} E_{hot} \frac{Z}{79} \exp\left(1 - \frac{h\nu}{T_{hot}}\right) \text{keV/keV/sr},$$

where Z is the atomic number of the hohlraum wall material.[6] The attenuation of the lower-energy hard x rays by the Au hohlraum wall was included in the analysis. An *in-situ* calibration was performed on the HXRD using the hard x-ray emission spectrum from a vacuum Au hohlraum irradiated with an 18-kJ, 1-ns square laser pulse. The calibration relied on earlier hohlraum hard x-ray measurements taken on the NOVA laser: the hard x-ray emission from a vacuum Au hohlraum was measured with the filter fluorescer experiment diagnostic,[6] and a Maxwellian distribution of hot electrons with T_{hot} = 30 keV and f_{hot} = 0.3% to 1.0% was inferred from the hard x-ray measurements.[15] The calibration of the HXRD on OMEGA used T_{hot} = 30 keV and f_{hot} = 1%; therefore, the estimates of E_{hot} reported in this article represent upper limits. The uncertainty in the absolute value of E_{hot} does not affect the scaling of hot-electron production with the overlapped laser intensity on the window nor the inferred values of T_{hot}. The $3/2\omega$ emission from the LEH was recorded with a 100-ps temporal resolution and a 0.5-nm spectral resolution.[16] The SRS scattered directly back into the OMEGA lens of a cone 3 beam was recorded with a full-aperture backscatter station (FABS).[16]

The time history of HXRD2 (solid curve) recorded on shot number 49254 for a gas-filled Au hohlraum is compared with the PS26 laser pulse (dotted curve) in Fig. 115.33(a). The peak overlapped foot intensity was $\sim 1.2 \times 10^{15}$ W/cm^2 and the initial fully ionized n_e of the gas fill was 0.1 n_{cr}. The first burst of hard x rays occurs around the time of peak laser foot power, while the second burst of hard x rays occurs around the time of peak laser power. The long decay times of the HXRD measurements are instrumental; nevertheless, the diagnostic has enough temporal resolution to resolve the two bursts of hard x-ray emission. The x-ray fluences of the first and second hard x-ray pulses were calculated for each of the four energy channels, and T_{hot} and f_{hot} were quantified using a least-squares-fitting routine. The time-resolved $3/2\omega$ spectrum is shown in Fig. 115.33(b) and the time-resolved FABS SRS in Fig. 115.33(c). Overplotted on the streaked spectra in Figs. 115.33(b) and 115.33(c) are the laser power and the spectrally integrated scattered-light signals. As can be seen in Fig. 115.33, the first x-ray pulse correlates with the $3/2\omega$ emission during the foot of the laser drive, and the second x-ray pulse correlates with the FABS SRS during the main drive.

The dependence of hot-electron production on the initial hohlraum n_e was investigated, with the peak overlapped foot intensity at the LEH around 1.2×10^{15} W/cm^2. As n_e was increased from 0.02 n_{cr} to 0.1 n_{cr}, f_{hot} for the first hard x-ray pulse increased from 0.005% to 0.1% and T_{hot} increased from 50 to 75 keV. As n_e was increased from 0 to 0.1 n_{cr}, f_{hot} for the second hard x-ray pulse increased from 0.1% to 5% and T_{hot} remained constant around 20 keV. The difference in T_{hot} for the first and second hard x-ray pulses is due to the higher phase velocity of the electron-plasma waves generated by the $2\omega_{pe}$ instability compared to those created by SRS.

The overlapped laser intensity on the LEH was varied from 0.5 to 1.5×10^{15} W/cm^2, and the intensity scaling of hot-electron generation in the exploding LEH window was investigated. The results are shown in Fig. 115.34(a) for E_{hot} with a very sharp threshold just above 0.5×10^{15} W/cm^2. The circles and triangles represent the lower ($n_e = 0.04\ n_{cr}$) and higher ($n_e = 0.1\ n_{cr}$) electron densities, respectively. The total energy in hot electrons, E_{hot}, is approximately 20 J with the higher n_e and an overlapped LEH laser intensity of $\sim 1.2 \times 10^{15}$ W/cm^2. The production of window hot electrons for the NIF-like density ($n_e = 0.04\ n_{cr}$) with the high overlapped intensity is between 2 and 5 J. The scaling of T_{hot} with the overlapped LEH intensity is shown in Fig. 115.34(b). The hohlraums with $n_e = 0.1\ n_{cr}$ and the highest overlapped intensity have $T_{hot} \sim 75$ keV. More scatter in T_{hot} (40 keV < T_{hot} < 80 keV) is observed for the hohlraums with $n_e = 0.04\ n_{cr}$ and the highest overlapped intensity. The measurements with the lowest overlapped intensity show a decrease in T_{hot} to ~30 keV. The OMEGA experiment is an excellent surrogate for the production of window hot electrons on the NIF ignition hohlraum: 2-D simulations from the radiation hydrodynamics code *HYDRA*[17] show that the window burnthrough phase of the gas-filled OMEGA hohlraum is hydrodynamically similar to that of an ignition hohlraum.

The linear theory of Simon *et al.* for the $2\omega_{pe}$ instability[7] predicts the threshold and growth rate of the instability, as well as the hot-electron temperature T_{hot} of electrons trapped in the plasmons; however, it does not predict the total energy in the trapped electrons. This requires determining the amplitude of the plasma waves, the trapping rate of electrons in the waves, and the competition between trapping and other wave saturation mechanisms, such as collisions. For the simulated

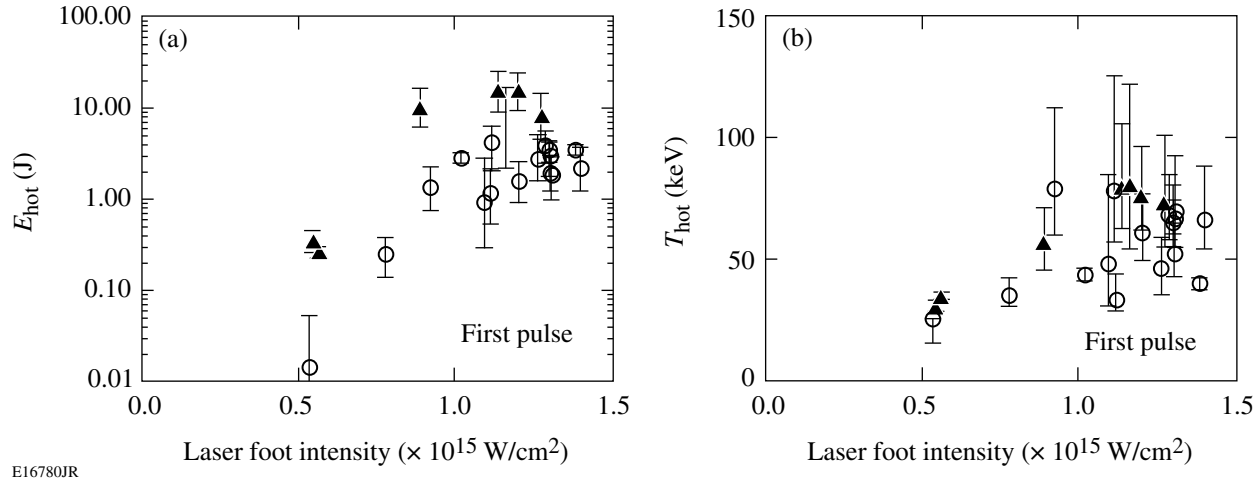

Figure 115.34
Scaling of (a) E_{hot} and (b) T_{hot} with the peak overlapped laser intensity on the LEH window for $n_e = 0.04\ n_{cr}$ (circles) and $n_e = 0.1\ n_{cr}$ (triangles).

electron temperatures in the exploding window of an OMEGA hohlraum, the linear theory of the $2\omega_{pe}$ instability predicts $T_{hot} \geq 70$ keV, which is consistent with measurements during the early part of the laser pulse.

The $2\omega_{pe}$ instability occurs only in the vicinity of plasma at $n_e = 0.25\ n_{cr}$. The threshold intensity for the $2\omega_{pe}$ instability, $I_{thresh} \propto T_e / \lambda L$, is a function of the laser wavelength λ, electron temperature T_e, and density gradient scale length in the direction of the laser beam, $L = n_e\left(\partial n_e / \partial x\right)^{-1} = \left(n_{cr}/4\right)\left(\partial n_e / \partial x\right)^{-1}$. Motivated by recent direct-drive experiments,[10] the overlapped beam intensity is used in the threshold formula rather than the intensity of a single beam. This lower threshold is likely due to cooperative excitation of a common forward-directed plasma wave and/or to effects, such as swelling in intensity and increased interaction length for incident light waves that turn near the quarter-critical density.

Using 2-D radiation hydrodynamic simulations from the code *HYDRA*, it is possible to determine the laser power P_{pass} that passes the $n_e = 0.25\ n_{cr}$ surface with intensity above the threshold. The energy at risk of scattering into two plasmons is then given by

$$E_{risk} = \int_t \max\left(0, P_{pass} - P_{thresh}\right) dt$$
$$= \int_t dt \sum_N P_{ray} \max\left(0, \frac{I_{pass} - I_{thresh}}{I_{thresh}}\right).$$

Here, P_{pass}–P_{thresh} is the laser power with intensity $I > I_{thresh}$ and P_{ray} is the power of each of the N computed laser rays as it crosses the $n_e = 0.25\ n_{cr}$ surface. In *HYDRA*, the average intensity, defined as the amount of power traversing a zone, is used to represent the overlap intensity I. This expression does not predict E_{hot} since it does not include the efficiency at which the $2\omega_{pe}$ instability generates hot electrons; however, the threshold given above can qualitatively explain the observed scalings of E_{hot} with hohlraum gas-fill density and laser intensity.

The two factors that determine the energy at risk for the $2\omega_{pe}$ instability are the fraction of the laser flux that crosses a surface of density $n_e = 0.25\ n_{cr}$ and the intensity of the laser at that surface. When the laser beams initially ablate the 0.6-μm-thick polyimide LEH window, they launch a shock wave. As the window plasma expands to low density, the laser-energy–deposition rate drops. The shock wave becomes unsupported and transits into the gas plasma behind the window as a hemispherical blast wave. When the blast wave expands below $n_e = 0.25\ n_{cr}$ everywhere, the risk of the $2\omega_{pe}$ instability in the LEH region is gone.

For hohlraums with an initial gas plasma density of $n_e = 0.04\ n_{cr}$, *HYDRA* simulations show that the blast-wave density is below $n_e = 0.25\ n_{cr}$ as soon as it enters the gas region. For the $n_e = 0.10\ n_{cr}$ hohlraums, the blast-wave peak density remains above $n_e = 0.25\ n_{cr}$ for about 0.1 ns after the blast wave enters the gas plasma. *HYDRA* simulations predict that E_{risk} should drop by a third between $n_e = 0.10\ n_{cr}$ and $n_e = 0.04\ n_{cr}$, which is consistent with the upper range of the points in Fig. 115.34(a). Post-processed *HYDRA* simulations confirm that E_{risk} decreases with intensity; however, this predicted scaling is too slow to explain the rapid drop in E_{hot} observed for intensities below 10^{15} W/cm^2. Presumably, the observed

drop is due to a decrease in the efficiency of trapping and accelerating electrons in the plasmons, which is not modeled in the expression for E_{risk}.

The observed threshold for the window hot electrons can be exploited to mitigate the hot-electron production as the LEH window burns through in gas-filled hohlraums. Specifications for the NIF ignition target restrict E_{hot} to less than 8 J for T_{hot} = 70 keV and to less than 38 J for T_{hot} = 30 keV; otherwise, preheat of the implosion capsule could jeopardize hot-spot ignition. As a result of this research, the initial overlapped laser intensity incident on the LEH window of an ignition target for the NIF has been set below the measured intensity threshold to retain ignition margin by staggering the turn-on time of the inner and outer cones of beams.

Two bursts of suprathermal electrons are observed from gas-filled hohlraums driven with 351-nm laser light. The $2\omega_{\text{pe}}$ instability in the exploding LEH window appears to produce up to 20 J of hot electrons with $T_{\text{hot}} \sim 75$ keV at early times and has a sharp laser-intensity threshold around 0.5×10^{15} W/cm^2. The observed threshold can be exploited to mitigate the hot-electron production in hohlraums. Simulations using a 2-D radiation hydrodynamics code and a linear theory of the $2\omega_{\text{pe}}$ instability show qualitative agreement with the experimental results. The second pulse produced by SRS during the main laser drive has more energy, but significantly lower $T_{\text{hot}} \sim 20$ keV.

ACKNOWLEDGMENT

The authors acknowledge the superb operation of the OMEGA Laser System, the target fabrication expertise of M. Bonino at LLE and A. Nikroo at General Atomics, and the diagnostic expertise of R. Bahr and S. Roberts at LLE. This work was supported by the U.S. Department of Energy Office of Inertial Confinement Fusion under Cooperative Agreement No. DE-FC52-08NA28302, the University of Rochester, and the New York State Energy Research and Development Authority. The support of DOE does not constitute and endorsement by DOE of the views expressed in this article.

REFERENCES

1. R. L. McCrory, D. D. Meyerhofer, R. Betti, R. S. Craxton, J. A. Delettrez, D. H. Edgell, V. Yu Glebov, V. N. Goncharov, D. R. Harding, D. W. Jacobs-Perkins, J. P. Knauer, F. J. Marshall, P. W. McKenty, P. B. Radha, S. P. Regan, T. C. Sangster, W. Seka, R. W. Short, S. Skupsky, V. A. Smalyuk, J. M. Soures, C. Stoeckl, B. Yaakobi, D. Shvarts, J. A. Frenje, C. K. Li, R. D. Petrasso, and F. H. Séguin, Phys. Plasmas **15**, 055503 (2008).

2. J. D. Lindl *et al*., Phys. Plasmas **11**, 339 (2004).

3. J. A. Paisner, E. M. Campbell, and W. J. Hogan, Fusion Technol. **26**, 755 (1994); G. H. Miller, E. I. Moses, and C. R. Wuest, Opt. Eng. **43**, 2841 (2004).

4. J. Schein *et al*., Phys. Rev. Lett. **98**, 175003 (2007); O. S. Jones *et al*., Phys. Plasmas **14**, 056311 (2007).

5. M. C. Herrmann, M. Tabak, and J. D. Lindl, Nucl. Fusion **41**, 99 (2001); R. Betti, K. Anderson, V. N. Goncharov, R. L. McCrory, D. D. Meyerhofer, S. Skupsky, and R. P. J. Town, Phys. Plasmas **9**, 2277 (2002).

6. R. P. Drake *et al*., Phys. Rev. A **40**, 3219 (1989); J. W. McDonald *et al*., Rev. Sci. Instrum. **75**, 3753 (2004); J. W. McDonald *et al*., Phys. Plasmas **13**, 032703 (2006).

7. D. W. Phillion *et al*., Phys. Rev. Lett. **49**, 1405 (1982); D. M. Villeneuve, R. L. Keck, B. B. Afeyan, W. Seka, and E. A. Williams, Phys. Fluids **27**, 721 (1984); C. Rousseaux *et al*., Phys. Fluids B **4**, 2589 (1992); W. Seka, R. E. Bahr, R. W. Short, A. Simon, R. S. Craxton, D. S. Montgomery, and A. E. Rubenchik, Phys. Fluids B **4**, 2232 (1992); C. S. Liu and M. N. Rosenbluth, Phys. Fluids **19**, 967 (1976); A. Simon, R. W. Short, E. A. Williams, and T. Dewandre, Phys. Fluids **26**, 3107 (1983); A. B. Langdon, B. F. Lasinski, and W. L. Kruer, Phys. Rev. Lett. **43**, 133 (1979); B. F. Lasinski and A. B. Langdon, Lawrence Livermore National Laboratory, Livermore, CA, Report UCRL-50021-77, 4-49 (1978); B. B. Afeyan and E. A. Williams, Phys. Plasmas **4**, 3827 (1997); B. B. Afeyan and E. A. Williams, Phys. Plasmas **4**, 3845 (1997).

8. W. L. Kruer, *The Physics of Laser–Plasma Interactions,* Frontiers in Physics, Vol. 73, edited by D. Pines (Addison-Wesley, Redwood City, CA, 1988), Chap. 4, pp. 37–43.

9. J. W. Shearer *et al*., Phys. Rev. A **6**, 764 (1972); K. Estabrook, W. L. Kruer, and B. F. Lasinski, Phys. Rev. Lett. **45**, 1399 (1980); K. Estabrook and W. L. Kruer, Phys. Fluids **26**, 1892 (1983); A. A. Offenberger *et al*., Phys. Rev. Lett. **49**, 371 (1982); T. P. Hughes, *Plasmas and Laser Light* (Wiley, New York, 1975); B. J. MacGowan *et al*., Phys. Plasmas **3**, 2029 (1996).

10. C. Stoeckl, R. E. Bahr, B. Yaakobi, W. Seka, S. P. Regan, R. S. Craxton, J. A. Delettrez, R. W. Short, J. Myatt, A. V. Maximov, and H. Baldis, Phys. Rev. Lett. **90**, 235002 (2003).

11. S. H. Glenzer *et al*., Phys. Rev. Lett. **81**, 365 (1998).

12. T. R. Boehly, D. L. Brown, R. S. Craxton, R. L. Keck, J. P. Knauer, J. H. Kelly, T. J. Kessler, S. A. Kumpan, S. J. Loucks, S. A. Letzring, F. J. Marshall, R. L. McCrory, S. F. B. Morse, W. Seka, J. M. Soures, and C. P. Verdon, Opt. Commun. **133**, 495 (1997).

13. *LLE Review Quarterly Report* **112**, 212, Laboratory for Laser Energetics, University of Rochester, Rochester, NY, LLE Document No. DOE/SF/19460-790 (2007).

14. C. Stoeckl, V. Yu. Glebov, D. D. Meyerhofer, W. Seka, B. Yaakobi, R. P. J. Town, and J. D. Zuegel, Rev. Sci. Instrum. **72**, 1197 (2001).

15. R. L. Kauffman, Lawrence Livermore National Laboratory, private communication (2008).

16. W. Seka, D. H. Edgell, J. P. Knauer, J. F. Myatt, A. V. Maximov, R. W. Short, T. C. Sangster, C. Stoeckl, R. E. Bahr, R. S. Craxton, J. A. Delettrez, V. N. Goncharov, I. V. Igumenshchev, and D. Shvarts, Phys. Plasmas **15**, 056312 (2008).

17. M. M. Marinak *et al*., Phys. Plasmas **8**, 2275 (2001).

Effectiveness of Silicon (Si) as a Laser Shinethrough Barrier for 351-nm Light

Introduction

In direct-drive inertial confinement fusion (ICF), energy from many individual high-power laser beams is delivered to a spherical target, causing a spherically symmetric implosion.[1] Current ignition designs for direct-drive targets require a layer of condensed D_2 or DT fuel that adheres to the inner surface of a spherical plastic-shell ablator. The laser ionizes the target shell's surface, forming a plasma that surrounds the target. This coronal plasma governs any further interaction of the laser and the target, and the critical surface within the plasma prevents further direct transmission of light into the target's interior. The laser energy is absorbed in the subcritical underdense plasma and transported by the electrons through the overdense plasma to the ablation front. The ablation pressure drives the fuel layer inward, compressing both it and the gaseous fuel at the target's center. The drive pressure is varied in time such that the fuel density is compressed (up to ~1000× solid density for ignition designs) while remaining close to Fermi degenerate. Shock waves resulting from the drive-pressure history, along with compressive work, heat the central gaseous-core "hot spot" to the high temperatures needed to initiate burning of the fuel.

Asymmetry-induced hydrodynamics can reduce the performance of ICF targets to well below that predicted by 1-D modeling.[2] The hydrodynamic instability of most concern is Rayleigh–Taylor instability (RTI).[3,4] Imperfections in the spherical symmetry of both the target structure and the laser illumination act as seeds for the RTI. The nonlinear growth of this instability on the inner surface of the target mixes the cold compressed fuel layer with the hot-spot fuel vapor and/or shell, reducing fusion yield or preventing ignition.[5–8] Ignition requirements impose severe constraints on the illumination uniformity and the sphericity of the target.[9]

It has long been known[10,11] that very early during laser irradiation, before the coronal plasma density reaches critical density, the target is transparent to the laser light and laser energy can penetrate into the target. Deposition of this laser "shinethrough" energy within the target can severely degrade target performance even though the total energy is small. Absorption of shinethrough laser light can transmit nonuniformities in the illumination due to power imbalance or imprint into the target's interior. These asymmetries are made worse by filamentation of the penetrating laser power inside the target, which has been observed to leave permanent damage tracks.[10] The nonuniform deposition of energy in the interior of the target can create density perturbations that seed the RTI.

Shinethrough-seeded RTI has been identified as the likely cause of anomalous results in "burnthrough" mass-ablation-rate experiments.[12,13] In these experiments, a high-Z tracer layer was embedded within a target as a diagnostic, and the onset time of characteristic x-ray radiation from that layer during an implosion was used to infer the burnthrough ablation rates. The measured ablation rates were far greater than predicted by 1-D modeling. The spatial distribution of the characteristic x rays was found to be emitted from many localized spots.[13] The addition of an opaque barrier layer on the target surface was shown to bring the characteristic x-ray onset time in line with the 1-D predictions.[12]

A thin barrier layer of UV opaque material on the outer surface of the target forces breakdown to occur at the outer surface, effectively eliminating the deleterious effects of shinethrough. The conventional material used for shinethrough barriers is aluminum (Al). Barrier layers of Al have been shown to block shinethrough light and improve implosion performance. A thin barrier layer of 200 Å of Al eliminated all signs of filamentation damage tracks in laser-illuminated targets.[10] Deuterium-filled glass targets with a 500-Å Al barrier imploded using the original 24-beam OMEGA Laser System[14] showed a clear yield improvement over uncoated targets.[11]

For direct-drive cryogenic targets on OMEGA, a suitable shinethrough barrier material must be opaque to the 351-nm UV laser light *and* be compatible with the standard cryogenic target fabrication techniques of permeation filling, infrared (IR) layering, and optical characterization. The common Al barrier material is unsuitable in this context in all respects. In

the past, silicon (Si) has been identified as a potential barrier material for cryogenic direct-drive targets.[15] Its transmission characteristics are sufficient for optical characterization at 627 nm (Fig. 115.35) and laser-assisted cryogenic layering at 3.16 μm, and it is suitable for permeation filling.

At the laser wavelength (351 nm) the Si barrier is almost opaque and its opacity increases with laser intensity due to the easy formation of free electrons in Si. Silicon thus appears to be an excellent candidate for a shinethrough barrier material.

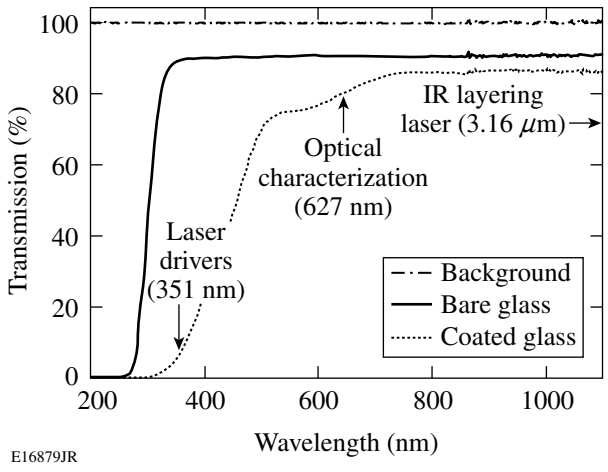

Figure 115.35
Transmission of light through uncoated glass and through glass coated with ~1100 Å of Si. The silicon-coating transmission is low at the UV laser driver wavelength (351 nm) and high at the ice-layer optical characterization wavelength (627 nm).

In this article we experimentally verify the suitability of Si as a shinethrough barrier material for 351-nm direct-drive laser-fusion experiments. The following sections (1) report the successful permeation filling, IR layering, and optical characterization of Si barrier–coated cryogenic targets; (2) experimentally verify the performance of Si as a shinethrough barrier; (3) determine a minimum acceptable barrier thickness; and (4) discuss our conclusions.

Cryogenic Target Fabrication with Si Barriers

Cryogenic targets for OMEGA are permeation filled with either D_2 or DT at room temperature at approximately 1000 atm in the Fill/Transfer Station (FTS).[16] The targets are deuterated polystyrene shells of 3- to 10-μm wall thickness suspended in a beryllium "C-mount" using four submicron threads of spider silk. Once filled, the targets are cooled slowly (~0.1 K/min) to below their fuel triple point, forming rough ice layers inside the targets.[16]

The rough ice layers are subsequently smoothed using volumetric heating just below the triple point, which leads to a sublimation/condensation redistribution of the ice mass toward an inner surface that is smoother, more uniform, and closer to an isotherm. Volumetric heating naturally occurs in DT and T_2 fuels that self-heat due to tritium beta decay.[17,18] For D_2 fuel, the infrared heating technique[19] deposits energy volumetrically in the ice by pumping an IR collisionally induced vibration–rotation band of deuterium. The wavelength of the IR heating laser employed at LLE is 3.16 μm.

LLE uses optical backlit shadowgraphy to characterize OMEGA cryogenic target ice layers.[20,21] A 627-nm, red-light–emitting diode (LED) provides the backlighting. A shadowgram records the image of the light rays passing through a backlit target. The rays are reflected and refracted at the shell wall and ice-layer surfaces, forming characteristic rings in the shadowgram. The most-prominent ring or "bright ring" results from a single internal reflection off the inner solid/vapor interface of the ice layer. The position of the bright ring in the shadowgram is directly correlated with the position of the inner surface of the ice layer and makes it possible to characterize the nonuniformity of the inner surface. A 3-D reconstruction of the inner ice surface can be built from multiple shadowgrams from different views. Details can be found in Refs. 20 and 21.

To test the suitability of Si as a shinethrough barrier material, standard cryogenic target shells were coated with Si, then permeation filled, layered, and characterized using the standard procedures. Several typical OMEGA cryogenic shells were coated with Si using a room-temperature radio-frequency sputter coater. The Si thickness was estimated by a quartz crystal monitor, and the coating thickness was verified offline using reflected-light interferometry. The shells were affixed to a substrate with a weak adhesive and coated from above. The targets were flipped over at midpoint in the coating process to expose the other side. This single "roll-over" method produced some low-mode nonuniformity in the coating thickness, but the coverage was sufficiently uniform to test permeation filling, IR layering, or optical characterization of the Si-coated cryogenic targets. If Si barriers become common for spherical direct-drive targets, they will require a more-uniform coating technique than the roll-over method used here.

The optical shadowgrams of two Si barrier–coated cryogenic targets shown in Fig. 115.36 are proof that permeation filling and optical characterization through a Si barrier are possible. The shells, one coated with 500 Å of Si and the other with 1000 Å, were cooled to below the triple point for D_2

(18.73 K). Sufficient IR heating laser power kept the liquid layer in Fig. 115.36 from freezing. The shadowgrams in Fig. 115.36 show that both targets could be optically characterized.

A shadowgram and intensity lineout showing the ice layer of a DT permeation-filled target coated with 750 Å of Si are displayed in Fig. 115.37. The bright ring is very strong and two of the fainter inner rings are also clearly visible. A Fourier-mode power spectrum for the bright ring is shown in Fig. 115.38. The Si barrier did not significantly affect optical characterization

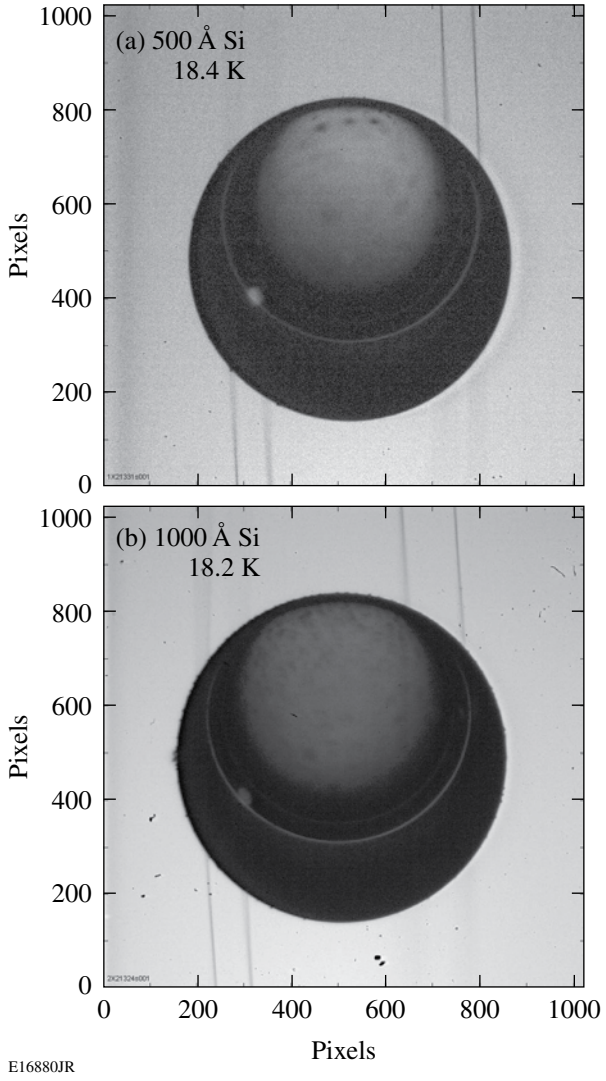

Figure 115.36
Backlit shadowgrams of permeation-filled cryogenic deuterium targets with Si shinethrough barrier coatings of (a) 500-Å and (b) 1000-Å thickness. The layering sphere temperatures are below the D_2 triple point, yet the fuel is still liquid. The off-center circular rings inside the target are the result of light internally reflecting off the vapor/liquid interface of the "bubble" inside the target.

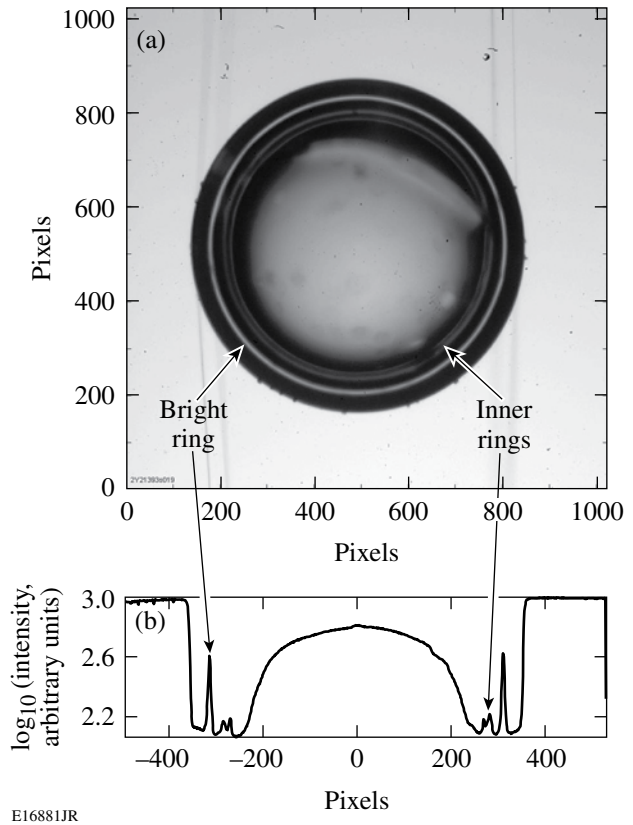

Figure 115.37
(a) Shadowgram of a Si-coated (750 Å), DT-filled cryogenic target and (b) a horizontal lineout through the target of the logarithm of the shadowgram intensity. Both the bright ring and two fainter inner rings are clearly visible through the Si barrier.

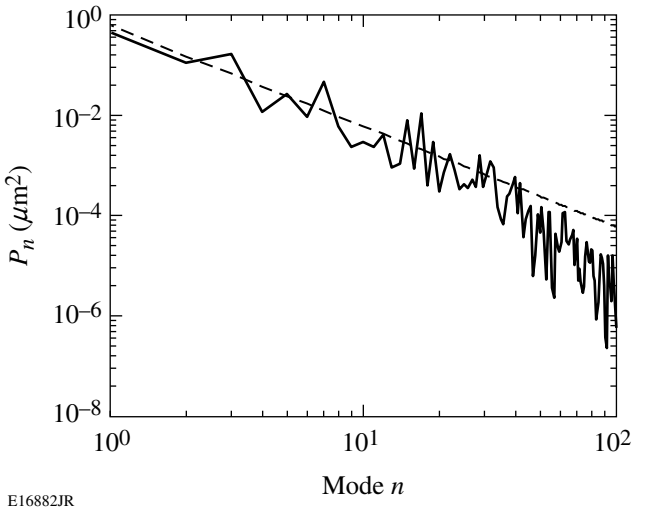

Figure 115.38
The Fourier-mode power spectrum of the bright ring (solid line) from Fig. 115.37 compared to the specification for direct-drive–ignition targets (dashed line).[9] The ice-surface rms for this view is 0.94 μm for all modes and for mode numbers 10 and above. This view is within the specification.

nor did the Si barrier inhibit beta layering of DT cryogenic targets. The surface-averaged rms (root mean square) of the ice-layer thickness for the target shown in Fig. 115.37 was 0.91 μm, one of the best layers produced to date for OMEGA.

The IR-layered, Si-coated D_2 cryogenic targets do not meet ignition specifications. Both targets shown in Fig. 115.36 showed large asymmetries when frozen with surface-averaged ice-layer-thickness nonuniformities of 6.2 μm (rms) for a 500-Å coating of Si and 11.6 μm (rms) for a 1000-Å coating of Si. While IR-layered D_2 targets typically have larger ice-layer asymmetries than DT targets, these values are among the worst in recent years and the target with the thickest Si barrier was more asymmetric. Determining whether these poor D_2 layers were statistical aberrations or were directly related to the Si coating will require further investigation.

Effectiveness of Si as a Shinethrough Barrier

Planar-target experiments were performed to verify the efficacy of Si and to determine the minimum effective thickness of Si as a shinethrough barrier material. Previous studies[11] have shown that the amount of shinethrough energy transmitted by an uncoated glass surface before a critical plasma forms is very low and is very insensitive to the incident laser intensity. The experiments were performed using a single beam at low energy (<1.5 J). The targets survived the experiments and clearly exhibited permanent shinethrough damage where there was no shinethrough barrier. Figure 115.39 shows filamentation damage streaks along the laser beam path behind an uncoated region of a glass target after exposure to a low-energy pulse (200 ps, 1.5 J).

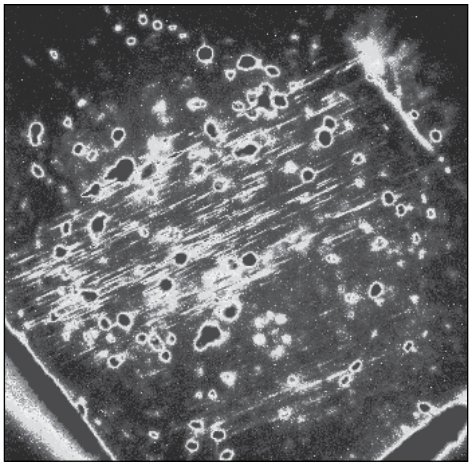

E16883JR

Figure 115.39
Post-shot close-up image of a glass-cube target ($4 \times 4 \times 4$ mm^3) showing filamentation tracks along the laser beam path through the target behind an uncoated region.

The target in this experiment was a 6-mm × 6-mm × 1-mm glass slide constructed as detailed in Fig. 115.40(a). The target front was illuminated by a laser pulse of 200-ps duration and 0.7 J of energy. An examination of the target shows a distinctive "hourglass" hole burnt into the Al coating on the back of the target corresponding to the uncoated regions on the front of the target exposed to the beam. The Al backing is intact behind both the Al and Si shinethrough barrier squares on the front of the target. This is qualitative evidence that Si was as effective at blocking shinethrough as the conventional Al barriers.

A series of experiments using VISAR (velocity interferometry system for any reflector)[22,23] tested the efficacy of Si as a shinethrough barrier during a pulse. VISAR detects a Doppler shift of a probe beam reflected off a moving surface. The interference between two paths of the probe laser, one reflected off a surface and one direct to the detector, produces fringes whose displacements are proportional to the velocity of the surface. The effect of shinethrough light on an opaque surface can be detected using VISAR. Any shinethrough energy will heat the opaque layer, causing it to expand and resulting in movement of the VISAR fringes. If the heating is sufficient to vaporize the layer, the expanding material will disrupt the VISAR fringes and blank out this fringe pattern.

For these studies, the rear surfaces of several planar glass targets were covered with 1000 Å of Al to provide a reflective surface suitable for observation by VISAR. Half of the front (laser-facing) side was coated with a Si barrier. The low-power laser beam was centered on the interface between the Si-coated and uncoated portions of the target. The VISAR probe beam was pointed at the rear of the target to sample a line across the coated/uncoated interface. The results are summarized in Fig. 115.41. The VISAR fringes behind unprotected regions are blanked out promptly at the start of the illumination pulse, indicating an ablation of the rear surface by shinethrough energy. Note that in Fig. 115.41(b) this blanking is not seen because VISAR is observed behind only the Si barrier–protected region due to error in VISAR pointing, target alignment, or target metrology. The correct timing of the VISAR image with the laser pulse has been verified using the laser timing fiducial pulses (the dots visible along the top and bottom of each VISAR image). The VISAR fringes behind portions of the targets protected by 750-Å, 300-Å, and 200-Å Si barriers [Figs. 115.41(a)–115.41(c)] are unaffected by shinethrough, indicating no detectable motion or heating of the rear surfaces

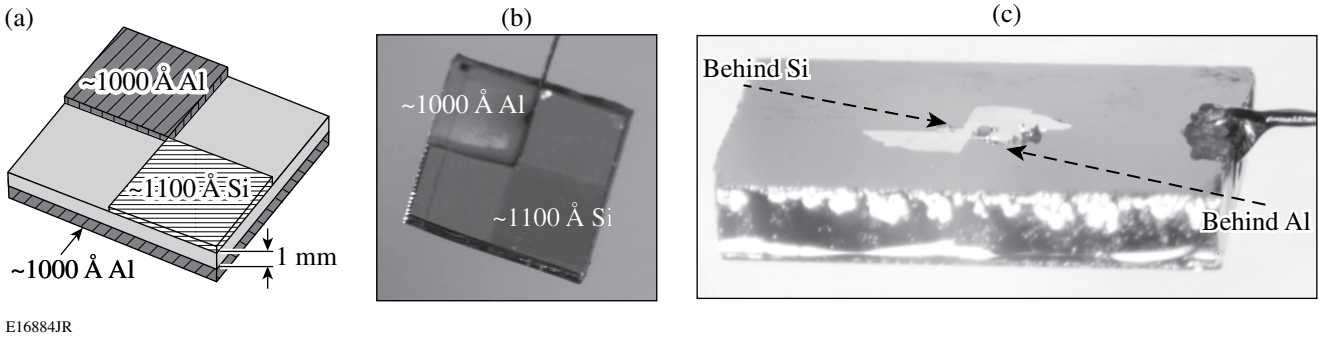

Figure 115.40
Glass-slide planar target of dimensions roughly $6 \times 6 \times 1$ mm^3. (a) Design specifications: The back side of the target was coated with 1000 Å of Al. The front (laser-facing) side of the target was 1/4 coated with 1000 Å of Al, 1/4 coated with 1100 Å of Si, and 1/2 uncoated. (b) Pre-shot photograph of target front. (c) Post-shot photograph of back of target.

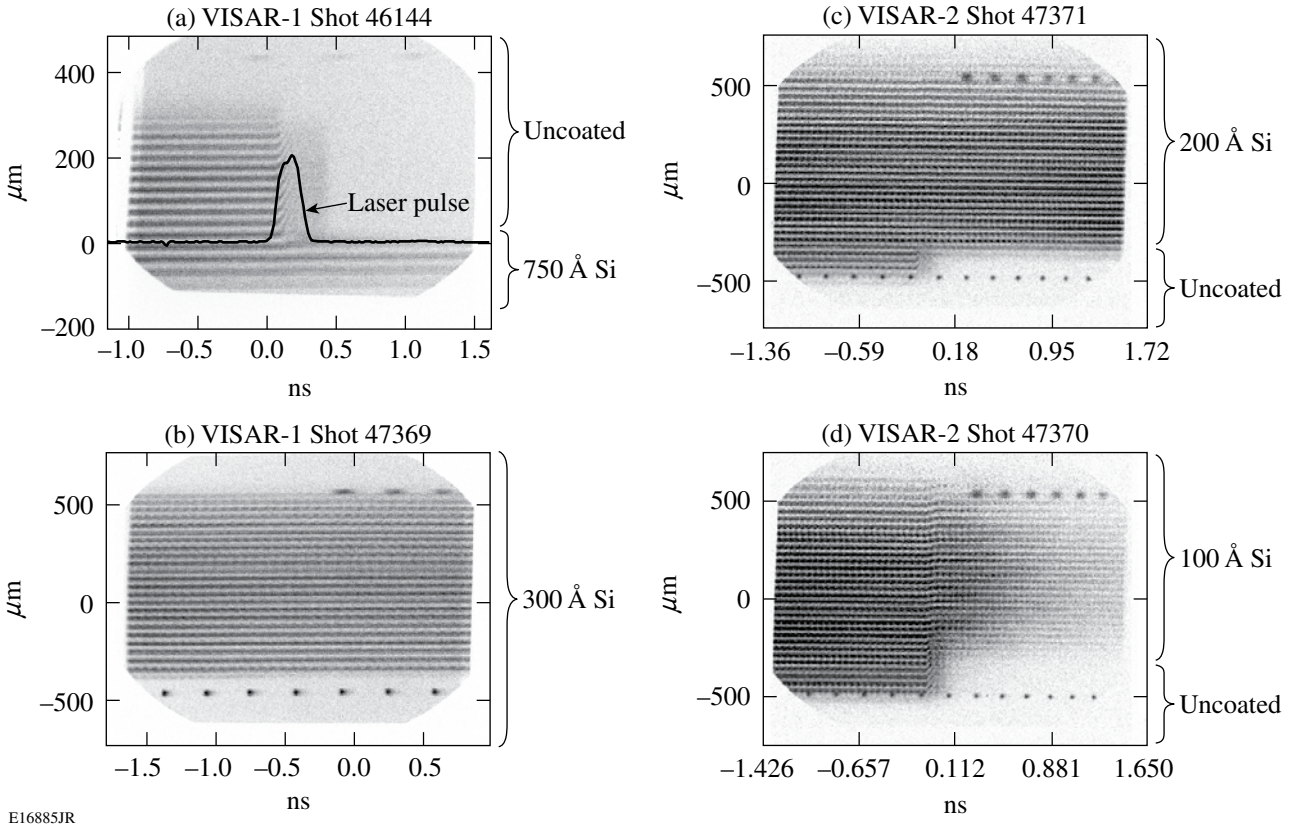

Figure 115.41
VISAR fringes for four targets half coated with different thicknesses of Si: (a) 750 Å of Si, (b) 300 Å of Si, (c) 200 Å of Si, and (d) 100 Å of Si. The back surface behind the uncoated front is clearly ablated off by shinethrough at the start of the laser pulse [shown, for example, in (a) by the black line], blanking the VISAR signal wherever these unprotected sections are observed. The sections of the target protected by Si are unaffected except for the thinnest barrier layer in (d), where there is evidence of fringe motion behind the Si barrier–protected region, indicating motion/heating of the rear surface.

behind these barriers. Because the damage-threshold fluence for CH plastic is twice that for Al (Ref. 24), we conclude that these barrier thicknesses would have prevented shinethrough damage to an ICF plastic-shell target. In Fig. 115.41(d), however, the VISAR fringes show a slight motion of the surface behind a 100-Å Si barrier at the start of the pulse, clearly proving that some shinethrough energy has penetrated the Si barrier. From this VISAR data we conclude that a 100-Å Si coating is inadequate as a shinethrough barrier. A barrier layer of 200 Å of Si should be sufficient to block shinethrough light for 351-nm-laser–driven, direct-drive ICF plastic-shell targets. As previous studies[11] have shown that the total shinethrough energy transmitted before a critical surface forms in the coronal plasma is insensitive to the incident energy or intensity, this thickness should not need to be scaled for other experimental conditions. A 200-Å Si barrier should be sufficient to block shinethrough energy during the earliest part of the laser pulse before the coronal plasma reaches critical density in ICF and ignition experiments.

Discussion

These experiments have shown that direct-drive ICF cryogenic targets coated with up to 1000 Å of Si as a shinethrough barrier can be successfully permeation filled, beta-layered, and characterized. However, to minimize the effects of the barrier on these processes (such as the attenuation of light used to characterize the ice layer), we recommend using the minimum effective shinethrough barrier thickness of 200 Å of Si. This minimum thickness may also alleviate the possible difficulties with IR layering D_2 targets found in this study's limited sample set.

ACKNOWLEDGMENT

This work was supported by the U.S. Department of Energy Office of Inertial Confinement Fusion under Cooperative Agreement No. DE-FC52-08NA28302, the University of Rochester, and the New York State Energy Research and Development Authority. The support of DOE does not constitute an endorsement by DOE of the views expressed in this article.

REFERENCES

1. J. Nuckolls *et al.*, Nature **239**, 139 (1972).
2. D. D. Meyerhofer, J. A. Delettrez, R. Epstein, V. Yu. Glebov, V. N. Goncharov, R. L. Keck, R. L. McCrory, P. W. McKenty, F. J. Marshall, P. B. Radha, S. P. Regan, S. Roberts, W. Seka, S. Skupsky, V. A. Smalyuk, C. Sorce, C. Stoeckl, J. M. Soures, R. P. J. Town, B. Yaakobi, J. D. Zuegel, J. Frenje, C. K. Li, R. D. Petrasso, D. G. Hicks, F. H. Séguin, K. Fletcher, S. Padalino, C. Freeman, N. Izumi, R. Lerche, T. W. Phillips, and T. C. Sangster, Phys. Plasmas **8**, 2251 (2001).
3. Lord Rayleigh, Proc. London Math Soc. **XIV**, 170 (1883).
4. G. Taylor, Proc. R. Soc. London Ser. A **201**, 192 (1950)
5. V. Lobatchev and R. Betti, Phys. Rev. Lett. **85**, 4522 (2000).
6. M. C. Herrmann, M. Tabak, and J. D. Lindl, Phys. Plasmas **8**, 2296 (2001).
7. R. Betti, K. Anderson, V. N. Goncharov, R. L. McCrory, D. D. Meyerhofer, S. Skupsky, and R. P. J. Town, Phys. Plasmas **9**, 2277 (2002).
8. R. P. J. Town and A. R. Bell, Phys. Rev. Lett. **67**, 1863 (1991).
9. P. W. McKenty, V. N. Goncharov, R. P. J. Town, S. Skupsky, R. Betti, and R. L. McCrory, Phys. Plasmas **8**, 2315 (2001).
10. J. E. Balmer, T. P. Donaldson, W. Seka, and J. A. Zimmermann, Opt. Commun. **24**, 109 (1978).
11. D. K. Bradley, T. Boehly, D. L. Brown, J. Delettrez, W. Seka, and D. Smith, in *Laser Interaction and Related Plasma Phenomena*, edited by H. Hora and G. Miley (Plenum Press, New York, 1991), Vol. 9, pp. 323–334.
12. J. Delettrez, D. K. Bradley, P. A. Jaanimagi, and C. P. Verdon, Phys. Rev. A **41**, 5583 (1990).
13. M. Nishikino *et al.*, Bull. Am. Phys. Soc. **46**, 142 (2001).
14. J. M. Soures, J. Fusion Energy **10**, 295 (1991).
15. Y. Fisher, T. R. Boehly, D. K. Bradley, D. R. Harding, D. D. Meyerhofer, and M. D. Wittman, Bull. Am. Phys. Soc. **43**, 1784 (1998).
16. D. R. Harding, T. C. Sangster, D. D. Meyerhofer, P. W. McKenty, L. D. Lund, L. Elasky, M. D. Wittman, W. Seka, S. J. Loucks, R. Janezic, T. H. Hinterman, D. H. Edgell, D. Jacobs-Perkins, and R. Q. Gram, Fusion Sci. Technol. **48**, 1299 (2005).
17. J. K. Hoffer and L. R. Foreman, Phys. Rev. Lett. **60**, 1310 (1988).
18. A. J. Martin, R. J. Simms, and R. B. Jacobs, J. Vac. Sci. Technol. A **6**, 1885 (1988).
19. D. N. Bittner *et al.*, Fusion Technol. **35**, 244 (1999).
20. D. H. Edgell, W. Seka, R. S. Craxton, L. M. Elasky, D. R. Harding, R. L. Keck, and M. D. Wittman, Fusion Sci. Technol. **49**, 616 (2006).
21. D. H. Edgell, R. S. Craxton, L. M. Elasky, D. R. Harding, S. J. Verbridge, M. D. Wittman, and W. Seka, Fusion Sci. Technol. **51**, 717 (2007).
22. L. M. Barker and R. E. Hollenbach, J. Appl. Phys. **43**, 4669 (1972).
23. P. M. Celliers, D. K. Bradley, G. W. Collins, D. G. Hicks, T. R. Boehly, and W. J. Armstrong, Rev. Sci. Instrum. **75**, 4916 (2004).
24. T. R. Boehly, Y. Fisher, D. D. Meyerhofer, W. Seka, J. M. Soures, and D. K. Bradley, Phys. Plasmas **8**, 231 (2001).

Elimination of Self-Pulsations in Dual-Clad, Ytterbium-Doped Fiber Lasers

Introduction

High-power, high-beam-quality, stable continuous-wave (cw) fiber lasers are desired in sensing, ranging, telecommunications, and spectroscopy.[1,2] Although high-output powers have been achieved in many high-power fiber laser systems,[3] self-pulsing often occurs in cw fiber lasers under specific pumping and cavity conditions.[4] Generally, self-pulsing in fiber lasers can be classified as sustained self-pulsing (SSP) and self-mode-locking (SML). SSP is the periodic emission of optical pulses at a repetition rate corresponding to the relaxation oscillation frequency of the inversion and photon populations. SML is the periodic emission of optical pulses with a rate corresponding to the cavity-round-trip time.[5] Both of the regimes can be described by the interaction of the photon population and the population inversion.[6]

Although the self-pulsations typically occur at the lower end of the pump power range, the pulses caused by these instabilities carry sufficient optical energy to cause catastrophic damage to the fiber laser, particularly when they are allowed to occur for extended periods of time. For this reason, there have been intensive investigations on self-pulsation suppression in cw fiber lasers. Electronic feedback has been used on the pump laser to shift the gain and phase to minimize relaxation oscillations.[7] Auxiliary pumping near the lasing wavelength sustains the population inversion in the gain medium, thereby preventing rapid gain depletion and minimizing the relaxation oscillations.[8] The fast saturable gain of a semiconductor optical amplifier included within the fiber-laser cavity prevents large signal buildup in the fiber laser and suppresses the self-pulsing behavior.[9] The narrow passband of a $\lambda/4$-shifted fiber Bragg grating (FBG) structure in a ring cavity limits the number of longitudinal cavity modes and suppresses self-pulsations.[10] In this article, increasing the round-trip time in the cavity by inserting a long section of passive fiber is shown to change the relaxation oscillation dynamics and make it possible to completely eliminate self-pulsations at all pumping levels. This technique is much simpler to implement than the alternative methods described above.

Experimental Results

The experimental setup is shown in Fig. 115.42. The 25-W pump light at a wavelength of 915 nm is delivered by the pump coupling fiber, which has a 200-μm core diameter and 0.22 numerical aperture (N.A.) with aspheric lenses of focal lengths 27 mm and 13.5 mm. The overall pump coupling efficiency is 75%. The laser gain medium is a 20-m, dual-clad, ytterbium-doped, single-mode fiber with an absorption rate of 0.5 dB/m at 915 nm. This ytterbium-doped fiber has a 130-μm cladding diameter with an N.A. of 0.46. The fiber has a core diameter of 5 μm with an N.A. of 0.12. One end of the fiber is spliced into an FBG having a 3-dB bandwidth of 0.36 nm and >99% reflectivity at a center wavelength of 1080 nm. The other end of the active fiber is cleaved perpendicularly, providing a 4% reflection at the fiber–air interface. A dichroic mirror is inserted between the aspheric lenses to couple the laser output signal into a 2-GHz-bandwidth optical detector and a 600-MHz-bandwidth oscilloscope to measure laser dynamics. Three additional configurations are characterized in this experiment. In these alternate configurations, three long sections of passive fiber (329 m, 1329 m, and 2329 m) are spliced into the laser cavity between the active fiber and the FBG. The four lasers are designated as laser 1 (20-m cavity), laser 2 (349-m cavity), laser 3 (1349-m cavity), and laser 4 (2349-m cavity).

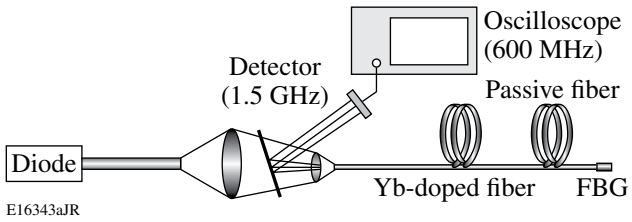

Figure 115.42
Schematic diagram of the ytterbium-doped fiber laser. FBG is the fiber Bragg grating.

The lasing properties of the four configurations have been characterized. The four lasers have about the same pump threshold of 0.75 W. At maximum pump power, the difference in output power between the four lasers is less than 9% due to the scattering loss of the passive fiber sections. Both SSP and SML have been observed in laser 1. A cw optical output is observed with low pump powers. As the injected pump power is increased beyond 2.0 W, quasi-periodic optical pulses, induced by undamped relaxation oscillations, are observed in the SSP regime. Figure 115.43 shows an example of such pulsations when the pump power is 3.2 W. The pulse period is around 20 μs, which agrees with the calculated relaxation oscillation frequency of the laser. As the pump power is tuned higher to 6.6 W, SML pulsing at a rate corresponding to a cavity-round-trip time is observed. This regime occurs because the gain medium is pumped hard enough to recover the population inversion in a single-cavity-round-trip time. Figure 115.44 shows an example of such pulsations when the pump power is 7.2 W. The measured pulse period of 290 ns corresponds to the round-trip time of the laser cavity. As the pump power is further increased beyond 7.5 W, the laser once again operates in the cw regime because the gain is replenished more rapidly than the time it takes for the pulse to complete a round-trip through the laser cavity.

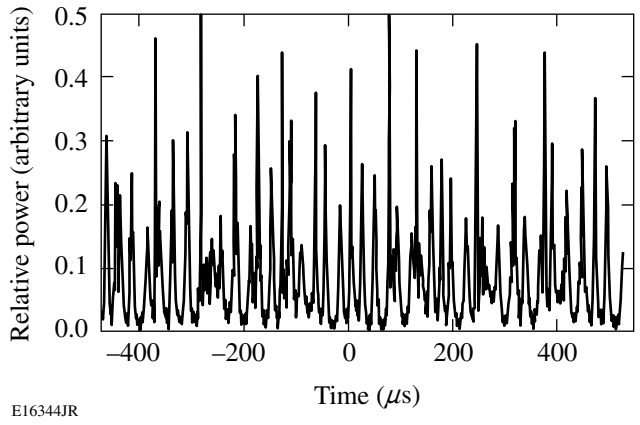

Figure 115.43
The self-pulsing dynamics of laser 1 when the pump power is 3.2 W.

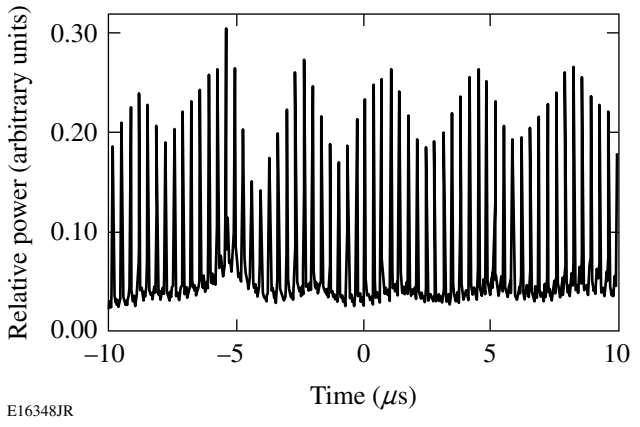

Figure 115.44
The self-pulsing dynamics of laser 1 when the pump power is 7.2 W.

Analysis

The physics underscored here implies that when the pumping rate is sufficiently fast compared to the relaxation oscillation dynamics, the gain will always be replenished before a pulse can build up in the cavity. The dynamics in the SSP regime are dependent on the cavity length such that the relaxation oscillation frequency becomes smaller with increasing cavity length, as governed by conventional laser theory. The dynamics in the SML regime are directly dependent on the cavity length since the laser mode locks to the cavity-round-trip time. Therefore, by sufficiently increasing the cavity length, all self-pulsation dynamics can be slowed down compared to the pumping rate and all self-pulsations will be eliminated.

The modulation depth of the pulsations, defined as the ratio of the peak-to-valley value of the modulation to the peak value, indicates the competition between self-pulsing and cw working regimes. Figure 115.45 shows the modulation depth as a function of pump power for the four laser cavities. As predicted by fiber-laser rate equations,[11] the modulation depth decreases as the fiber-laser cavity length is increased, indicating a stronger tendency toward cw operation. In addition, the pump range where self-pulsations occur also decreases drastically with increasing cavity length. Laser 2 has an instability range that is less than 19% of that of laser 1, while laser 3 has an instabil-

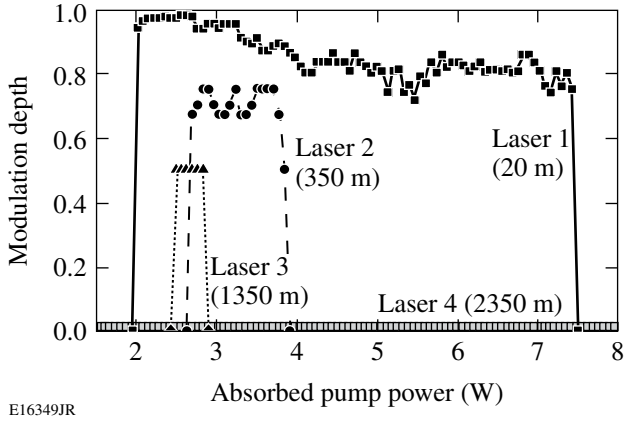

Figure 115.45
The self-pulsing characteristics of the fiber lasers with four different cavity lengths. The active fiber length is 20 m in all four cases

ity range that is less than 7% of that of laser 1. For laser 4, the instability range reduces to zero and no self-pulsations occur over the entire pump range.

For fiber lasers having long cavity lengths such as in laser 4, stimulated Raman scattering (SRS) can occur at high-power levels. In the experiments described above, no SRS spectra above the noise floor were observed, but SRS can be induced at higher pump levels. For example, a laser with a 1-km cavity length has an SRS threshold of about 5 W. SRS can be mitigated with appropriate filters, such as wavelength-division multiplexers, in-line short-pass filters, or hole-assisted single-polarization fibers.[12] Large-mode-area fiber can also be used to suppress SRS in long fiber lasers. For example, higher-order-mode (HOM) fiber with a mode-field diameter of 86 μm (Ref. 13) can increase the nonlinear threshold by a factor of 200 compared to normal single-mode fiber. By inserting a 1-km passive HOM delay fiber into the laser cavity, the effective fiber length that contributes to the nonlinearity is about 5 m, mitigating the SRS impairment of such a long-cavity fiber laser.

Using long lengths of passive fiber to suppress self-pulsing has many advantages over other methods. No active components or electronics are required, resulting in reduced system complexity. This method does not require free-space alignment and can be easily integrated into existing laser systems. Even though our demonstration was in an ytterbium-doped fiber laser, the technique can be applied to any rare-earth-doped fiber laser (e.g., erbium). Additionally, the laser output power degrades only a few percent due to the scattering loss so that high-efficiency performance can be maintained.

Conclusion

In conclusion, suppression and elimination of self-pulsing in a watt-level, dual-clad, ytterbium-doped fiber laser have been demonstrated. Self-pulsations are caused by the dynamic interaction between the photon population and the population inversion. The addition of a long section of passive fiber in the laser cavity makes the gain recovery faster than the self-pulsation dynamics, allowing only stable continuous-wave lasing. This scheme provides a simple and practical method requiring no active devices for eliminating self-pulsations in fiber lasers at all pumping levels.

ACKNOWLEDGMENT

This work was supported by the U.S. Department of Energy Office of Inertial Confinement Fusion under Cooperative Agreement No. DE-FC52-08NA28302, the University of Rochester, and the New York State Energy Research and Development Authority. The support of DOE does not constitute an endorsement by DOE of the views expressed in this article.

REFERENCES

1. L. Qiu *et al*., IEEE Photonics Technol. Lett. **16**, 2592 (2004).
2. W. Guan and J. R. Marciante, Electron. Lett. **43**, 558 (2007).
3. Y. Jeong *et al*., Opt. Express **12**, 6088 (2004).
4. A. Hideur *et al*., Opt. Commun. **186**, 311 (2000).
5. F. Brunet *et al*., J. Lightwave Technol. **23**, 2131 (2005).
6. M. Dinand and Ch. Schütte, J. Lightwave Technol. **13**, 14 (1995).
7. V. Mizrahi *et al*., J. Lightwave Technol. **11**, 2021 (1993).
8. L. Luo and P. L. Chu, Opt. Lett. **22**, 1174 (1997).
9. H. Chen *et al*., Appl. Opt. **41**, 3511 (2002).
10. A. Suzuki *et al*., IEEE Photonics Technol. Lett. **19**, 1463 (2007).
11. M. Ding and P. K. Cheo, IEEE Photonics Technol. Lett. **8**, 1151 (1996).
12. D. A. Nolan *et al*., Opt. Lett. **29**, 1855 (2004).
13. S. Ramachandran *et al*., Opt. Lett. **31**, 1797 (2006).

Resolving Dark Pulses from Photon Pulses in NbN Superconducting Single-Photon Detectors

Introduction

Fast and reliable single-photon detectors (SPD's) have become a highly sought after technology in recent years.[1] Some of the most interesting applications for SPD's, which include quantum communications and quantum key distribution,[2] as well as satellite communications, require devices that can successfully operate at telecommunication wavelengths, namely 1310 nm and 1550 nm. Another desirable feature for an ideal SPD is its photon-number resolution (PNR) capability.[3,4] InGaAs avalanche photodiodes work at telecommunication wavelength and are commercially available; they do, however, suffer from severe after-pulsing and require time gating, which limits their maximum count rate. Presently, they also lack the PNR capability.[5,6]

It has already been established that nanostructured, NbN superconducting single-photon detectors (SSPD's) operate based on hotspot formation and bias current redistribution in ultrathin (4 nm), narrow (100- to 120-nm), and long (~0.5-mm) meandering NbN superconductive stripes.[1] NbN SSPD's have been shown to have counting rates exceeding 250 MHz, with reported quantum efficiencies (QE's) up to 57% (Ref. 7) at 1550-nm wavelength and very low dark-count rates, ~10 Hz to 10 kHz, depending on the operation bias point.[8]

Typically, the SSPD's are kept at temperatures between 4.2 and 1.7 K (far below the NbN critical temperature T_c), and biased at currents I_{bias} close to the meandering stripe critical current I_c. Once a photon is absorbed by the NbN nanostripe, it breaks a Cooper pair, and, subsequently, a large number of quasiparticles are generated through the electron–electron and electron–phonon interactions, creating a local hotspot where superconductivity is suppressed or even destroyed. The hotspot expels the supercurrent from its volume and forces it to flow near the stripe edges, where it can exceed the I_c value, leading to the generation of phase-slip centers and the eventual formation of a resistive region across the width of the stripe.

When the device is directly connected to a transmission line with the characteristic impedance Z_0 equal to, e.g., 50 Ω, the above-mentioned resistive region, which is >50 Ω, forces the bias current to redistribute from the SSPD into the load, which means that the amplitude of the SSPD voltage response is always simply the $Z_0 I_{bias}$ product. The above conclusion is true even if the SSPD were illuminated by several photons and, consequently, several hotspots were simultaneously generated at various points along the meander. Thus, in the above typical experimental arrangement, the SSPD photoresponse is insensitive to the number and energy of incoming photons.

We need to stress that a biased SSPD can generate output electrical pulses even when the input light is completely blocked and there are no photons incident upon the device. The dark-count pulses are transient voltage signals, spontaneously generated in a current-biased, long, superconducting nanostripe, and their amplitude, when the device is connected to a 50-Ω line, is also close to $Z_0 I_{bias}$, despite the fact that their physical origin is different from the photon counts. In the case of dark counts, the transient resistive state across the SSPD stripe is, actually, due to the current-induced vortex–antivortex generation.[9,10]

The goal of this work is to show that, with our proposed new readout scheme, which implements a low-noise cryogenic amplifier and a high-load resistor next to the detector, we are able to resolve the difference between dark counts and photon counts in our devices. The same readout approach also leads to the photon-number–resolving and energy-resolving capabilities in our standard SSPD's,[11] making the SSPD a PNR-type and/or an energy-sensitive photon sensor.

Device Description and Experimental Setup

SSPD's are patterned from epitaxial-quality NbN films, deposited by dc reactive magnetron sputtering onto sapphire substrates.[12] The films are characterized by a sheet resistance between 400 and 500 Ω/sq at room temperature, with T_c between 10 and 11 K, and the critical current density $J_c \approx 10^6$ A/cm^2. The meander patterning is done by e-beam lithography and reactive ion etching. The films were deposited at the Moscow State Pedagogical University and patterned at Delft University of Technology. Perhaps because of the slight

differences in geometry, or slight patterning technique differences, the SSPD's in this work had three to four times lower I_c's (~5 to 10 μA) than the typical Moscow fabricated and patterned devices.[12] The QE's, however, were on par with the standard 10×10-μm^2 SSPD's, with the devices measured in this work having QE $\approx 4\%$ at $\lambda = 800$ nm.

The standard SSPD operation setup is shown in Fig. 115.46(a). The device is wire bonded to a 50-Ω microstrip transmission line, coupled to a multimode optical fiber, and immersed into liquid helium.[13] The microstrip is then connected to a semirigid coaxial cable and at room temperature connected to a wideband bias-tee (0.08- to 26-GHz bandwidth). The bias-tee makes it possible to simultaneously amplify the transient photoresponse signal using a tandem of two broadband amplifiers (0.08- to 8.5-GHz bandwidth, 22-dB gain) and bias the SSPD by a stable low-noise dc voltage source. The amplified output signals, corresponding to photon counts and/or dark counts, are recorded by using either a Tektronix TDS 6604 digital single-shot (6-Ghz-bandwidth) oscilloscope or a pulse counter. As a single-photon source, we use a tunable Ti:sapphire mode-locked laser, heavily attenuated. For dark-count measurements, the detector was blocked from all incoming radiation, i.e., shielded inside the dewar by a metallic enclosure.

An equivalent electrical model of the SSPD photoresponse is shown in Fig. 115.46(b). Kinetic inductance L_k is in series with a parallel arrangement of a hotspot resistance R_{hs} and a switch S represents the photodetection (switching) event in the SSPD. The detector is then connected to a dc bias source and a readout circuit, which consists in this case of a transmission line and amplifier with input impedance $Z_0 = 50\ \Omega$. In the simulations, which will be presented later, a bandpass filter representing the amplifier bandwidth is added. Finally, V_{out} is the experimentally observed transient voltage pulse during photodetection.

Initially, the switch is closed, and there is no voltage drop. Once a photon is absorbed by our nanostripe, the switch opens, and as R_{hs} grows to a value much larger than Z_0, most of the current redistributes into Z_0, and the resultant voltage pulse amplitude is simply $V_{out} \approx GI_{bias}Z_0$, where G is the amplifier gain. Thus, independent of the number or energy of the absorbed incident photons, V_{out} always has the same value for a given I_{bias} for the circuit shown in Fig. 115.46.

The new readout scheme presented here implements a high-electron-mobility transistor (HEMT) amplifier, operated cryogenically and mounted next to (on the same board) the SSPD. Because the HEMT input impedance is very high, a 500-Ω load (or shunt) resistor R_L is utilized in parallel with the detector and the HEMT, as shown in Fig. 115.47, which presents the circuit schematics. By applying the detector transient response to the gate of the HEMT, one can read out the amplified drain voltage, which should, ideally (for $R_L \gg R_{hs}$), be proportional to the hotspot resistance and equal to $V_{out} \approx GI_{bias}R_{hs}$. If the number of photons simultaneously absorbed in the SSPD meander happens to be larger than 1, the photons are very likely to form separate hotspots and their resistances will add up in series. The HEMT output voltage in this case should be $V_{out} \approx GI_{bias}nR_{hs}$, where n is the number of absorbed photons per pulse (actually, the number of created hotspots).

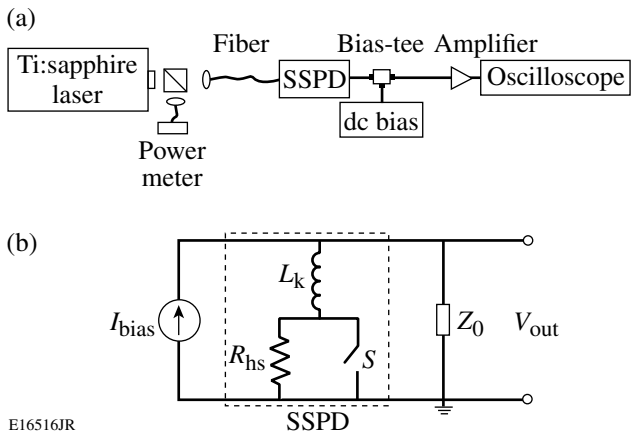

Figure 115.46
(a) Experimental setup and (b) standard electrical photoresponse model of an SSPD.

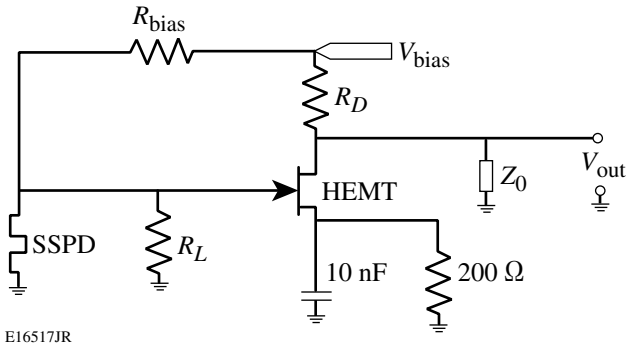

Figure 115.47
Circuit schematics implementing an HEMT amplifier and a 500-Ω load resistor R_L. The 10-nF capacitor sets the maximum ac gain and the 200-Ω resistor sets the dc current for the HEMT; R_{bias} and R_D are the biasing and pull-up resistors, respectively.

Thus, for relatively small n's, and $nR_{hs} < R_L$, the output pulse height of our setup is proportional to n, effectively leading to PNR.[11]

The HEMT setup should also enable one to distinguish pulses generated in response to either a single-photon absorption event (photon count) or a spontaneous voltage transient (dark count). In the case of dark counts, one can expect only a single localized resistive region, created due to the vortex–antivortex motion across the stripe, but its effective resistance should be different than R_{hs}, resulting in a somewhat different value of V_{out}.

Figure 115.48 compares photon-count time traces for the SSPD connected according to the standard scheme (Fig. 115.46) and the one with HEMT (Fig. 115.47). Even from this very short time trace, one can clearly see that with the standard-technique pulse amplitudes do not vary as much as those where the HEMT is utilized.

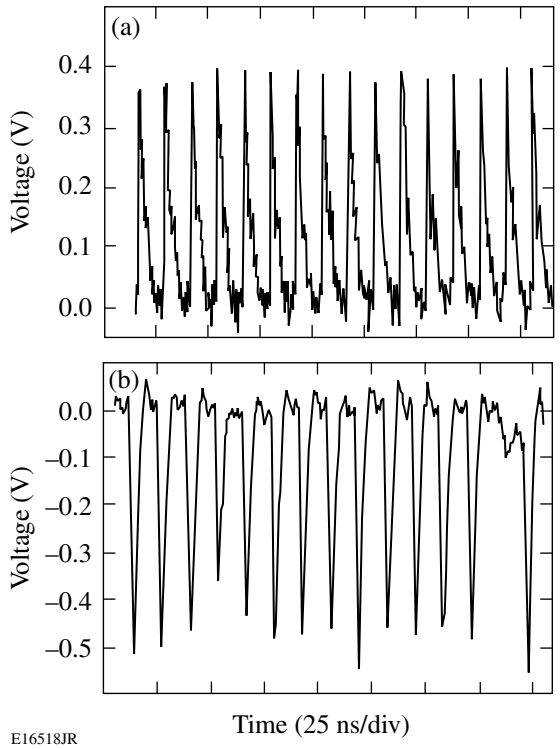

Figure 115.48
Comparison of real-time oscilloscope time-domain traces for (a) a traditional scheme (50-Ω load line) and (b) an HEMT readout scheme, taken at similar laser intensities, such that $n \leq 1$ (HEMT is an inverting amplifier; therefore, the pulses are negative). The repetition rate of the laser was 82 MHz.

Results and Discussion

In the experiments reported here, 700-nm-wavelength photons were used to compare time traces of photon events with dark-count events. Figure 115.49 shows histograms that compare pulse-amplitude distributions of the dark-count [Fig. 115.49(a)] and photon-count events [Figs. 115.49(b) and 115.49(c)] at two different laser intensities. All data were taken at the same bias current $I_{bias} = 0.9\ I_c$.

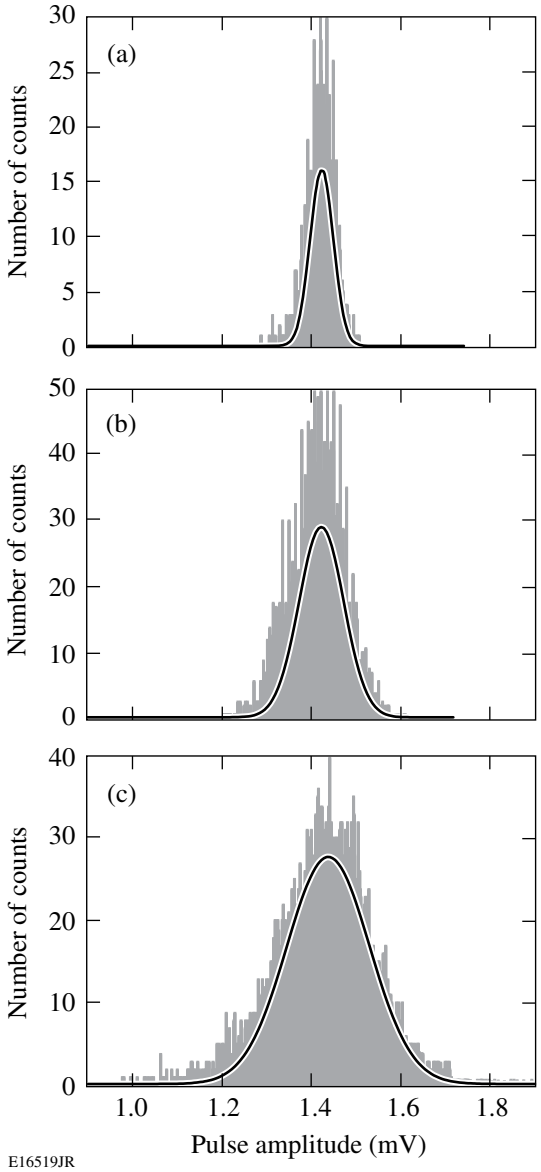

Figure 115.49
(a) Pulse-amplitude histograms of dark counts, (b) photon counts in the single-photon regime, $n \ll 1$, (c) and multiphoton regime, $n \geq 1$. All measurements performed at 4.2 K and at $I_{bias} = 0.9\ I_c$. The SSPD output voltage amplitudes (x axis) are divided by the amplifier gain.

All histograms can be fit with a simple Gaussian function, and it is quite obvious from Fig. 115.49(a) that the dark counts have the narrowest distribution. It was shown previously[10] that, when the detector is blocked from all incoming radiation and placed in liquid helium shielded by a metallic enclosure, the spontaneous transient voltage pulses, or dark counts, are most likely due to topological excitations. The NbN film thickness of our devices is 4 nm, which puts the SSPD nanowire in a two-dimensional (2-D) superconductor regime because its thickness is smaller than the NbN Ginzburg–Landau coherence length. In 2-D systems in general, true long-range superconducting order is not possible, and in an ultrathin film, topological excitations come in the form of vortex–antivortex pairs (VAP's).[14] VAP's are superconducting analogous to electron-hole excitations in semiconductors.[15] At the typical SSPD operating temperature, and in the absence of I_{bias}, all VAP's are bound and there is no dissipation in the NbN film. Once I_{bias} is applied, it exerts a Lorentz force on the VAP's, and at I_{bias} close to I_c, this force is strong enough to exceed the VAP binding energy and break them. The latter effect creates free vortices (analog to excited carriers in semiconductors) and allows vortices and antivortices to move in opposite directions toward the edges of the NbN stripe, causing dissipation, and, in turn, the resistive state and Joule heating. The dark-counting rate in SSPD's falls off quasi-exponentially with the biasing current.[10]

The photon-count amplitude distributions shown in Figs. 115.49(b) and 115.49(c), collected when the detector was irradiated by 700-nm photons, are clearly wider than that corresponding to the dark counts, even in the single-photon regime [Fig. 115.49(b)], when the average number of photons per pulse in the optical beam incident upon the SSPD is $n \ll 1$ (e.g., 0.01 photons per pulse). When the laser intensity was increased such that $n \geq 1$, we can see that the full width at half maximum (FWHM) of the distribution shown in Fig. 115.49(c) became over two times wider than that in Fig. 115.49(a).

The correlation between the beam intensity (average number of photons per pulse) incident upon the detector and the distribution FWHM of the response signals was very reproducible, and, as presented in Fig. 115.50, it depended on the SSPD bias current. One can clearly see that the dark-count signals (open squares) exhibit overall the narrowest distribution, which, in addition, is independent of the bias current.

For photon counts, the general trend is that the distribution width increases somewhat with increasing I_{bias}, and there is a wide jump between FWHM's corresponding to the multiphoton ($n \geq 1$, closed triangles) and single-photon ($n < 1$, closed circles and open triangles) illumination. However, for $n \ll 1$ (closed circles), as I_{bias} approaches I_c, the dark counts start to dominate over the photon counts and the amplitude distribution width starts to drop around $I_{bias} = 0.83\ I_c$, eventually overlapping with open squares at $I_{bias} > 0.9\ I_c$. The latter behavior agrees very well with our earlier observation that the rate of photon and dark counts depends on the I_{bias}/I_c ratio, as shown in the inset of Fig. 115.50.

When the laser intensity is set so that $n \geq 1$ (closed triangles in Fig. 115.50), one can observe the widest distribution width of the SSPD response pulse. We believe that this behavior is related to the non-perfect fabrication of SSPD's, resulting in some variations in the width or even the thickness of an NbN

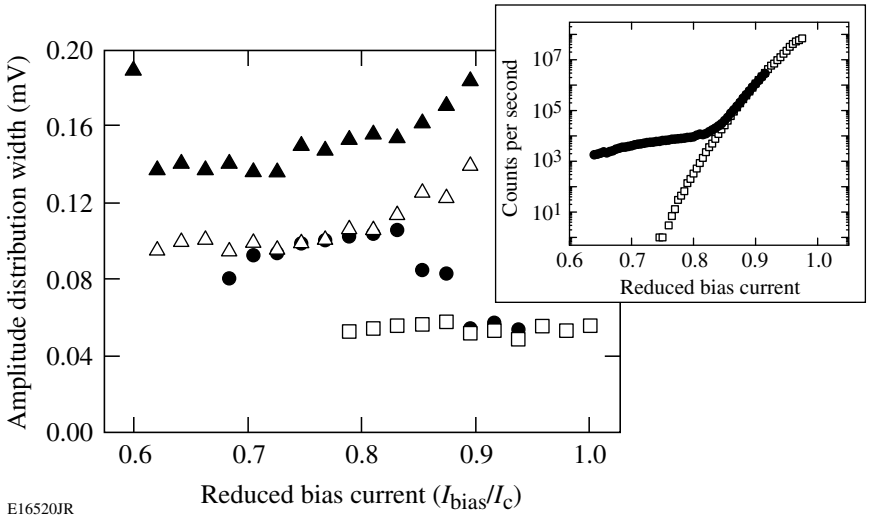

Figure 115.50
Amplitude distribution width (FWHM of Gaussian fits) for dark counts (open squares), $n \ll 1$ (closed circles), $n \leq 1$ (open triangles), and $n \geq 1$ (closed triangles). The inset shows the counting rate as a function of bias current for dark counts (open squares) and $n \ll 1$ (closed circles).

meander stripe. Since the device I_c is determined by the narrowest and thinnest section(s) of the stripe, fluctuations in the stripe width must lead to variations of the final hotspot resistance, which in turn correspond to the broadened amplitude distributions of the photon-count responses. When light intensity is increased ($n \geq 1$), more sections of the SSPD meander with, and apparently, different widths are activated, leading to enhanced fluctuations in the response pulse amplitudes and, finally, to the largest value of the distribution FWHM.

Electrical Model and PSpice Simulations

If the electrical model only is considered, the difference in amplitude, for different hotspot resistances, stems from the time it takes for the current that initially biases the device to redistribute into the readout circuit. In other words, for a given R_L, current redistribution time decreases with increasing R_{hs}. For the hotspot to stop growing, and the cooling mechanism to take over, the current through the device must drop to a value below ~0.23 I_c (Ref. 16). When the SSPD photoresponse is modeled such that R_{hs} is a simple resistor, then the fall and rise time constants of the transient V_{out} are simply $\tau_{fall} = L_k / (R_{hs} + R_L)$ and $\tau_{rise} = L_k / R_L$ (Ref. 17), respectively. Unfortunately, this latter behavior is undesired if we want to observe PNR since, for a given R_L, the current redistribution time for two hotspots, which follows $\tau_{fall} = L_k / (2R_{hs} + R_L)$ occurs faster than that for a single hotspot.

For PSpice modeling, the value of R_L was chosen to be 500 Ω, even though it was suspected that this value might be lower than the hotspot resistance. The reason is that higher R_L values can lead to an underdamped circuit because, as can be seen in Fig. 115.47, there is a large inductor (~400-nH kinetic inductance of the SSPD) in parallel with R_L. In addition, in our readout circuit there is always a small parasitic capacitance estimated to be around 2 to 3 pF (coming from a circuit board, as well as other components). Figure 115.51(a) shows the PSpice simulated pulses for different values of R_L, and as can be seen, even for R_L = 500 Ω (gray solid curve), the circuit is already slightly underdamped, as there is a small oscillation following the main pulse. Figure 115.51(b) shows the experimental (solid curve), as well as simulated (dashed curve), voltage pulses for our HEMT readout approach. The broader, more-damped oscillation behind the measured main pulse is likely due to some second-order effects from the amplifier and/or stainless steel coaxial line. Critical damping yielded R_L = 270 Ω [dashed curve in Fig. 115.51(a)], which is actually a smaller value than the estimated hotspot resistance.

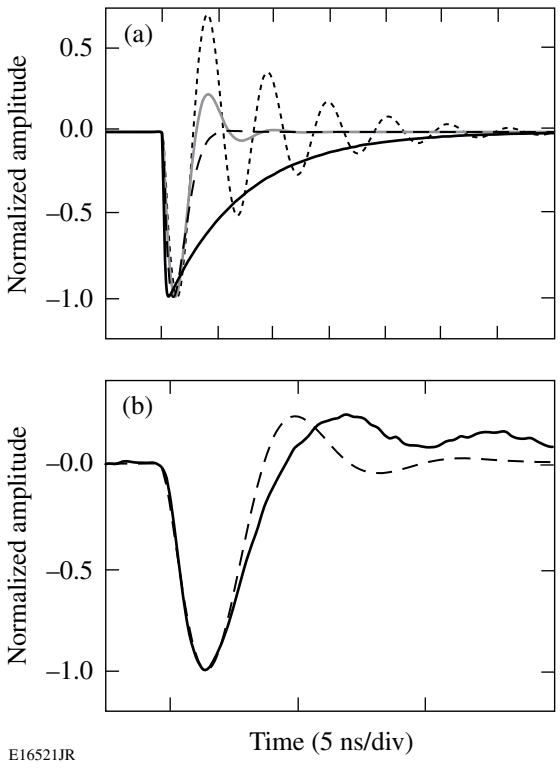

Figure 115.51
(a) PSpice simulations of voltage transients at different values of R_L: 50 Ω (black solid curve), 270 Ω (dashed curve), 500 Ω (gray solid curve), and 2 kΩ (short-dashed curve); (b) measured photoresponse (solid curve) and simulated photoresponse (dashed curve), for R_L = 500 Ω.

Finally, it must be mentioned that in order to fully model the behavior of an SSPD integrated with an HEMT readout, it is not enough to simply use the above electrical model, as there are many processes at play simultaneously. The Joule heating occurs in parallel with the cooling process and current redistribution,[18] so, ultimately, a more-complex physical model must be used, which is outside the scope of this work.

Toward Photon-Number Resolution

As mentioned before and presented in Ref. 11, the integrated, cryogenic HEMT readout not only allows one to distinguish dark counts from photon counts, but it should also allow one to achieve PNR in SSPD's. For large R_L's, the SSPD transient output pulse resulting from photodetection should be proportional in amplitude to the number of photons absorbed or, equivalently, the number of hotspots created in the SSPD. Unfortunately, it was shown by Ref. 18, in typical SSPD biased close to I_c, the R_{hs} can be as large as 5.5 kΩ, mainly due to Joule

heating. Even if it were possible to find a cryogenic amplifier with such large input R_L, the readout scheme would not work because the current would not be able to redistribute into the load fast enough before a runaway heating effect, and the device would simply latch.

Our devices, as mentioned before, have much lower than typical I_c's, although they still operate quite well. With our $I_{bias} \approx 5\ \mu$A, we estimate R_{hs} to be between 600 and 1000 Ω, so our selected $R_L = 500$ Ω is reasonable and should make it possible, in principle, to distinguish between the single- and multiphoton events.

Indeed, when the laser intensity and I_{bias} were increased so that the detector started to register nearly every incident light pulse, while the dark counts were still low, we observed that, in time-domain traces, some response pulses exhibited visibly higher amplitudes than the rest. Figure 115.52 shows an example of such a time trace, which is quite convincing, but, of course, it is impossible to conclude that these large pulses were indeed due to double-photon events, instead of, e.g., a single-photon event arriving close in time to a dark-count event, or even resulting from inhomogeneities of our meander stripe and resulting longer current redistribution time. It was therefore very useful to look at the statistics of the pulse-amplitude distributions once again. This time, most of our measurements were done by varying the intensity of our laser pulses (mode-locked and twice up-converted light to get $\lambda = 267$ nm) and I_{bias}, and collecting amplitudes of several thousand pulses at each value of the laser intensity and I_{bias}.

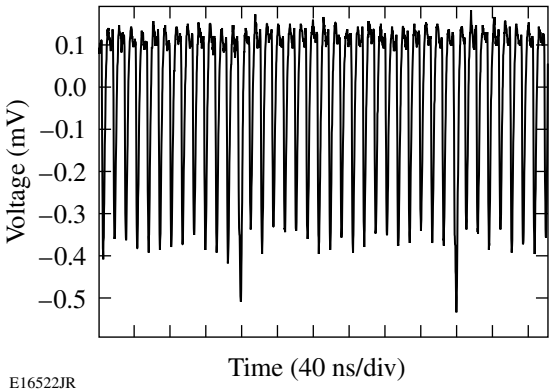

Figure 115.52
Real-time oscilloscope trace-domain trace, showing higher pulse amplitudes of some pulses.

The results are presented in Fig. 115.53. When $I_{bias} \approx 0.7\ I_c$, the amplitude distribution could be easily fit with a simple Gaussian function, as shown in Figs. 115.53(a) and 115.53(b). However, once I_{bias} reached $0.9\ I_c$, as shown in Figs. 115.53(c) and 115.53(d), we started to see a clear second peak at lower amplitudes, and the distribution now had to be fit with two Gaussians. The latter can be easily explained by the varying width (nonuniformity) of the NbN stripe: at higher I_{bias}, more (wider) sections of the SSPD meander were activated for photodetection, giving rise to the second Gaussian peak. This peak is expected to be centered at lower amplitudes, because Joule heating in the wider sections should give rise to lower R_{hs}, as in those sections we should expect a better heat dissipation into the substrate than that in the narrower sections.

When the data shown in Figs. 115.53(c) and 115.53(d) were plotted on a semi-log scale, as presented in Figs. 115.53(e) and 115.53(f), respectively, it became quite clear that in the $n \leq 1$ regime [Fig. 115.53(f)] there was, actually, a third small peak centered around 0.8 mV. This peak was completely absent in the $n \ll 1$ regime [Fig. 115.53(e)] and when I_{bias} was below $0.78\ I_c$. At present, we have no clear interpretation for the existence of this third peak. It cannot be related to the dark counts since they fall off exponentially with I_{bias} and are nearly zero below $0.85\ I_c$. Thus, the most-reasonable, tentative explanation is that it is indeed due to the SSPD detection of multiphoton events. Further analysis and calculations are needed to either support or disprove this conclusion.

Conclusion

We were able to resolve the difference between dark counts and photon counts in our NbN SSPD by utilizing an HEMT amplifier readout technique and examining pulse-amplitude distribution widths. The dark-count distribution width is very narrow for a given bias current, while that for photon counts is up to 2.5 times wider and is clearly related to the incident photon flux upon the SSPD (the average number of photons per pulse). The latter demonstrates that the HEMT readout is a promising approach in the future for PNR measurements.

ACKNOWLEDGMENT

This work was supported in part by the U.S. AFOSR grant FA9550-06-1-0348 and the NYSTAR grant to the University of Rochester CAT-EIS. We would also like to thank Prof. G. Gol'tsman and his group at the Moscow State Pedagogical University for their assistance in sample preparation and Prof. H. Mooij for very helpful discussions.

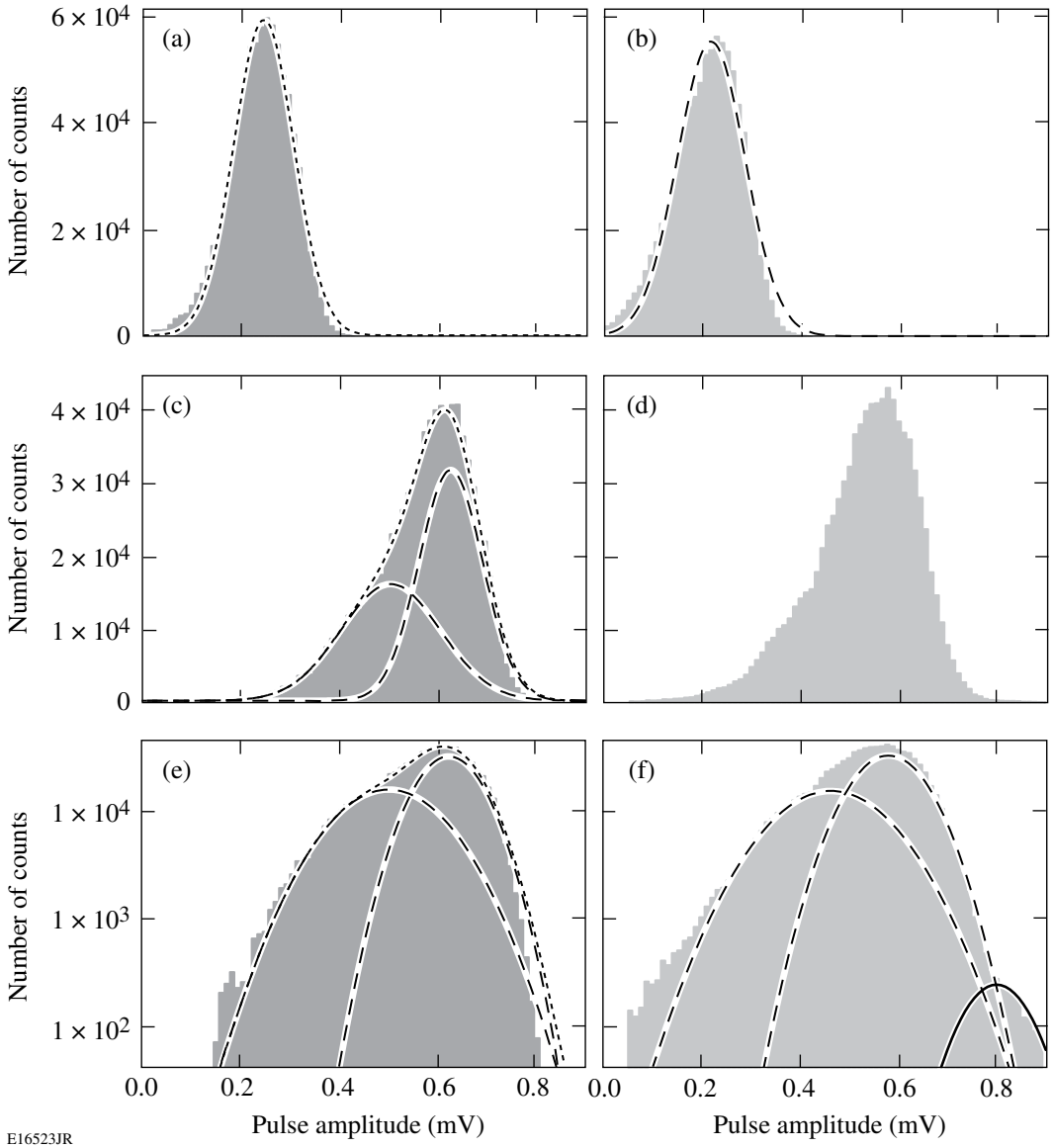

Figure 115.53
Pulse-amplitude histograms for (a) $n \ll 1$, $I_{bias} = 0.7\ I_c$, (b) $n \leq 1$, $I_{bias} = 0.7\ I_c$, (c) $n \ll 1$, $I_{bias} = 0.9\ I_c$, (d) $n \leq 1$, $I_{bias} = 0.9\ I_c$, (e) semi-log plot of (c), (f) semi-log plot of (d) (dark gray histograms indicate the same incident photon flux for the $n \ll 1$ regime; light gray histograms indicate the same incident photon flux for the $n \leq 1$ regime).

REFERENCES

1. W. Słysz, M. Węgrzecki, J. Bar, P. Grabiec, M. Górska, V. Zwiller, C. Latta, P. Böhi, A. J. Pearlman, A. S. Cross, D. Pan, J. Kitaygorsky, I. Komissarov, A. Verevkin, I. Milostnaya, A. Korneev, O. Minayeva, G. Chulkova, K. Smirnov, B. Voronov, G. N. Gol'tsman, and R. Sobolewski, J. Mod. Opt. **54**, 315 (2007).

2. C. Bennett and G. Brassard, in *International Conference on Computers, Systems, and Signal Processing* (IEEE Computer Society, IEEE Circuits and Systems Society, and Indian Institute of Science, Bangalore, India, 1984), pp. 175–179.

3. E. Waks, A. Zeevi, and Y. Yamamoto, Phys. Rev. A **65**, 052310 (2002); G. Brassard *et al.*, Phys. Rev. Lett. **85**, 1330 (2000).

4. E. Knill, R. Laflamme, and G. J. Milburn, Nature **409**, 46 (2001).

5. Y. Kang *et al.*, Appl. Phys. Lett. **85**, 1668 (2004).

6. G. Ribordy *et al.*, J. Mod. Opt. **51**, 1381 (2004).

7. K. M. Rosfjord *et al.*, Opt. Express **14**, 527 (2006).

8. J. Kitaygorsky, J. Zhang, A. Verevkin, A. Sergeev, A. Korneev, V. Matvienko, P. Kouminov, K. Smirnov, B. Voronov, G. Gol'tsman, and R. Sobolewski, IEEE Trans. Appl. Supercond. **15**, 545 (2005).

9. A. Engel *et al.*, Phys. Stat. Sol. C **2**, 1668 (2005).

10. J. Kitaygorsky, I. Komissarov, A. Jukna, D. Pan, O. Minaeva, N. Kaurova, A. Divochiy, A. Korneev, M. Tarkhov, B. Voronov, I. Milostnaya, G. Gol'tsman, and R. Sobolewski, IEEE Trans. Appl. Supercond. **17**, 275 (2007).

11. M. G. Bell *et al.*, IEEE Trans. Appl. Supercond. **17**, 289 (2007).

12. G. N. Gol'tsman, K. Smirnov, P. Kouminov, B. Voronov, N. Kaurova, V. Drakinsky, J. Zhang, A. Verevkin, and R. Sobolewski, IEEE Trans. Appl. Supercond. **13**, 192 (2003).

13. W. Słysz, M. Węgrzecki, J. Bar, P. Grabiec, M. Górska, V. Zwiller, C. Latta, P. Böhi, I. Milostnaya, O. Minaeva, A. Antipov, O. Okunev, A. Korneev, K. Smirnov, B. Voronov, N. Kaurova, G. Gol'tsman, A. Pearlman, A. Cross, I. Komissarov, A. Verevkin, and R. Sobolewski, Appl. Phys. Lett. **88**, 261113 (2006).

14. J. E. Mooij, in *Percolation, Localization, and Superconductivity*, edited by A. M. Goldman and S. A. Wolf, NATO ASI, Series B, Vol. 109 (Plenum Press, New York, 1984), pp. 325–370.

15. A. M. Kadin, J. Appl. Phys. **68**, 5741 (1990).

16. A. VI. Gurevich and R. G. Mints, Rev. Mod. Phys. **59**, 941 (1987).

17. A. J. Kerman *et al.*, Appl. Phys. Lett. **88**, 111116 (2006).

18. J. K. W. Yang IEEE Trans. Appl. Supercond. **17**, 581 (2007).

Publications and Conference Presentations

Publications

K. U. Akli, S. B. Hansen, A. J. Kemp, R. R. Freeman, F. N. Beg, D. C. Clark, S. D. Chen, D. Hey, S. P. Hatchett, K. Highbarger, E. Giraldez, J. S. Green, G. Gregori, K. L. Lancaster, T. Ma, A. J. MacKinnon, P. Norreys, N. Patel, J. Pasley, C. Shearer, R. B. Stephens, C. Stoeckl, M. Storm, W. Theobald, L. D. Van Woerkom, R. Weber, and M. H. Key, "Laser Heating of Solid Matter by Light-Pressure-Driven Shocks at Ultrarelativistic Intensities," Phys. Rev. Lett. **100**, 165002 (2008).

S.-W. Bahk, "Band-Limited Wavefront Reconstruction with Unity Frequency Response from Shack–Hartmann Slopes Measurements," Opt. Letters **33**, 1321 (2008).

R. Betti, W. Theobald, C. D. Zhou, K. S. Anderson, P. W. McKenty, S. Skupsky, D. Shvarts, V. N. Goncharov, J. A. Delettrez, P. B. Radha, T. C. Sangster, C. Stoeckl, and D. D. Meyerhofer, "Shock Ignition of Thermonuclear Fuel with High Areal Densities," J. Phys., Conf. Ser. **112**, 022024 (2008).

C. Dorrer, "Effect of Jitter on Linear Pulse-Characterization Techniques," Opt. Express **16**, 6567 (2008).

C. Dorrer and I. Kang, "Linear Self-Referencing Techniques for Short-Optical-Pulse Characterization," J. Opt. Soc. Am. B **25**, A1 (2008) (invited).

M. C. Ghilea, T. C. Sangster, D. D. Meyerhofer, R. A. Lerche, and L. Disdier, "Aperture Tolerances for Neutron-Imaging Systems in Inertial Confinement Fusion," Rev. Sci. Instrum. **79**, 023501 (2008).

V. N. Goncharov, T. C. Sangster, P. B. Radha, R. Betti, T. R. Boehly, T. J. B. Collins, R. S. Craxton, J. A. Delettrez, R. Epstein, V. Yu. Glebov, S. X. Hu, I. V. Igumenshchev, J. P. Knauer, S. J. Loucks, J. A. Marozas, F. J. Marshall, R. L. McCrory, P. W. McKenty, D. D. Meyerhofer, S. P. Regan, W. Seka, S. Skupsky, V. A. Smalyuk, J. M. Soures, C. Stoeckl, D. Shvarts, J. A. Frenje, R. D. Petrasso, C. K. Li, F. Séguin, W. Manheimer, and D. G. Colombant, "Performance of Direct-Drive Cryogenic Targets on OMEGA," Phys. Plasmas **15**, 056310 (2008) (invited).

V. N. Goncharov, T. C. Sangster, P. B. Radha, R. Betti, J. A. Delettrez, R. Epstein, D. R. Harding, S. X. Hu, I. V. Igumenshchev, F. J. Marshall, R. L. McCrory, P. W. McKenty, D. D. Meyerhofer, S. P. Regan, W. Seka, D. Shvarts, S. Skupsky, V. A. Smalyuk, C. Stoeckl, J. A. Frenje, C. K. Li, and R. D. Petrasso, "Modeling High-Compression, Direct-Drive, ICF Experiments," J. Phys., Conf. Ser. **112**, 022002 (2008).

O. V. Gotchev, P. Brijesh, P. M. Nilson, C. Stoeckl, and D. D. Meyerhofer, "A Compact, Multiangle Electron Spectrometer for Ultraintense Laser-Plasma Interaction Experiments," Rev. Sci. Instrum. **79**, 053505 (2008).

D. R. Harding, D. D. Meyerhofer, T. C. Sangster, S. J. Loucks, R. L. McCrory, R. Betti, J. A. Delettrez, D. H. Edgell, L. M. Elasky, R. Epstein, V. Yu. Glebov, V. N. Goncharov, S. X. Hu, I. V. Igumenshchev, D. Jacobs-Perkins, R. J. Janezic, J. P. Knauer, L. D. Lund, J. R. Marciante, F. J. Marshall, D. N. Maywar, P. W. McKenty, P. B. Radha, S. P. Regan, R. G. Roides, W. Seka, W. T. Shmayda, S. Skupsky, V. A. Smalyuk, C. Stoeckl, B. Yaakobi, J. D. Zuegel, D. Shvarts, J. A. Frenje, C. K. Li, R. D. Petrasso, and F. H. Séguin, "Cryogenic Target-Implosion Experiments on OMEGA," J. Phys., Conf. Ser. **112**, 022001 (2008).

S. X. Hu, "Heating of Frozen Rydberg Gases in a Strong Magnetic Field," J. Phys. B: At. Mol. Opt. Phys. **41**, 081009 (2008).

S. X. Hu, V. A. Smalyuk, V. N. Goncharov, J. P. Knauer, P. B. Radha, I. V. Igumenshchev, J. A. Marozas, C. Stoeckl, B. Yaakobi, D. Shvarts, T. C. Sangster, P. W. McKenty, D. D. Meyerhofer, S. Skupsky, and R. L. McCrory, "Studies of Plastic-Ablator Compressibility for Direct-Drive Inertial Confinement Fusion on OMEGA," Phys. Rev. Lett. **100**, 185003 (2008).

I. V. Igumenshchev, "Magnetically Arrested Disks and the Origin of Poynting Jets: A Numerical Study," Astrophys. J. **677**, 317 (2008).

I. Kang, S. Chandrasekhar, L. Buhl, P. G. Bernasconi, X. Liu, C. R. Giles, C. Kazmierski, N. Dupuis, J. Decobert, F. Alexandre, C. Jany, A. Garreau, J. Landreau, M. Rasras, M. Cappuzzo, L. T. Gomez, Y. F. Chen, M. P. Earnshaw, J. Lee, A. Leven, and C. Dorrer, "A Hybrid Electroabsorption Modulator Device for Generation of High Spectral-Efficiency Optical Modulation Formats," Opt. Express **16**, 8480 (2008).

I. Kang, C. Dorrer, L. Zhang, M. Dinu, M. Rasras, L. L. Buhl, S. Cabot, A. Bhardwaj, X. Liu, M. A. Cappuzzo, L. Gomez, A. Wong-Foy, Y. F. Chen, N. K. Dutta, S. S. Patel, D. T. Neilson, C. R. Giles, A. Piccirilli, and J. Jaques, "Characterization of the Dynamical Processes in All-Optical Signal Processing Using Semiconductor Optical Amplifiers," IEEE J. Sel. Top. Quantum Electron. **14**, 758 (2008) (invited).

C. Kim, J. U. Wallace, S. H. Chen, and P. B. Merkel, "Effects of Dilution, Polarization Ratio, and Energy Transfer on Photoalignment of Liquid Crystals Using Coumarin-Containing Polymer Films," Macromolecules **41**, 3075 (2008).

D. N. Maywar, J. H. Kelly, L. J. Waxer, S. F. B. Morse, I. A. Begishev, J. Bromage, C. Dorrer, J. L. Edwards, L. Folnsbee, M. J. Guardalben, S. D. Jacobs, R. Jungquist, T. J. Kessler, R. W. Kidder, B. E. Kruschwitz, S. J. Loucks, J. R. Marciante, R. L. McCrory, D. D. Meyerhofer, A. V. Okishev, J. B. Oliver, G. Pien, J. Qiao, J. Puth, A. L. Rigatti, A. W. Schmid, M. J. Shoup III, C. Stoeckl, K. A. Thorp, and J. D. Zuegel, "OMEGA EP High-Energy Petawatt Laser: Progress and Prospects," J. Phys., Conf. Ser. **112**, 032007 (2008).

R. L. McCrory, D. D. Meyerhofer, R. Betti, R. S. Craxton, J. A. Delettrez, D. H. Edgell, V. Yu. Glebov, V. N. Goncharov, D. R. Harding, D. W. Jacobs-Perkins, J. P. Knauer, F. J. Marshall, P. W. McKenty, P. B. Radha, S. P. Regan, T. C. Sangster, W. Seka, R. W. Short, S. Skupsky, V. A. Smalyuk, J. M. Soures, C. Stoeckl, B. Yaakobi, D. Shvarts, J. A. Frenje, C. K. Li, R. D. Petrasso, and F. H. Séguin, "Progress in Direct-Drive Inertial Confinement Fusion Research," Phys. Plasmas **15**, 055503 (2008) (invited).

M. Mikulics, M. Marso, S. Wu, A. Fox, M. Lepsa, D. Grützmacher, R. Sobolewski, and P. Kordoš, "Sensitivity Enhancement of Metal–Semiconductor–Metal Photodetectors on Low-Temperature-Grown GaAs Using Alloyed Contacts," IEEE Photon. Technol. Lett. **20**, 1054 (2008).

M. Nakatsutsumi, J. R. Davies, R. Kodama, J. S. Green, K. L. Lancaster, K. U. Akli, F. N. Beg, S. N. Chen, D. Clark, R. R. Freeman, C. D. Gregory, H. Habara, R. Heathcote, D. S. Hey, K. Highbarger, P. Jaanimagi, M. H. Key, K. Krushelnick, T. Ma, A. MacPhee, A. J. MacKinnon, H. Nakamura, R. B. Stephens, M. Storm, M. Tampo, W. Theobald, L. Van Woerkom, R. L. Weber, M. S. Wei, N. C. Woolsey, and P. A. Norreys, "Space and Time Resolved Measurements of the Heating of Solids to Ten Million Kelvin by a Petawatt Laser," New J. Phys. **10**, 043046 (2008).

P. Nilson, W. Theobald, J. Myatt, C. Stoeckl, M. Storm, O. V. Gotchev, J. D. Zuegel, R. Betti, D. D. Meyerhofer, and T. C. Sangster, "High-Intensity Laser-Plasma Interactions in the Refluxing Limit," Phys. Plasmas **15**, 056308 (2008) (invited).

S. P. Regan, T. C. Sangster, D. D. Meyerhofer, W. Seka, R. Epstein, S. J. Loucks, R. L. McCrory, C. Stoeckl, V. Yu. Glebov, O. S. Jones, D. Callahan, P. A. Amendt, N. B. Meezan, L. J. Suter, M. D. Rosen, O. L. Landen, E. L. DeWald, S. H. Glenzer, C. Sorce, S. Dixit, R. E. Turner, and B. MacGowan, "Hohlraum Energetics and Implosion Symmetry with Elliptical Phase Plates Using a Multi-Cone Beam Geometry on OMEGA," J. Phys., Conf. Ser. **112**, 022077 (2008).

T. C. Sangster, V. N. Goncharov, P. B. Radha, V. A. Smalyuk, R. Betti, R. S. Craxton, J. A. Delettrez, D. H. Edgell, V. Yu. Glebov, D. R. Harding, D. Jacobs-Perkins, J. P. Knauer, F. J. Marshall, R. L. McCrory, P. W. McKenty, D. D. Meyerhofer, S. P. Regan, W. Seka, R. W. Short, S. Skupsky, J. M. Soures, C. Stoeckl, B. Yaakobi, D. Shvarts, J. A. Frenje, C. K. Li, R. D. Petrasso, and F. H. Séguin, "High-Areal-Density Fuel Assembly in Direct-Drive Cryogenic Implosions," Phys. Rev. Lett. **100**, 185006 (2008).

W. Seka, D. H. Edgell, J. P. Knauer, J. F. Myatt, A. V. Maximov, R. W. Short, T. C. Sangster, C. Stoeckl, R. E. Bahr, R. S. Craxton, J. A. Delettrez, V. N. Goncharov, I. V. Igumenshchev, and D. Shvarts, "Time-Resolved Absorption in Cryogenic and Room-Temperature Direct-Drive Implosions," Phys. Plasmas **15**, 056312 (2008) (invited).

D. Shvarts, V. A. Smalyuk, R. Betti, J. A. Delettrez, D. H. Edgell, V. Yu. Glebov, V. N. Goncharov, R. L. McCrory, P. W. McKenty, D. D. Meyerhofer, F. J. Marshall, P. B. Radha, S. P. Regan, T. C. Sangster, W. Seka, S. Skupsky, C. Stoeckl, B. Yaakobi, J. A. Frenje, C. K. Li, R. D. Petrasso, and F. H. Séguin, "The Role of Fast-Electron Preheating in Low-Adiabat Cryogenic Implosions on OMEGA," J. Phys., Conf. Ser. **112**, 022005 (2008).

V. A. Smalyuk, D. Shvarts, R. Betti, J. A. Delettrez, D. H. Edgell, V. Yu. Glebov, V. N. Goncharov, R. L. McCrory, D. D. Meyerhofer, P. B. Radha, S. P. Regan, T. C. Sangster, W. Seka, S. Skupsky, C. Stoeckl, B. Yaakobi, J. A. Frenje, C. K. Li, R. D. Petrasso, and F. H. Séguin, "Role of Hot-Electron Preheating in the Compression of Direct-Drive Imploding Targets with Cryogenic D_2 Ablators," Phys. Rev. Lett. **100**, 185005 (2008).

A. A. Solodov and R. Betti, "Stopping Power and Range of Energetic Electrons in Dense Plasmas of Fast-Ignition Fusion Targets," Phys. Plasmas **15**, 042707 (2008).

W. Theobald, R. Betti, C. Stoeckl, K. S. Anderson, J. A. Delettrez, V. Yu. Glebov, V. N. Goncharov, F. J. Marshall, D. N. Maywar, R. L. McCrory, D. D. Meyerhofer, P. B. Radha, T. C. Sangster, W. Seka, D. Shvarts, V. A. Smalyuk, A. A. Solodov, B. Yaakobi, C. D. Zhou, J. A. Frenje, C. K. Li, F. H. Séguin, R. D. Petrasso, and L. J. Perkins, "Initial Experiments on the Shock-Ignition Inertial Confinement Fusion Concept," Phys. Plasmas **15**, 056306 (2008).

A. Trajkovska Petkoska, T. Z. Kosc, K. L. Marshall, K. Hasman, and S. D. Jacobs, "Motion of Doped-Polymer-Cholesteric Liquid Crystal Flakes in a Direct-Current Electric Field," J. Appl. Phys. **103**, 094907 (2008).

B. Yaakobi, T. R. Boehly, T. C. Sangster, D. D. Meyerhofer, B. A. Remington, P. G. Allen, S. M. Pollaine, H. E. Lorenzana, K. T. Lorenz, and J. A. Hawreliak, "Extended X-Ray Absorption Fine Structure Measurements of Quasi-Isentropically Compressed Vanadium Targets on the OMEGA Laser," Phys. Plasmas **15**, 062703 (2008).

Forthcoming Publications

S.-W. Bahk, J. Bromage, I. A. Begishev, C. Mileham, C. Stoeckl, M. Storm, and J. D. Zuegel, "On-Shot Focal-Spot Characterization Technique Using Phase Retrieval," to be published in Applied Optics.

A. M. Cok, R. S. Craxton, and P. W. McKenty, "Polar-Drive Designs for Optimizing Neutron Yields on the National Ignition Facility," to be published in Physics of Plasmas.

C. Dorrer, J. Bromage, and J. D. Zuegel, "High-Dynamic-Range, Single-Shot Cross-Correlator Based on an Optical Pulse Replicator," to be published in Optics Express.

T. Duffy, W. T. Shmayda, R. Janezic, S. J. Loucks, and J. Reid, "LLE's High-Pressure DT-Fill-Process Control System," to be published in Fusion Science and Technology.

M. J. Guardalben, "Littrow Angle Method to Remove Alignment Errors in Grating Pulse Compressors," to be published in Applied Optics.

S. X. Hu, V. A. Smalyuk, V. N. Goncharov, S. Skupsky, T. C. Sangster, D. D. Meyerhofer, and D. Shvarts, "Validating Thermal Transport Modeling with Planar-Foil Experiments on OMEGA," to be published in Physical Review Letters.

H. Irie, Q. Diduck, M. Margala, R. Sobolewski, and M. J. Feldman, "Nonlinear Characteristics of T-Branch Junctions—Transition from Ballistic to Diffusive Regime," to be published in Applied Physics Letters.

Z. Jiang and J. R. Marciante, "Comments on 'Beam Quality Factor of Higher Order Modes in a Step-Index Fiber,' " to be published in the Journal of Lightwave Technology.

W. Manheimer, D. Colombant, and V. Goncharov, "The Developement of a Krook Model for Nonlocal Transport in Laser Produced Plasmas. I. Basic Theory," to be published in Physics of Plasmas.

P. M. Nilson, L. Willingale, M. C. Kaluza, C. Kamperidis, S. Minardi, M. S. Wei, P. Fernandes, M. Notley, S. Bandyopadhyay, M. Sherlock, R. J. Kingham, M. Tatarakis, Z. Najmudin, W. Rozmus, R. G. Evans, M. G. Haines, A. E. Dangor, and K. Krushelnick, "Bi-Directional Jet Formation During Driven Magnetic Reconnection in Two-Beam Laser–Plasma Interaction," to be published in Physics of Plasmas.

J. Qiao, A. Kalb, T. Nguyen, J. Bunkenburg, D. Canning, and J. H. Kelly, "Demonstration of Large-Aperture, Tiled-Grating Compressors for High-Energy Petawatt-Class Chirped-Pulse–Amplification Systems," to be published in Optics Letters.

M. J. Quinlan, W. T. Shmayda, S. Lim, S. Salnikov, Z. Chambers, E. Pollock, and W. U. Schröder, "Effects of H_2O and H_2O_2 on Thermal Desorption of Tritium from Stainless Steel," to be published in Fusion Science and Technology.

S. N. Shafrir, S. D. Jacobs, S. Adar, C. Miao, H. Romanofsky, and J. C. Lambropoulos, "Drag Force and Surface Texture in Material Removal with MRF on Optical Glass and Hard

Ceramics," to be published in the Proceedings of the 12th Electromagnetic Symposium.

A. Simon, "Response to 'Comment on "An Alternative Analysis of Some Recent Diffusion Experiments on the LAPD Device" ' [Phys. Plasmas **15**, 022507 (2008)]," to be published in Physics of Plasmas.

V. A. Smalyuk, S. X. Hu, V. N. Goncharov, D. D. Meyerhofer, T. C. Sangster, D. Shvarts, C. Stoeckl, B. Yaakobi, J. A. Frenje, and R. D. Petrasso, "Rayleigh–Taylor Growth Stabilization in Direct-Drive Plastic Targets at Laser Intensities of $\sim 1 \times 10^{15}$ W/cm^2," to be published in Physical Review Letters.

V. A. Smalyuk, S. X. Hu, V. N. Goncharov, D. D. Meyerhofer, T. C. Sangster, C. Stoeckl, and B. Yaakobi, "Systematic Study of Rayleigh–Taylor Growth in Direct-Drive Plastic Targets in a Laser-Intensity Range of $\sim 2 \times 10^{14}$ W/cm^2 to $\sim 1.5 \times 10^{15}$ W/cm^2," to be published in Physics of Plasmas.

M. Storm, I. A. Begishev, R. J. Brown, C. Guo, D. D. Meyerhofer, C. Mileham, J. F. Myatt, P. M. Nilson, T. C. Sangster, C. Stoeckl, W. Theobald, and J. D. Zuegel, "A High-Resolution Coherent Transition-Radiation Diagnostic for Laser-Produced Electron Transport Studies," to be published in Review of Scientific Instruments.

A. Trajkovska-Petkoska and S. D. Jacobs, "Effect of Different Dopants on Polymer Cholesteric Liquid Crystals," to be published in Molecular Crystals and Liquid Crystals.

M. S. Wei, A. A. Solodov, J. Pasley, R. B. Stephens, D. R. Welch, and F. N. Beg, "Study of Relativistic Electron Beam Production and Transport in High-Intensity Laser Interaction with a Wire Target by Integrated LSP Modeling," to be published in Physics of Plasmas.

Y. Zhu, J. D. Zuegel, J. R. Marciante, and H. Wu, "Distributed Waveform Generator: A New Circuit Technique for Ultra-Wideband Pulse Generation, Shaping, and Modulation," to be published in IEEE Journal of Solid-State Circuits.

Conference Presentations

The following presentations were made at HEDP/HEDLA–08, St. Louis, MO, 11–15 April 2008:

D. D. Meyerhofer, "HED Physics Opportunities on OMEGA/OMEGA EP."

S. P. Regan, H. Sawada, D. D. Meyerhofer, P. B. Radha, J. A. Delettrez, R. Epstein, V. N. Goncharov, D. Li, V. A. Smalyuk, T. C. Sangster, B. Yaakobi, and R. C. Mancini, "Creating and Probing Matter Compressed and Heated by Shock Waves on OMEGA."

J. P. Knauer, S. Sublett, R. S. Craxton, T. J. B. Collins, I. V. Igumenshchev, D. D. Meyerhofer, A. Frank, and R. P. Drake, "Hydrodynamic Jet Experiments at LLE," APS April Meeting 2008, St. Louis, MO, 12–15 April 2008.

C. Miao, S. N. Shafrir, S. Adar, H. Romanofsky, and S. D. Jacobs, "*In-Situ* Drag Force and Normal Force Measurement for Magnetorheological Finishing (MRF) of Hard Ceramics," 16th Symposium on Materials Research, Rochester, NY, 22 April 2008.

S. N. Shafrir, S. D. Jacobs, S. Adar, C. Miao, H. Romanofsky, and J. C. Lambropoulos, "Drag Force and Surface Texture in Material Removal with MRF on Optical Glass and Hard Ceramics," 12th Department of Defense Electromagnetic Windows Symposium, Redstone Arsenal, AL, 28 April–1 May 2008.

The following presentations were made at CLEO 2008, San Jose, CA, 6–8 May 2008:

S.-W. Bahk, J. Bromage, J. D. Zuegel, and J. R. Fienup, "Application of Phase Retrieval for Predicting a High-Intensity-Focused Laser Field."

C. Dorrer, "Effect of Jitter on Linear Self-Referencing Pulse-Characterization Techniques."

C. Dorrer, I. A. Begishev, A. V. Okishev, and J. D. Zuegel, "Extreme-Contrast Front End for High-Power Laser Systems."

C. Dorrer, J. Bromage, and J. D. Zuegel, "High-Dynamic-Range, Single-Shot Cross-Correlator Using a Pulse Replicator."

C. Dorrer, A. V. Okishev, I. A. Begishev, J. D. Zuegel, V. I. Smirnov, and L. B. Glebov, "Optical Parametric Chirped-Pulse–Amplification Contrast Enhancement by Regenerative Pump Spectral Filtering."

W. Guan and J. R. Marciante, "Suppression of Self-Pulsations in Dual-Clad Ytterbium-Doped Fiber Lasers."

A. V. Okishev, "Multimillijoule Picosecond Regenerative Differentiator-Amplifier."

J. Qiao, A. Kalb, J. H. Kelly, D. Canning, T. Nguyen, and J. Bunkenburg, "Realization of Tiled-Grating Compressors for the OMEGA EP Petawatt Laser System."

L. J. Waxer, M. J. Guardalben, J. H. Kelly, B. E. Kruschwitz, J. Qiao, I. A. Begishev, J. Bromage, C. Dorrer, J. L. Edwards, L. Folnsbee, S. D. Jacobs, R. Jungquist, T. J. Kessler, R. W. Kidder, S. J. Loucks, J. R. Marciante, D. N. Maywar, R. L. McCrory, D. D. Meyerhofer, S. F. B. Morse, A. V. Okishev, J. B. Oliver, G. Pien, J. Puth, and A. L. Rigatti, "The OMEGA EP High-Energy, Short-Pulse Laser System" (invited).

The following presentations were made at the 17th Topical Conference on High-Temperature Plasma Diagnostics, Albuquerque, NM, 11–15 May 2008:

Z. A. Ali, V. Yu. Glebov, M. Cruz, T. Duffy, C. Stoeckl, S. Roberts, T. C. Sangster, R. Tommasini, and S. Throop, "Tests and Calibration of the NIF Neutron Time-of-Flight Diagnostic."

C. G. Freeman, C. Stoeckl, T. C. Sangster, T. Duffy, and C. Mileham, "A Thomson Parabola for the Multiterawatt Laser Facility."

V. Yu. Glebov, M. Moran, C. Stoeckl, T. C. Sangster, and M. Cruz, "Neutron Bang Time Detector Based on a Light Pipe."

M. Storm, C. Guo, D. D. Meyerhofer, J. Myatt, T. C. Sangster, and C. Stoeckl, "Relativistic Electron-Beam Transport Measurements" (invited).

The following presentations were made at the 18th Target Fabrication Meeting, Lake Tahoe, CA, 11–15 May 2008:

M. J. Bonino, D. R. Harding, and L. M. Elasky, "Effects of Target Assembly on the Quality of Cryogenic Ice Layers."

D. H. Edgell, M. D. Wittman, R. S. Craxton, L. M. Elasky, D. R. Harding, and W. Seka, "Three-Dimensional Characterization of Cryogenic Targets Using X-Ray Phase-Contrast Imaging and Shadowgraphy."

L. M. Elasky, S. J. Verbridge, A. J. Weaver, and D. R. Harding, "Success of Layering with DT and Developments with D_2 in OMEGA Cryogenic Targets."

D. R. Harding, T. B. Jones, Z. Bei, D. H. Edgell, and S. H. Chen, "Cryogenic-DT-Foam Targets: The New Frontier."

T. B. Jones, Z. Bei, and D. R. Harding, "Electric-Field-Assisted Target Fabrication."

S. J. Verbridge, A. J. Weaver, D. R. Harding, and L. M. Elasky, "Effects of Process Limitations and Shell Composition on Cryogenic Target Layers."

G. P. Wainwright and W. T. Shmayda, "Tritium Management on OMEGA at the Laboratory for Laser Energetics."

M. D. Wittman and D. R. Harding, "Performance and Capabilities of the Cryogenic Fill-Tube Target Test Facility at LLE."

The following presentations were made at the 38th Annual Anomalous Absorption Conference, Williamsburg, VA, 1–6 June 2008:

R. S. Craxton, P. W. McKenty, J. A. Marozas, and A. M. Cok, "Optimization of Neutron Yields on the NIF from Room-Temperature DT Targets."

J. A. Delettrez, V. N. Goncharov, P. B. Radha, D. Shvarts, C. Stoeckl, B. Yaakobi, A. V. Maximov, W. Seka, J. A. Frenje, J. F. Myatt, T. C. Sangster, and V. A. Smalyuk, "Simulations of the Effect of Energetic Electrons Produced from Two-Plasmon Decay in the 1-D Hydrodynamic Code *LILAC*."

D. H. Edgell, W. Seka, J. A. Delettrez, R. S. Craxton, V. N. Goncharov, I. V. Igumenshchev, J. F. Myatt, A. V. Maximov, R. W. Short, T. C. Sangster, and R. E. Bahr, "Time-Dependent Scattered-Laser-Light Spectroscopy in Direct-Drive Inertial Confinement Fusion Experiments."

R. Epstein, J. A. Delettrez, V. N. Goncharov, P. W. McKenty, F. J. Marshall, P. B. Radha, H. Sawada, and B. Yaakobi, "Radiative-Transport Modeling Relevant to Cryogenic Implosion Simulation and Diagnosis."

A. V. Maximov, J. F. Myatt, R. W. Short, W. Seka, C. Stoeckl, and J. A. Delettrez, "Modeling of Two-Plasmon-Decay Instability Driven by Crossing Laser Beams."

J. Myatt, D. H. Edgell, W. Seka, A. V. Maximov, and R. W. Short, "Two-Plasmon-Decay Hot-Electron Distribution from Anistropic Thick-Target Bremsstrahlung Measurements."

T. C. Sangster, J. H. Kelly, S. J. Loucks, D. D. Meyerhofer, S. F. B. Morse, R. L. McCrory, and C. Stoeckl, "Status of the OMEGA EP Laser System."

W. Seka, D. H. Edgell, J. F. Myatt, A. V. Maximov, R. W. Short, C. Stoeckl, R. E. Bahr, R. S. Craxton, J. A. Delettrez, and V. N. Goncharov, "Two-Plasmon-Decay Instability in Direct-Drive Implosion Experiments."

R. W. Short, "Two-Plasmon Decay of Multiple Obliquely Incident Laser Beams in Direct-Drive Geometry."

A. A. Solodov, K. S. Anderson, R. Betti, V. Gotcheva, J. F. Myatt, J. A. Delettrez, and S. Skupsky, "Integrated Simulations of Hot-Electron Transport and Ignition for Direct-Drive, Fast-Ignition Fusion Targets."

C. Stoeckl, K. S. Anderson, R. Betti, T. R. Boehly, J. A. Delettrez, J. A. Frenje, V. N. Goncharov, V. Yu. Glebov, J. H. Kelly, A. J. Mackinnon, R. L. McCrory, D. D. Meyerhofer, S. F. B. Morse, J. F. Myatt, P. A. Norreys, P. M. Nilson, R. D. Petrasso, T. C. Sangster, A. A. Solodov, R. B. Stephens, M. Storm, W. Theobald, L. J. Waxer, B. Yaakobi, and C. D. Zhou, "Fast-Ignition Target Design and Experimental-Concept Validation on OMEGA," 10th International Workshop on Fast Ignition of Fusion Targets, Crete, Greece, 12–18 June 2008 (invited).

O. V. Gotchev, P. Chang, J. P. Knauer, D. D. Meyerhofer, R. Betti, F. H. Séguin, C. K. Li, J. A. Frenje, and R. D. Petrasso, "Magnetized Hot-Spot Implosions on OMEGA," ICC 2008 Workshop, Reno, NV, 24–27 June 2008.


1850
MELIORA
UNIVERSITY of
ROCHESTER